SAND2017-1652

SANDIA REPORT

00000000
Unlimited Release
Printed 2/2017

Imaging Fracture Networks Using Joint Seismic and Electrical Change Detection Techniques

Hunter Knox (SNL), Jonathan Ajo-Franklin (LBNL), Timothy Johnson (PNNL), Joseph Morris (LLNL), Mark Grubelich (SNL), Stephanie James (SNL), Alex Rinehart (NMBG), Leiph Preston (SNL), Vince Vermeul (PNNL), Chris Strickland (PNNL), James Knox (SNL), Dennis King (SNL), Craig Ulrich (LBNL)

Prepared by
Sandia National Laboratories
Albuquerque, New Mexico 87185 and Livermore, California 94550

Sandia National Laboratories is a multi-mission laboratory managed and operated by Sandia Corporation, a wholly owned subsidiary of Lockheed Martin Corporation, for the U.S. Department of Energy's National Nuclear Security Administration under contract DE-AC04-94AL85000.

Issued by Sandia National Laboratories, operated for the United States Department of Energy by Sandia Corporation.

Available to DOE and DOE contractors from
U.S. Department of Energy
Office of Scientific and Technical Information
P.O. Box 62
Oak Ridge, TN 37831

Telephone: (865) 576-8401
Facsimile: (865) 576-5728
E-Mail: reports@adonis.osti.gov
Online ordering: http://www.osti.gov/bridge

Available to the public from
U.S. Department of Commerce
National Technical Information Service
5285 Port Royal Rd
Springfield, VA 22161

Telephone: (800) 553-6847
Facsimile: (703) 605-6900
E-Mail: orders@ntis.fedworld.gov
Online ordering: http://www.ntis.gov/help/ordermethods.asp?loc=7-4-0#online

00000000
Unlimited Release
Printed 2/2017

Imaging Fracture Networks Using Joint Seismic and Electrical Change Detection Techniques

Blue Canyon Dome SubTER Team

Abstract

During the initial phase of this SubTER project, we conducted a series of high resolution seismic imaging campaigns designed to characterize induced fractures. Fractures were emplaced using a novel explosive source, designed at Sandia National Laboratories, that limits damage to the borehole. This work provided evidence that fracture locations could be imaged at inch scales using high-frequency seismic tomography but left many fracture properties (i.e. permeability) unresolved. We present here the results of the second phase of the project, where we developed and demonstrated emerging seismic and electrical geophysical imaging technologies that characterize 1) the 3D extent and distribution of fractures stimulated from the explosive source, 2) 3D fluid transport within the stimulated fracture network through use of a contrasting tracer, and 3) fracture attributes through advanced data analysis. Focus was placed upon advancing these technologies toward near real-time acquisition and processing in order to help provide the feedback mechanism necessary to understand and control fracture stimulation and fluid flow. Results from this study include a comprehensive set of 4D crosshole seismic and electrical data that take advantage of change detection methodologies allowing for perturbations associated with the fracture emplacement and particulate tracer to be isolated. During the testing the team also demonstrated near real-time 4D electrical resistivity tomography imaging and 4D seismic tomography using the CASSM approach with a temporal resolution approaching 1 minute. All of the data collected were used to develop methods of estimating fracture attributes from seismic data, develop methods of assimilating disparate and transient data sets to improve fracture network imaging resolution, and advance capabilities for near real-time inversion of cross-hole tomographic data. These results are illustrated here. Advancements in these areas are relevant to all situations where fracture emplacement is used for reservoir stimulation (e.g. Enhanced Geothermal Systems (EGS) and tight shale gases).

Acknowledgment

We would like to take this opportunity to thank the all of the people responsible for standing up this important cross cutting initiative and those that have worked tirelessly to form the framework under which this research was executed. This project, along with its seedling project, was funded under the Subsurface Technology and Engineering Research (SubTER) program. The SubTER initiative is championed at the U.S. Department of Energy (DOE), by Julio Friedman, Doug Hollett, Susan Hamm, Eric Hass, Margaret Coleman, and Kevin McCarthy. Furthermore we would like to thank the SubTER Leads and Deputies at the National Laboratories including Susan Hubbard, Jens Birkholzer, Curtis Oldenburg, Marianne Walck, Erik Webb, and Susan Altman. Most of the work described herein was conducted under the *Permeability Manipulation and Fluid Control* and the *New Subsurface Signals* pillars, which was lead by Rajesh Pawar, Earl mattson, Alain Bonneville, and Rob Mellors.

This particular SubTER sapling project would not have been possible without tremendous support from the Geothermal Technology Office (GTO) and specifically Alex Prisjatschew, Eric Hass, Michael Weathers. It was also managed by Traci Rodosta, Andrea Dunn, Erik Albenze, and Kanwal Mahajan at NETL. This combined GTO-NETL team provided a great deal of guidance and oversight through out the one year project.

Finally, we would like to take this opportunity to recognize the large number of the people who contributed technically to this project. Those not included on the author list are as follows: Kirsten Chojnicki, Avery "Zack" Cashion, Greg Cieslewski, David Chavira, Adam Foris, Doug Blankenship, Pierpaolo Marchesini, Yuxin Wu, Tom Daley, and Paul Cook. All of their valuable input led to the successful completion of this project.

Contents

Appendix

List of Figures

List of Tables

Nomenclature

SNL Sandia National Laboratories

LBNL Lawrence Berkley National Laboratory

PNNL Pacific Northwest National Laboratory

LLNL Lawrence Livermore National Laboratory

NMBG New Mexico Bureau of Geology

DOE Department of Energy

SubTER Subsurface Technology and Engineering Research

GTO Geothermal Technologies Office

MEQ Microseismic Earthquakes or Microseismic Events

EMRTC Energetic Materials Research and Testing Center

NMT New Mexico Institute of Mining and Technology

DAS Distributed Acoustic Sensing

DTS Distributed Temperature Sensing

nZVI nano-Zero Valent Iron

CRT Complex Resistivity Tomography

SIP Spectral Induced Polarization

TOC Top of Casing

ML-CASSM Multi-level Continuous Active Source Seismic Monitoring

CSL Crosshole Sonic Logging

CT Crosshole Tomography

Chapter 1

Background

A primary goal of the SubTER initiative is to develop methods of controlling flow within deep subsurface fractured rock systems in order to optimize energy recovery, storage capacity, and environmental protection. Adequate feedback mechanisms are central to this goal. Namely, methods are needed that can characterize fracture networks and monitor fracture flow, and can do so at time scales small enough to provide actionable feedback information during stimulation and/or other injection/extraction operations. Seismic and electrical geophysical imaging techniques are able to estimate complimentary fractured rock properties (and changes therein) in regions between deep boreholes, and are a natural candidate for remotely characterizing and monitoring fractured rock systems. However, current technologies are limited in terms of providing the feedback loop necessary to control fracture stimulation and fluid flow. In particular, 1) data may be insensitive to small-scale fractures that are important to system function, 2) data collection and processing times limit temporal and spatial imaging resolution, 3) important fracture attributes (e.g. permeability) are not routinely estimated.

At the present time, minimal spatial information on the geometry of induced fracture networks is available during or after reservoir stimulation in a reservoir context, beyond the zone of initiation and production data. The one source of spatial and temporal constraints on the fracture network is analysis of microseismic events (MEQs) associated with stimulation; unfortunately the hypocenter data from such analysis is highly limited in spatial accuracy due to velocity model uncertainty and typically provides only diffuse clouds of activity. Likewise, MEQs provide no information on fracture aperture and may not be observable in some cases of mode 1 opening or aseismic slip. Primarily, evidence for the efficacy of permeability modification provided by fracturing comes from production and injection data rather than spatial imaging of fractures or geophysical inference of fracture properties. Adaptive control of fracturing fundamentally requires an alternative source of data to dynamically understand fracture distribution, connectivity, aperture, and impact on flow. This is particularly true in the case of novel stimulation methods involving energetic sources where only limited prior data exists on induced fracture geometry.

Recent research has proposed a path forward to provide this information through use of high-temporal resolution active geophysical measurements, mainly continuous borehole seismic measurements and behind-casing electrical resistance tomography (ERT). While the geophysical detectability of fractures has been known for decades (e.g. Aki et al. (1982)

and Majer et al. (1997)), only recently have continuous downhole acquisition systems been capable of acquiring quasi real-time tomographic data sufficient for direct time-lapse imaging (Ajo-Franklin et al., 2011; Daley et al., 2007) of subtle changes in seismic velocity and attenuation.

Likewise, autonomous ERT hardware and software have developed to the point where high temporal resolution measurements, and in some case real-time inversions (e.g. Johnson and Wellman (2015)), should allow for investigation of fracture extent and transport processes (e.g. Robinson et al. (2015)) dynamically, particularly when fracture properties are enhanced with a geophysical tracer. Beyond mapping the geometry of fractures using active geophysical imaging, the change in measured elastic and/or electrical properties may provide semi- quantitative information on fracture aperture and permeability. Sayers and den Boer (2012) and Morris et al. (2013, 2015) have demonstrated models that provide stress-dependent estimates of fracture hydraulic conductivity derived from seismic/acoustic attributes. The combination of jointly acquired geophysical datasets with high temporal resolution and quantitative models to infer fracture properties suggests that real-time dynamic imaging of induced fracture networks is within reach.

Chapter 2

Introduction

Efficient reservoir enhancement, whether it is applied to tight shale gases or geothermal reservoirs, requires both effective stimulation and real-time feedback. It is easy to imagine a system where an initial stimulation would occur and real-time feedback could drive all subsequent stimulations. This would enable a well to be stimulated safely until no further economic benefit could be realized. In the case of geothermal reservoirs, we propose that coupling novel energetic stimulations with multi-disciplinary geophysical change detection techniques provides an avenue under which this system is realized.

The first part of the aforementioned system, formation stimulations using energetic materials (i.e. explosives), has been widely applied for enhanced recovery of fluids in the oil and gas industry. Many of these energetic methods, however, have notable limitations including possible well bore and/or formation damage (e.g. Schmidt et al. (1980)). It has long been known that in an ideal case, the energetic materials (aka the stimulation system) would produce multiple fractures and eliminate well bore damage. These objectives would likely be achieved by generating both a controlled pressure rise rate and an acceptable final pressure. With conventional high explosives, the pressure rise rate is non-optimal and the near field pressures are too high. In general, the use of high explosives produces numerous short fractures effectively shattering the well bore in the near field. Conversely, quasi static, low pressure rise rate systems such as hydraulic or slow burning propellant based fracturing methods cannot easily produce multiple fractures or induce shear destabilization (i.e self-propping). The energetic materials research described herein, aims to develop a stimulation system that falls between the high explosive and quasi-static low-pressure regimes, thereby providing both a controlled pressure rise rate and an acceptable final pressure. Furthermore, this form of stimulation removes the limitations and complications of conventional hydraulic fracturing techniques and also eliminates the wastewater produced with conventional hydraulic fracturing.

Furthermore, the second piece of an efficient fracturing system, imaging fractures with geophysical techniques, has remained a central focus for reservoir development, especially in tight shale gas formations and Enhanced Geothermal Systems (EGS), and for material storage applications such as CO2 sequestration and deep nuclear repositories. An outstanding problem, however, is that imaging fractures and their evolution during production and/or storage is inherently complex, regardless of logistical and/or economic monitoring constraints. This difficulty arises primarily from two characteristics: 1) the tortuous and

multi-scaled geometries of fracture networks (e.g. extrinsic anisotropy), which at the smallest levels is unresolvable with far-field geophysical observations, and 2) the intrinsic anisotropy of the natural rock systems where targets are typically located (e.g. volcanics, tight shales). It has been shown, however, that imaging resolution can be improved by increasing two geophysical survey design parameters: 1) azimuthal and offset coverage (i.e. surrounding the target at closer offsets) and 2) independent data measurements (i.e. multi-physics large N approaches) (e.g. Neal et al. (2012) and Bergmann et al. (2013)).

Herein we will show promising results from a SubTER Sapling study and outline in detail a multi-disciplinary experiment that was conducted in April of 2016. The meso-scale multi-physics experiment was designed to image fractures generated by the aforementioned novel controlled rapid pressurization technique. This imaging includes real time electrical resistance (ERT) and seismic tomography, campaign style high resolution seismic tomography, the use of a contrasting agent, continuous recording on a fiber optic cable (i.e. Digital Acoustic Sensing and Digital Temperature Sensing) array, traditional pressure decay tests, and traditional borehole logging techniques for imaging fractures. Analysis of this data set includes implementation of joint inversions, passive seismic interferometry, and change detection techniques. These geophysical parameters and their associated changes are then evaluated for quantifiable changes in stress or mechanical and hydraulic properties. All of the fracture characterization and monitoring data generated under this experiment will be made available to wider research community after a brief sequestration period to allow analysis by the original research team. This work is affiliated with The Subsurface Technology and Engineering Research, Development, and Demonstration (SubTER) Crosscut, which encompasses DOE offices involved in subsurface activities that are aligned with energy production/extraction, subsurface storage of energy and CO2, and subsurface waste disposal and environmental remediation.

Chapter 3

Field Site

The work described here has been conducted at the Blue Canyon Dome in Socorro, NM. Socorro is located approximately 80 miles south of Albuquerque, New Mexico (see Figure 3.1. The field site, which is comprised of a series of shallow boreholes, is situated on a ridge on Socorro Peak approximately four miles west of the town. The ridge itself is unbounded on three sides (making it approximately stress free) and for our purposes consists of a two-layer geologic system. The uppermost layer ($\sim$ top 30 feet) is comprised of weathered (i.e. highly fractured) rhyolite. The second layer is un-weathered rhyolite with sparse near vertical natural fractures that have been mineralized. The un-weathered rhyolite has a compressive strength of approximately 38k psi (262 MPa). Details about emplacement, geologic context, etc are not discussed here, but can be found in extensive publications (e.g.(Chamberlin et al., 2004). The site is managed by the Energetic Materials Research and Testing Center (EMRTC), which is affiliated with New Mexico Institute of Mining and Technology (NMT).

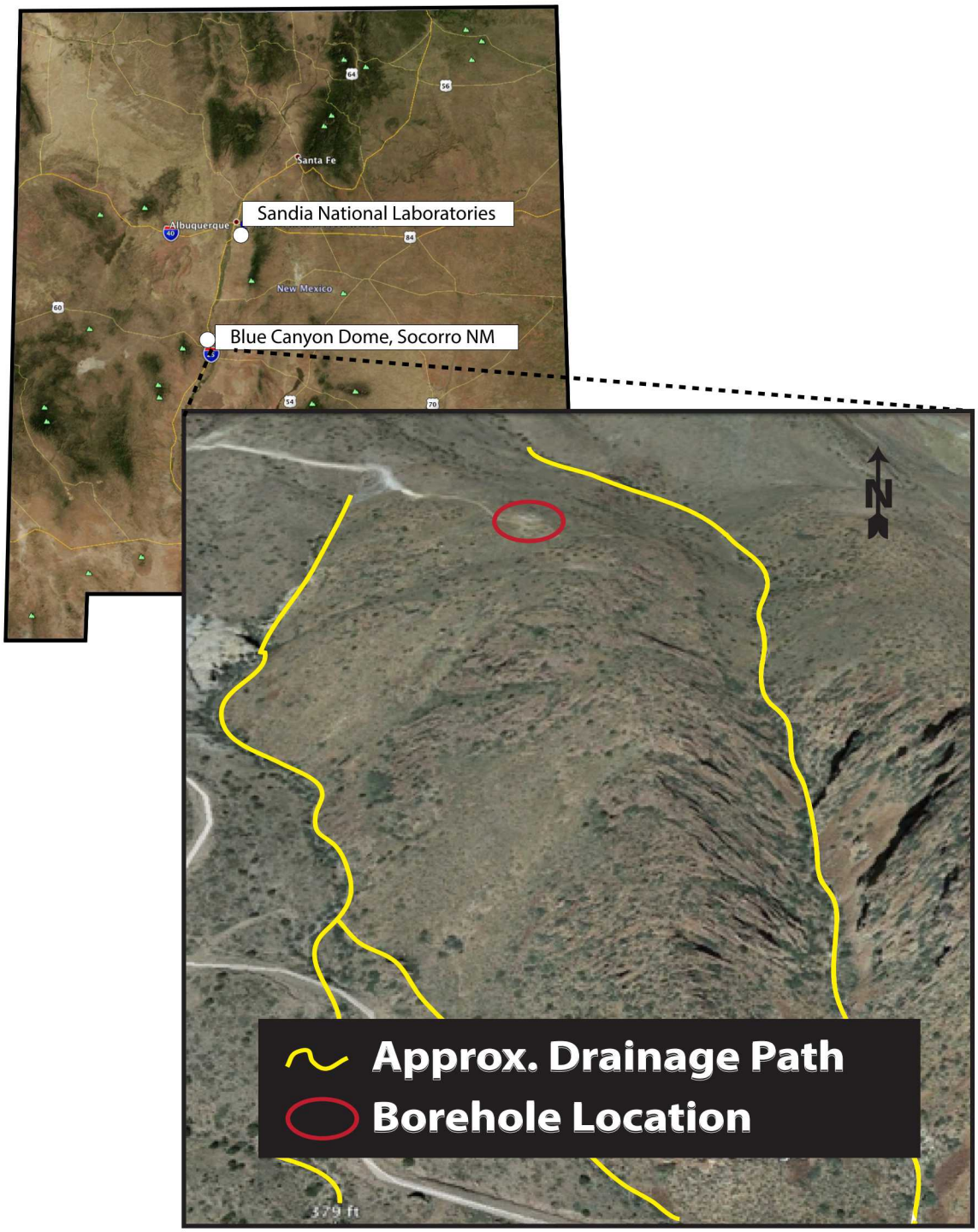

Figure 3.1. Location of Blue Canyon Dome in Socorro, NM, relative to Sandia National Laboratories, which is located in Albuquerque, NM. The drainage paths give the reader a sense that the field site is situated on a ridge.

Chapter 4

Instrumentation Installation

During the week of September 28th, 2015, the SubTER team undertook the task of installing the geophysical hardware in each of the four monitoring boreholes (see Figure 4.1). These monitoring boreholes were completed using hammer drilling techniques during the week of September 21st, 2015. During the drilling operations, the stimulation borehole was also extended from it original depth (∼65 ft) to 75 feet and core was extracted. Examination of this core indicated that there were no obvious fractures and that the rock had similar textural, color, and strength properties (i.e. the core had to be broken with a sledge hammer so that it would fit in the core box).

The multi-phenomenology field campaign required careful consideration to ensure that multiply systems could occupy the same monitoring boreholes without interfering with each other or degrading data quality. Figure 4.3 depicts the conceptual model for instrumentation installation where campaign style (temporally sparse, except for ML-CASSM) measurements are conducted inside the water-tight casing and the continuous ERT and DAS measurements systems occupy the annulus in each borehole. The execution of this design is shown in Figures 4.4, 4.5, 4.6. Close examination of the aforementioned figures shows that both the ERT electrodes and the fiber optic cable were both installed on the exterior of the casing. The fiber was looped at the bottom of each of the casing strings to avoid unnecessary splices and secured to the casing using duct tape and zip-ties (see Figures 4.4 and 4.6). The ERT electrodes were secured using band clamps and the cables were secured using zip-ties, this process is further described in a later section (see Figure 4.5).

For reference, we include here some of the finer details of the casing installation. First, each section of casing was "roughed up" using a belt sander. This task was undertaken to help mitigate any potential debonding between the casing and the grout. Furthermore, the tremie pipe was only partially secured to the end of the casing string. This contact was broken after a sufficient amount of grout was pumped downhole and the team could ensure that the grout level was above the tremie pipe. The team then gradually raised the tremie pipe maintaining its position below the grout level. This helped ensure continuous grout coverage. Finally, we include here two last points: 1) the grout was custom designed for the ERT survey and 2) the boreholes were filled with water while the grout was curing in the annulus. The latter consideration was further mitigation for debonding as well as weighing down the casing to keep it from rising out of the borehole.

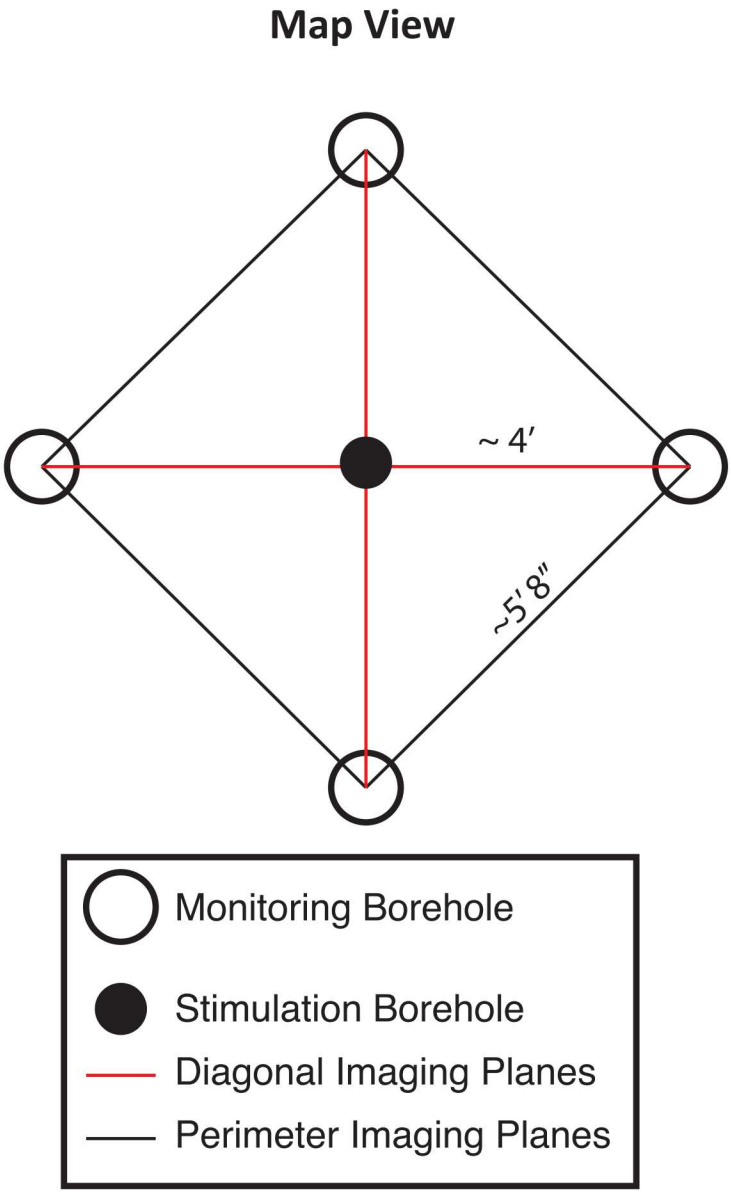

Figure 4.1. The center borehole (referred to as the stimulation borehole) was core, while the exterior monitoring boreholes were hammer drilled 4 feet off center of the stimulation borehole in each of the cardinal directions. The monitoring boreholes were cased with PVC, while the stimulation borehole had a much more intricate design (see Figure 4.2)

.

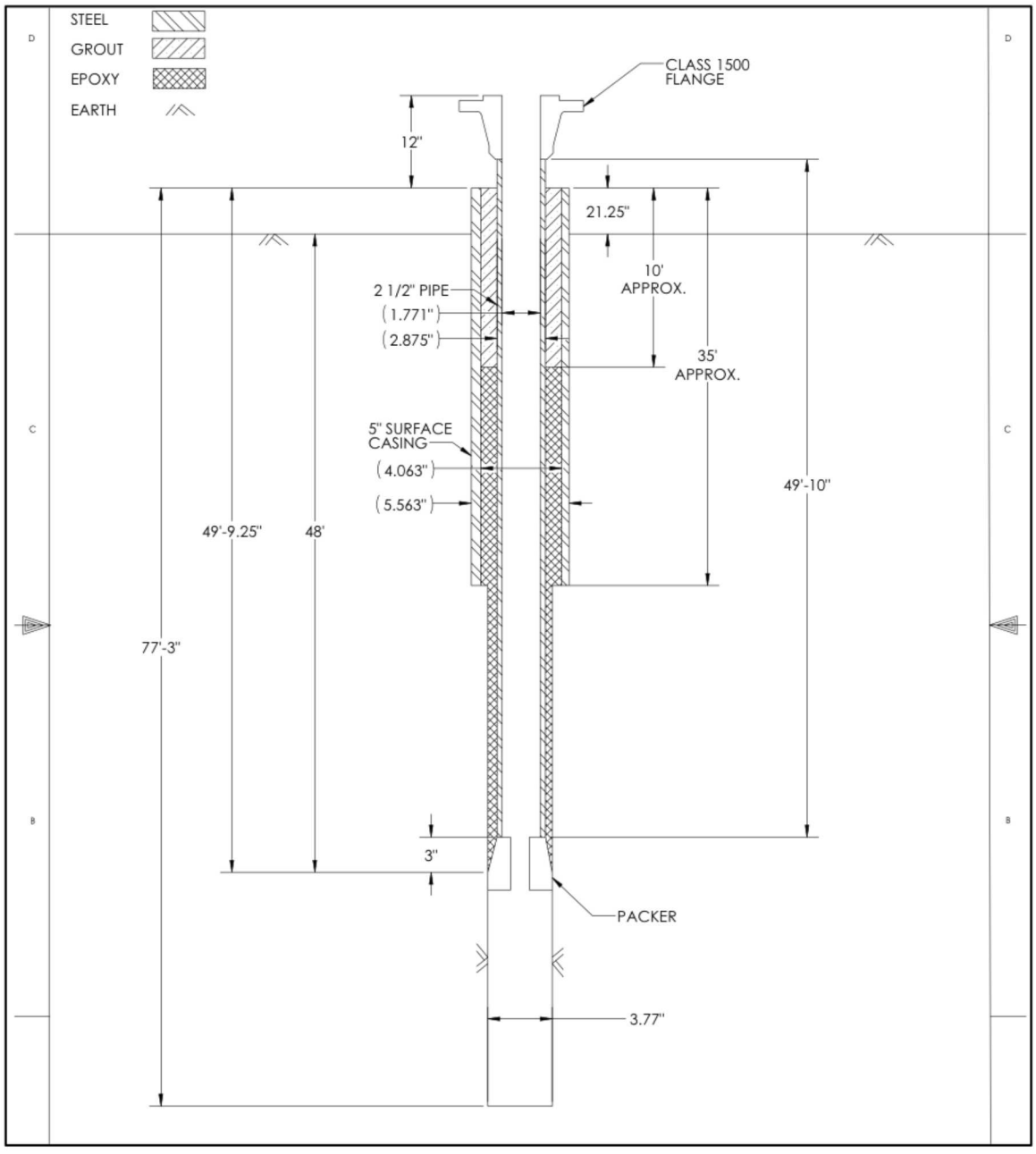

Figure 4.2. Engineering drawing of the stimulation borehole completion.

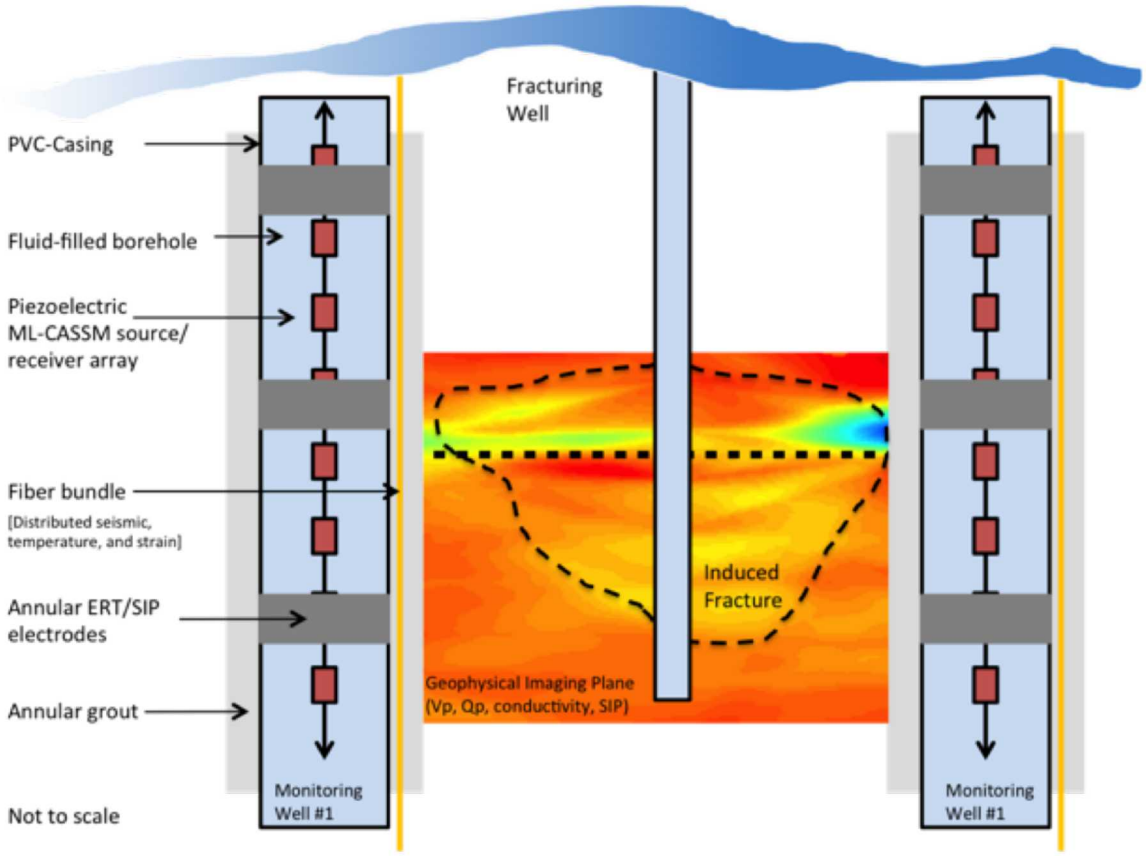

Figure 4.3. Conceptual model for monitoring borehole completion.

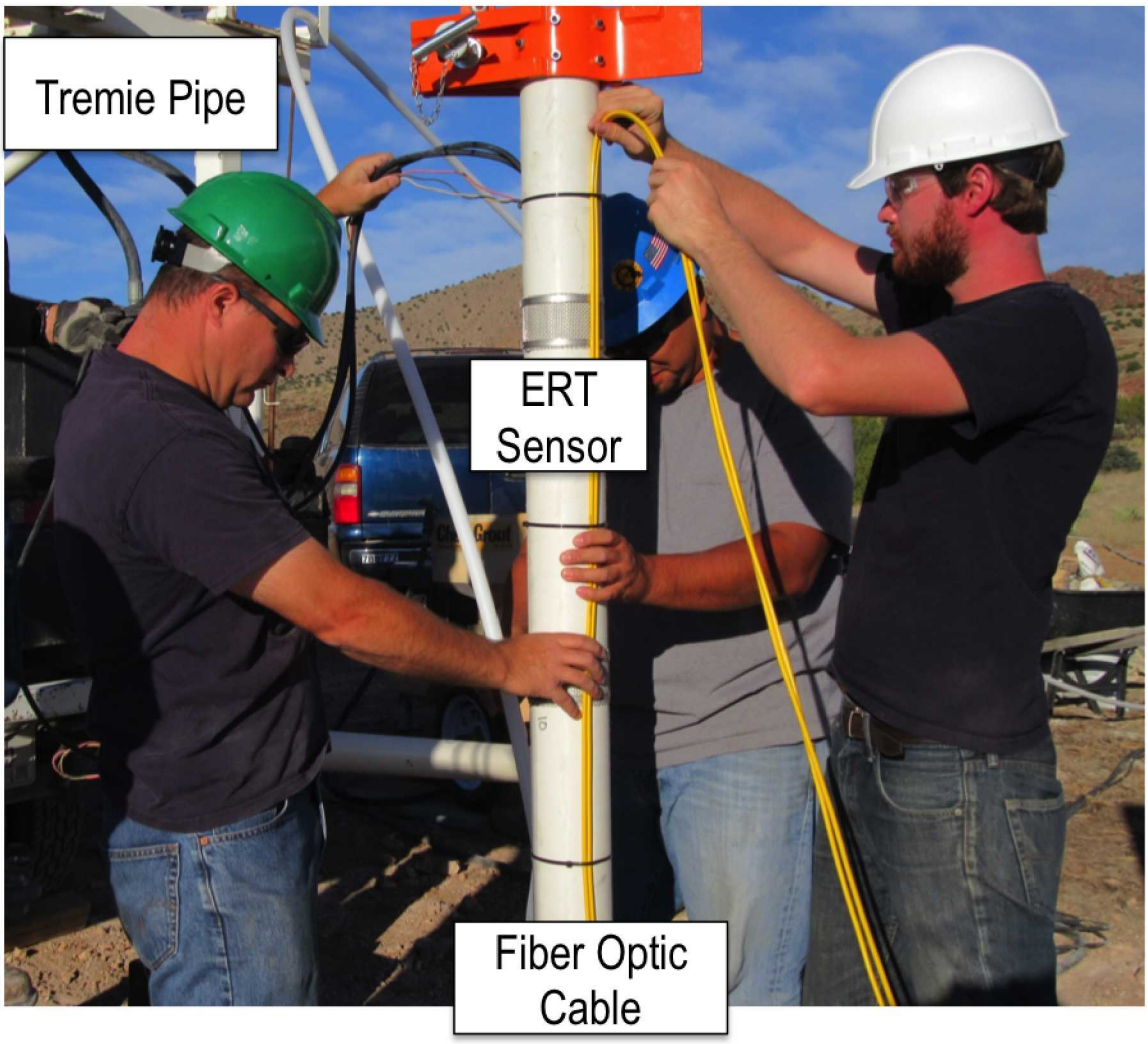

Figure 4.4. Image of casing installation showing that both distributed fiber and ERT measurement systems were secured to the outside of the casing. These instruments were later grouted in place using the tremie pipe shown and a custom grout mixture.

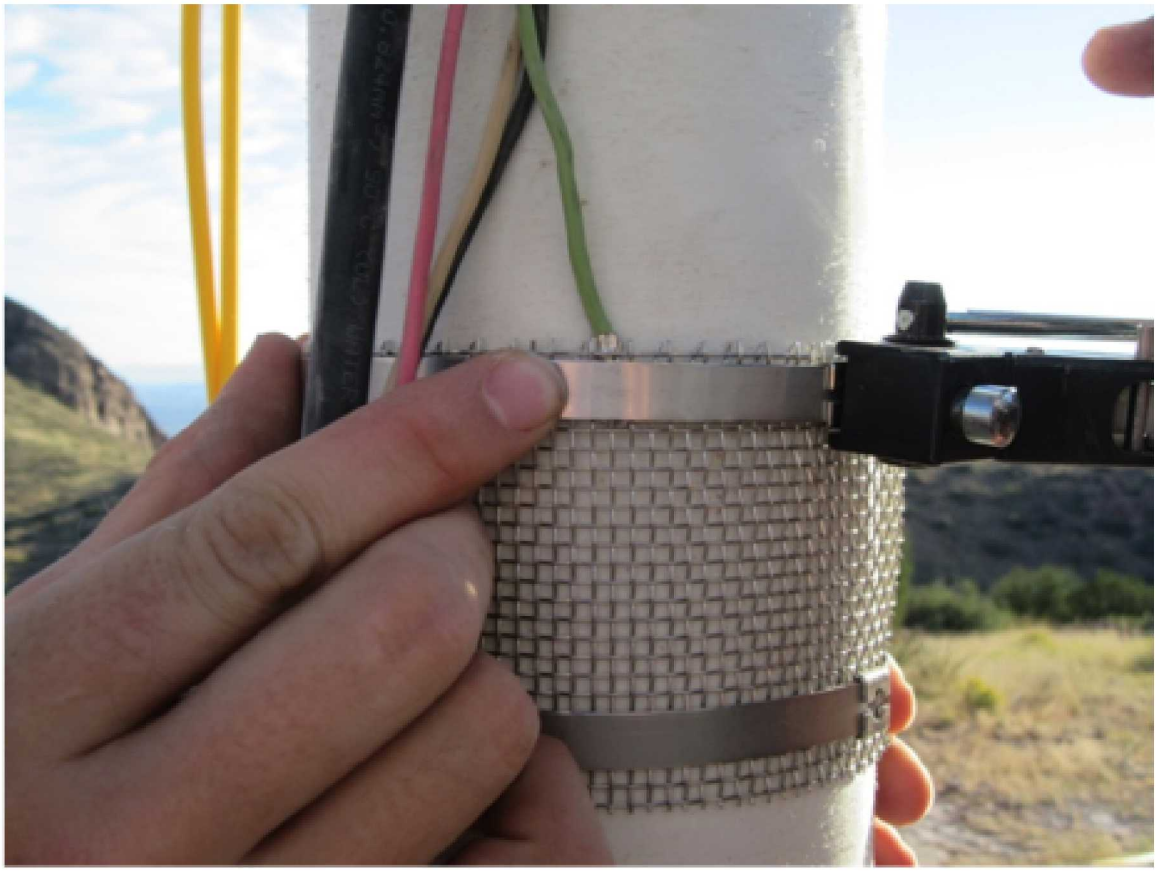

Figure 4.5. Image of ERT sensor configuration.

Figure 4.6. Fiber optic cable (distributed sensing) was deployed on the exterior of the casing. To avoid unnecessary splices in the cable, the cable was looped at the bottom of each monitoring borehole and secured with duct tape. This also provided twice as many DAS measurements in the boreholes.

Chapter 5

Field Test

During the weeks of April 11th and April 18th, 2016, the SubTER team performed the field test described in the subsequent sections. The initial planning for the field test required the construction of a conceptual testing timeline (see Figure 5.1). The team worked diligently in this phase to optimize the temporal and spatial resolution of the testing in this conceptual model. Furthermore, it was at this time that the team decided to leverage this opportunity to investigate the efficacy of explosive re-fracturing, which expanded the field test slightly. The team also took this opportunity to define more quantitatively the pressure testing steps (e.g. the fracture flexure experiment and the hydraulic testing). Once the conceptual timeline was constructed, the team took the opportunity to internally review the plan to verify that we had maximized the opportunities for multi-phenomenological studies.

Once the conceptual model was complete, the team began construction of a detailed Gaant chart to outline the relative positions of tasks for the field test (see Figure 5.2). This rigorous evaluation allowed for identification of 1) relative position of tasks, 2) the time allotments for giving tasks, and 3) the ownership of the tasks. This exercise proved essential for staying on task and determining who should be performing tasks at the wellhead and the monitoring boreholes.

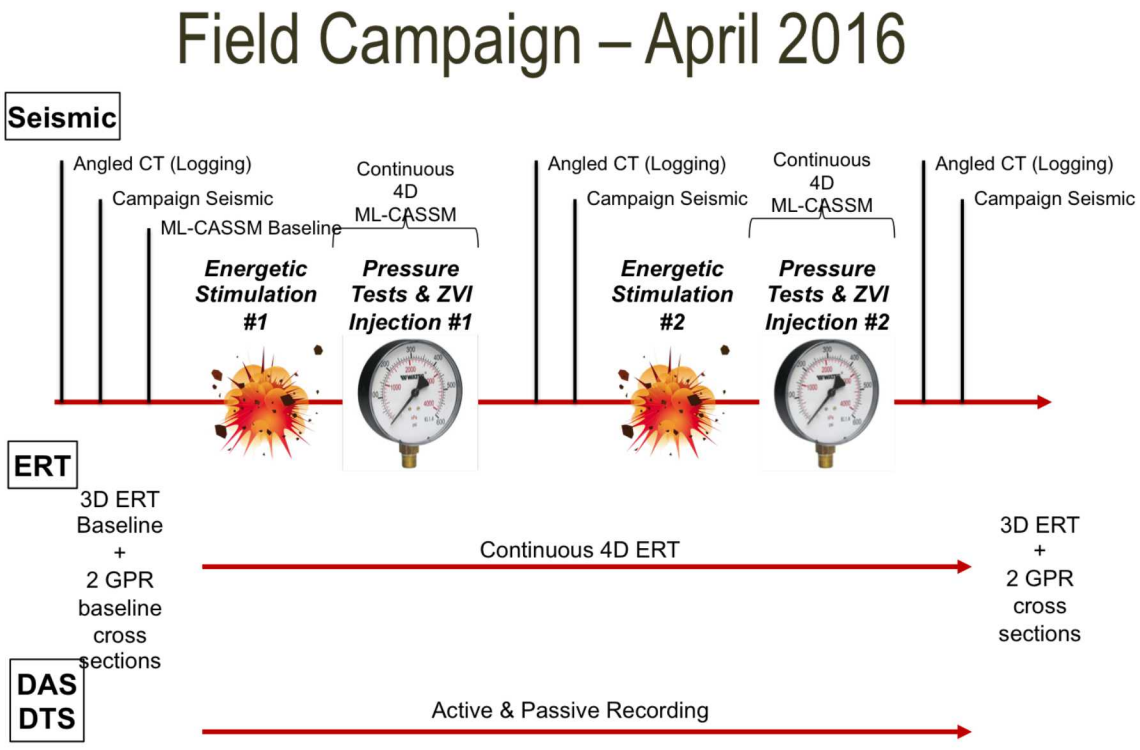

Figure 5.1. The conceptual experiment plan was constructed to maximize both the temporal and spatial resolution of each of the surveys, to capture the changes induced by both explosive fracturing events and the associated pressure injections, and to provide as many opportunities to compare multi-phenomenological datasets.

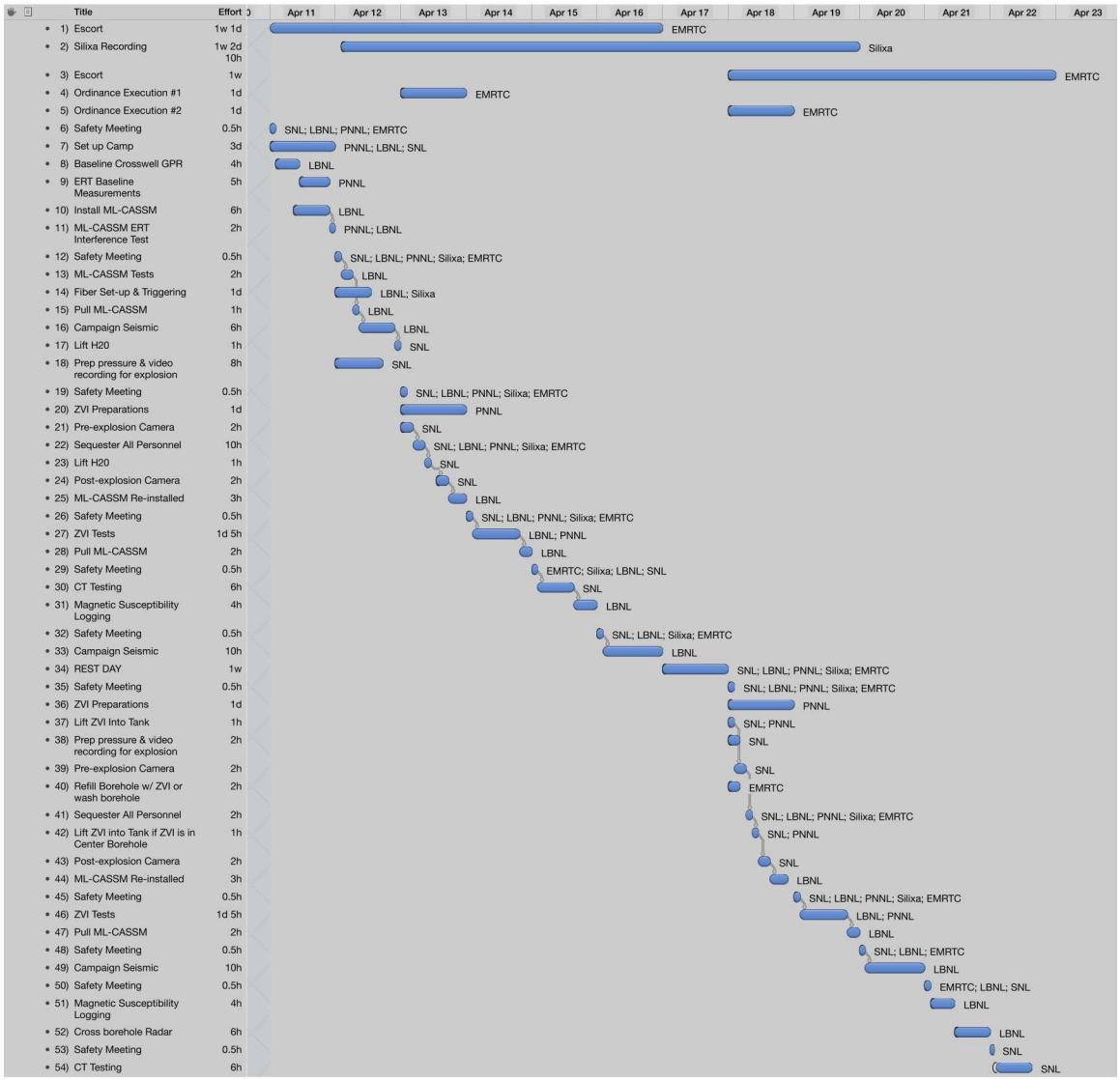

Figure 5.2. Gaant chart for field test. Note that the execution of this test was completed one day early. The relative timing of the tasks, however, is accurate.

Chapter 6

Pressure Tests

A series of hydraulic tests were conducted within the central borehole, both before and after energetic stimulation, to quantify the magnitude of change in formation permeability associated with the stimulation activities. Three separate hydraulic tests were conducted, one prior to stimulation, one after the first detonation, and one after a second detonation. Although a pre-stimulation hydraulic test was conducted, processing and analysis of these data was not completed in time for inclusion in this report; instead, book value estimates are used here for comparison. The post-stimulation hydraulic tests were conducted as constant-rate injection tests and the pressure falloff portion of the response curves were analyzed to provide estimates of hydraulic conductivity and permeability. Wellhead pressure was monitored with an Omega DPG409 Series high accuracy digital pressure gauge and flow rate was monitored with a Badget Meter, Inc. ModMAG M-2000 electromagnetic Flow Meter; both data streams were continuously monitored and recorded using a Campbell Scientific, Inc. CR1000 datalogger.

Test response data were analyzed using AQTESOLVE Pro, a software package developed by HydroSOLVE, Inc. The analytical model used for post-stimulation test conditions was a solution developed by Gringarten and Witherspoon (1972) for vertical fracture configurations. The Agarwal (1980) time transformation was applied to all pressure falloff data so that these recovery data could be analyzed using standard analytical well-function models developed for analyzing hydraulic stress responses.

The initial post-stimulation pressure test (i.e., post-detonation no. 1) was conducted on April 18, 2016. This hydraulic test was conducted at a constant injection rate of 1.27 gpm for a duration of 95 minutes. Care was taken to avoid any external pressure perturbations at test termination and pressure falloff was monitored throughout the recovery phase of the test. The observed pressure falloff and type-curve fits are shown in Figure 6.1. This plot shows the pressure falloff data and data derivative plotted along with the Gringarten and Witherspoon (1972) type curve. The selected model provides a reasonably good fit to the data and indicates an estimated hydraulic conductivity of 0.05 ft/d.

Following a second detonation, another post-stimulation pressure test was conducted, also on April 18, 2016. This hydraulic test was conducted at a constant injection rate of 1.44 gpm for a duration of 80 minutes. Again, care was taken to avoid any external pressure perturbations at test termination and pressure falloff was monitored throughout the recovery phase of the test. The observed pressure falloff and type-curve fits (same model as above)

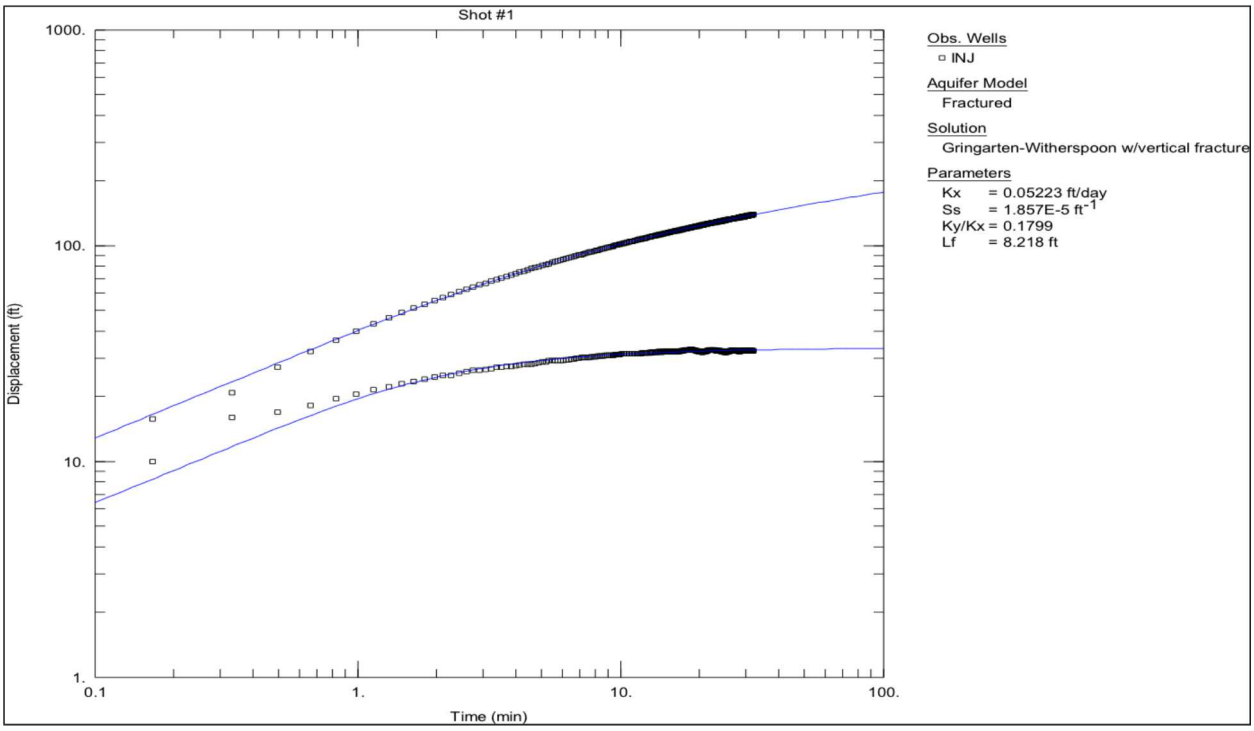

Figure 6.1. Pressure falloff data and data derivative, and associated type curve fits, for post-detonation no. 1 test conditions.

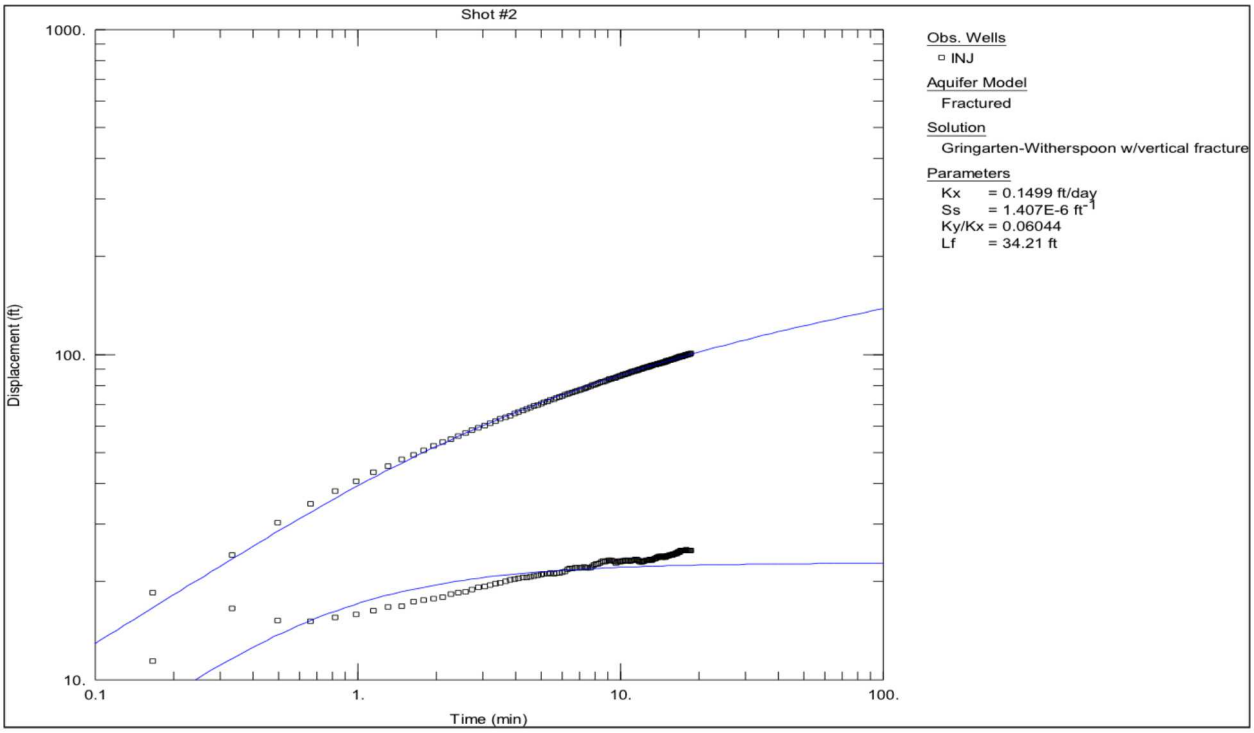

Figure 6.2. Pressure falloff data and data derivative, and associated type curve fits, for post-detonation no. 2 test conditions.

are shown in Figure 6.2 . In this case the model also provides a reasonably good fit to the data from the post-detonation no. 2 test; the type curve match indicates an estimated hydraulic conductivity of 0.15 ft/d. It is worth noting that the model fit indicates an increase in fracture length between the first (∼8 ft) and second (∼30 ft) detonations. Additional sensitivity analysis would be needed to determine just how sensitive the solution (and model fit) is to this parameter. However, the estimated changes in hydraulic conductivity and fracture length are both consistent with increased fracture propagation associated with the second detonation. A comparison of baseline and post-stimulation permeability estimates are provided in table 1. Baseline conditions are estimated based on a typical range of values for unfractured metamorphic and igneous rocks (Freeze and Cherry, 1979). The relatively low permeability values represented by this range are consistent with the observed baseline pressure response, which indicated a very low permeability condition. As shown in Table 6.1, the initial detonation increased the permeability of the host rock by several orders of magnitude, and the second detonation was able to further increase the permeability by almost 200%.

Table 6.1. Comparison of baseline and post-stimulation permeability values.

	Hydraulic Conductivity (ft/d)	Permeability (md)
Baseline Conditions	7E-5 to 3E-9	2E-2 to 1E-6
Post-Detonation #1	0.05	18
Post-Detonation #2	0.15	55

Chapter 7

Open Hole Characterization

Introduction

A geophysical borehole logging program was designed and executed to characterize site variability in lithology, texture, existing fractures, borehole break-out, diameter, and orientation utilizing industry standard borehole geophysical tools such as deviation, caliper, spectral gamma, and optical televiewer. The scientific goal of the logging effort was to identify subsurface features which might influence the propagation or structure of the induced fracture network. A complementary goal was to provide secondary datasets to improve the quality of our timelapse geophysical inversions; borehole deviation logs in particular were required to properly locate ERT electrodes as well as the CASSM source/receiver arrays. A last component of the logging effort was timelapse analysis of magnetic susceptibility to attempt to track proximity of the ZVI injection to the monitoring wells.

Logging System

The logging tools selected for the characterization study were manufactured by Advanced Logic Technologies (ALT) and were deployed using a Mt. Sopris MX series portable wireline winch controlled with Mt. Sopris Matrix data recording technology. The MX series winch is a single conductor wireline that supplies the required power to each logging tool (sonde) and receives data along the same conductor and capable of logging boreholes up to 1000 meters deep. The integrated Matrix logging unit decodes the information from each sonde along with tracking the depth of the sonde at centimeter scales. The Matrix logging unit is controlled by the user with a separate laptop computer with Mt. Sopris logging software and appropriate individual sonde (tool) files that contain information on sonde length, power requirements, telemetry requirements, and available sonde configuration settings. In the Blue Canyon Dome study, deviation logs are particularly critical due to the planned crosswell monitoring experiments (seismic & ERT) and the very close well spacings.

In addition to the open-hole characterization sondes, a magnetic susceptibility sonde was deployed before and after the ZVI stimulation test to monitor any change in magnetic susceptibility. Increases in magnetic susceptibility were expected if generated fractures carrying

ZVI fluids invaded the sonde sensing zone around the borehole.

Methodology

The following methodology section will describe the background of each sonde and the resolution sampled.

Deviation Measurements : Borehole deviation was measured twice, once using a Mt Sopris QL40-DEV borehole deviation tool and a second time using the integrated deviation sensors on the QL40-OBI-2G optical televiewer. In both cases, sonde azimuth was estimated using a three component (3C) flux-gate magnetometer while inclination was measured using a 3C accelerometer. Measurements were made every 10 cm from top-of-casing (TOC) to the bottom of the borehole (∼1819 ∼1841.5 m MSL).

Caliper Measurements: Borehole diameter was measured using a 2PCA-1000 3-arm caliper while pulling the caliper up from the bottom of the well. Three mechanical arms attached are to the sonde assembly near the bottom of the sonde and flex in and out as the sonde is pulled up the well. A linear potentiometer monitors the position of the caliper arms as they move in and out with the diameter of the well. An internal microprocessor converts the signal to a frequency and sends the information up the wireline to the Matrix unit. The caliper can measure well diameters up to 42 cm. Measurements were made along the well every 5cm.

Spectral Gamma Measurements: Borehole spectral gamma measurements were made with a 2SNA-1000 Spectral Gamma sonde. This sonde measures gamma particles that did not fully react with matter as they travel from their source (usually clays). These particles are at low energy and are fully absorbed by the sonde gamma detector, a scintillator crystal. The radius of investigation is on the order of 30-60 cm.

Optical Televiewer Measurements: Borehole optical televiewer measurements were made with a QL40-OBI-2G optical televiewer from ALT. The OBI incorporates a high resolution, high sensitivity CCD digital camera with matching Pentax optics, located above a conical mirror that captures the reflection of the borehole wall. Each of the lights in the ring represents one pixel and azimuthal resolution settings can be set to 720, 360, 180 and 90 points per recorded circle. The lower the resolution the faster the logging speed. Images were taken every 0.029 cm along the length of the borehole. Optical televiewer logs for all four monitoring wells were acquired before completion to provide information on pre-existing fractures, textural variations, borehole variability, and other features of relevance prior to the fracture test.

Magnetic Susceptibility Measurements: Borehole magnetic susceptibility measurements were made with a HM-453 sonde from W&R Instruments. The W-R probe uses a pair of coils spaced 20 cm apart, and generates a 1.9345 kHz square wave which is transmitted into the surrounding rock material. The signal measured by the receiver coil is proportional

to the magnetic susceptibility of the host rock. A secondary coil and resistor capacitor network isolate this signal from the rock conductivity signal, which is measured at a much higher frequency (∼100 kHz). Magnetic susceptibility measurements represent a volumetric response of the surrounding host rock and can be acquired in less than 0.5 s. The HM-453 has a sensitivity range of $7x10^{-}6$ to 0.07 SI units.

Characterization Results

The results of the open-hole characterization is provided in the following section. In the summary deviation plot (Figure 7.1), X-Y deviations are observed to reach a maximum of ∼0.2 m relative to surface locations, which seems insignificant over 23m well depths but actually is a significant offset considering the close well spacings (<3m). The resulting deviation logs were integrated into our 3D model of the monitoring wells for use in future ERT and seismic inversions. Figure 7.1 shows the estimate bulls eye map-view deviations for the four monitoring wells (MW: N(1)/S(2)/E(3)/W(4)); unfortunately no deviation logs are available for the stimulation well, but significant deviations were not anticipated given that the stimulation well was core drilled rather than hammer drilled.

Other composite logs in Figures 7.2 and 7.3 showcase the results from multiple borehole geophysical tools that were collected in each borehole. In Figure 7.2 results from MW-N and MW-E are observed from a geophysical suite consisting of caliper, gamma-gamma, deviation, and optical televiewer logs. Caliper logs (magenta curve, Figure 7.2) from both MW-N and MW-E show a consistent sized borehole (∼13 cm) with little to no natural break-outs or drilling induced fractures. Gamma-gamma (orange curve, Figure 7.2) show minimal variations throughout the 23m borehole depth indicating a single dominant clay free lithology (Rhyolite). The vertical deviation logs (green, blue, black, and red) are shown in Figure 7.2 and again show a minor tilt of less than 2 degrees and deviation less than 0.25m. The last log in Figure **??** composite is the optical televiewer log. In both MW-N and MW-E a cobbly zone is observed from the bottom of casing (1822m) to ∼1826.5 m elevation followed by a section of grayish rhyolite (1829.5 m bottom). Below 1829.5m the rhyolite is typical reddish rock observed within the study area. Many natural bedding features such as contact or sealed fractures and textural variations or observed to ∼1841.5 m at the bottom of the borehole. These textural features are more apparent in MW-N vs MW-E which appears to have more dust on the borehole walls even after flushing.

MW-W and MW-S composite logs are shown in Figure 7.3 following the same layout in Figure 7.2. Caliper logs show a consistent sized borehole of about 13cm with no natural break-outs or drilling induced. Gamma-gamma show minimal variations throughout the 23m borehole depth indicating a single dominant clay free lithology. Deviation logs show minor tilting (<2°) and little deviation (<0.25m). Optical televiewer logs show a cobbly zone from 1822 to ∼1827m consistent with MW-N and MW-E and similar textural features to the bottom of the borehole (∼1841.5). Upon further inspection and image processing the believed drilling induced fracture from 1835 to 1838.5m elevation is appears to be mostly

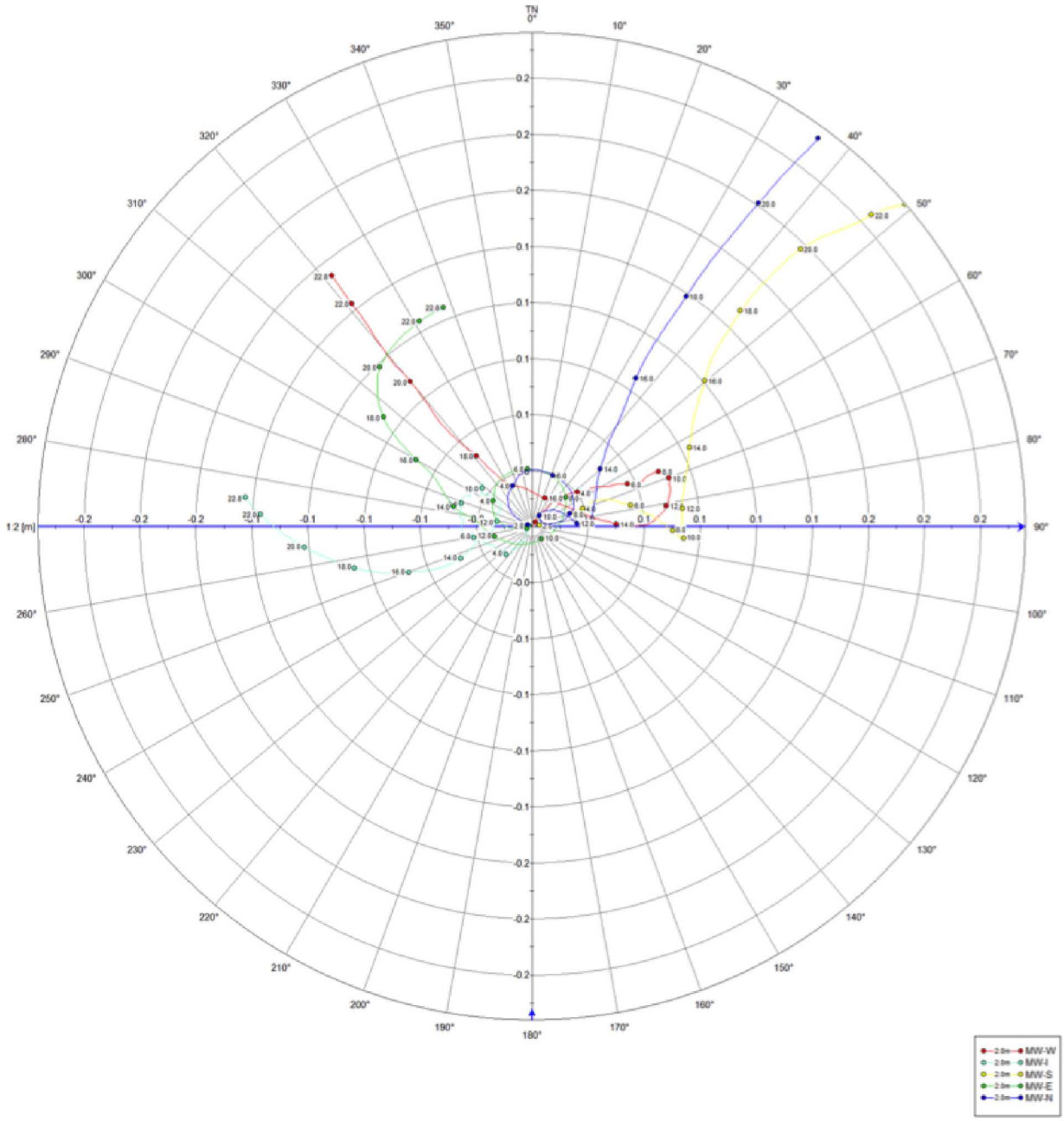

Figure 7.1. Combined deviation logs showing X-Y deviations referenced to the wellhead.

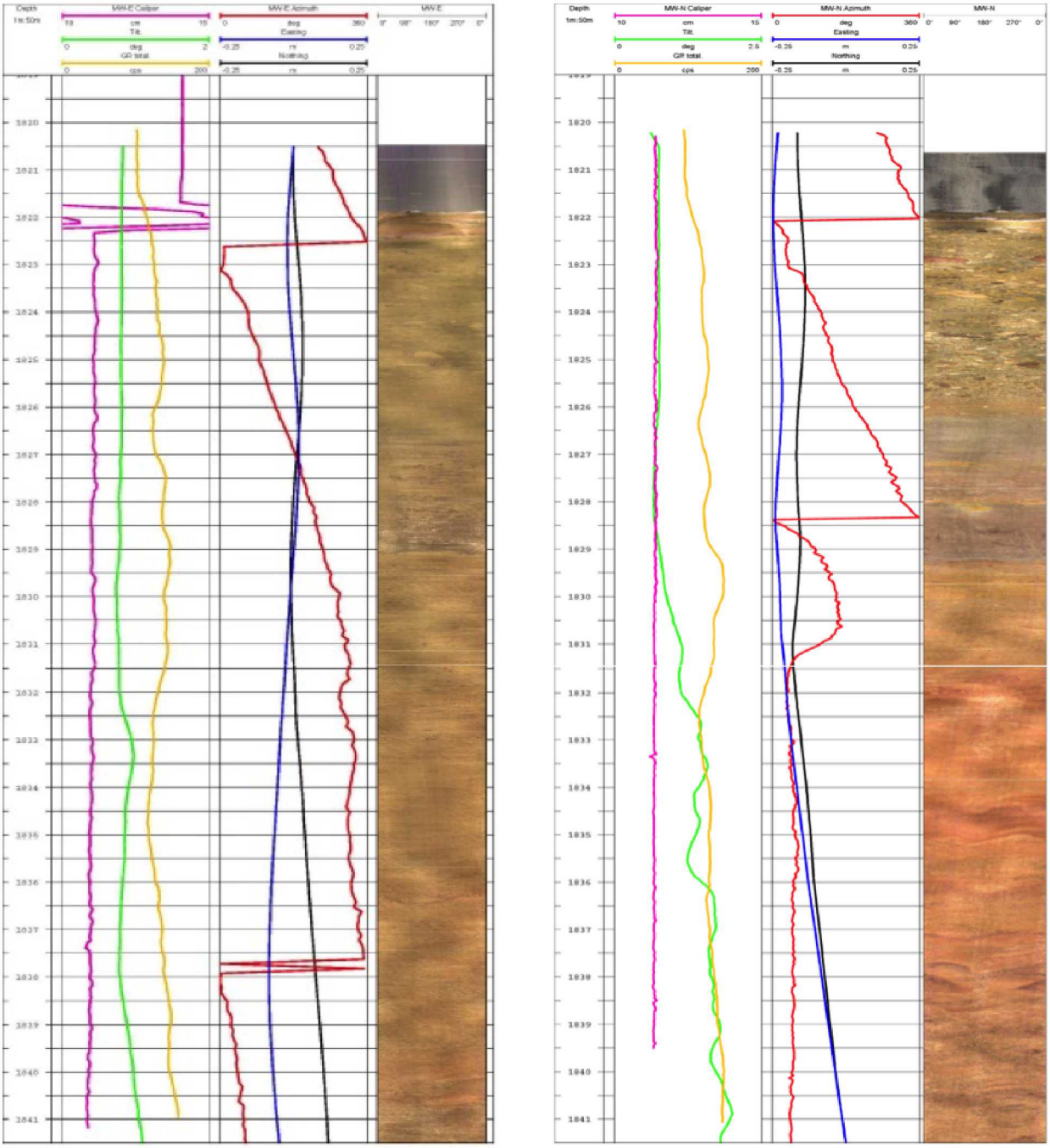

Figure 7.2. Composite log for MW-N (1) and MW-E (2) showing caliper (magenta), tilt (green), gamma (orange), azimuth (red), easting (blue), northing (black) and optical image.

surface staining in the image but there appears to be a horizontal open fracture at 1839.5m (Figure 7.3). Caliper data in the zone of this optical feature dont show any major increases in borehole diameter that we would expect from a larger looking feature like the one observed.

In summary, the boreholes were installed in a tight Rhyolite with some bedding/textural features but all of those appear to be sealed within the zone of interest. Minor tilting and deviation was observed.

Timelapse Logging

Prior to the center well stimulation and zero valent iron (ZVI) tracer injection magnetic susceptibility was collected in all four monitoring wells. Figure 7.4 shows the before (blue curve) and after (red curve) ZVI injection. The before and after curves are almost identical except for a zone from 1830m to 1834m where a small increase in magnetic susceptibility is observed. In the zone of the ERT electrodes (1834 to 1841m) the susceptibility sonde responds mostly to the metal ERT electrodes on the outside of casing. In MW-N from 1838.5 to 1841m a small increase can be seen. The magnetic susceptibility sonde appears to be responsive to the injected ZVI tracer but fractures likely didnt intrude close enough to the borehole to be within the sondes peak sensing zone. Thus we only see a minor increase in susceptibility. Figure 7.5 presents a couple photographs from the time lapse camera of the borehole logging process.

In conclusion, the open and cased hole logging programs provided depth-resolved lithological data as well as further constraints on the geophysical imaging studies. The rhyolite zone targeted for fracturing appeared to be largely homogeneous and fracture free while the installed well bores exhibited minor deviation. The timelapse magnetic susceptibility logging effort appeared to show minor responses to ZVI but was dominated by the effect of the ERT electrodes, a lesson learned for future studies.

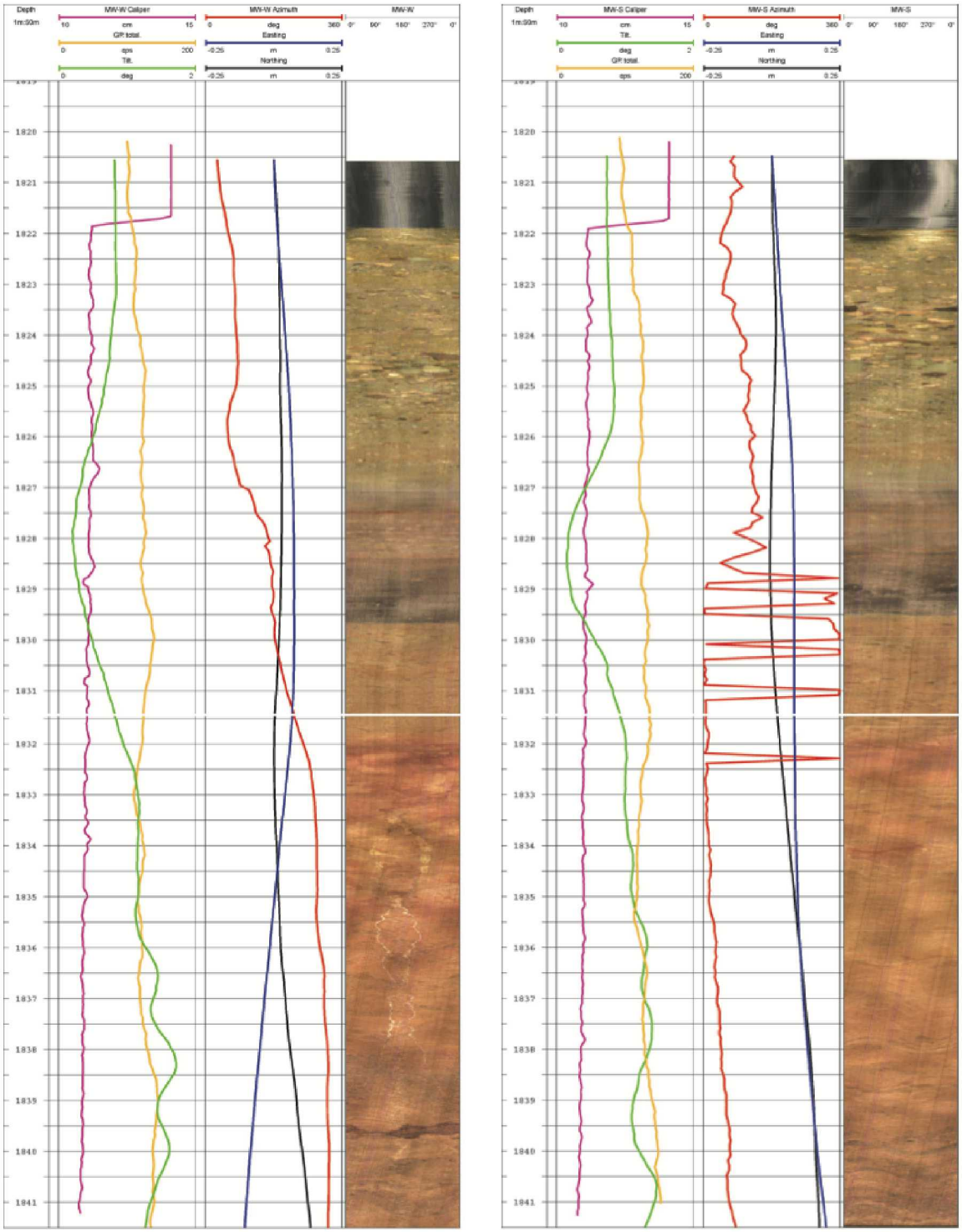

Figure 7.3. Composite logs for MW-W (3) and MW-S (4) showing caliper (purple), tilt (green), gamma (orange), azimuth (red), easting (blue), northing (black) and optical image.

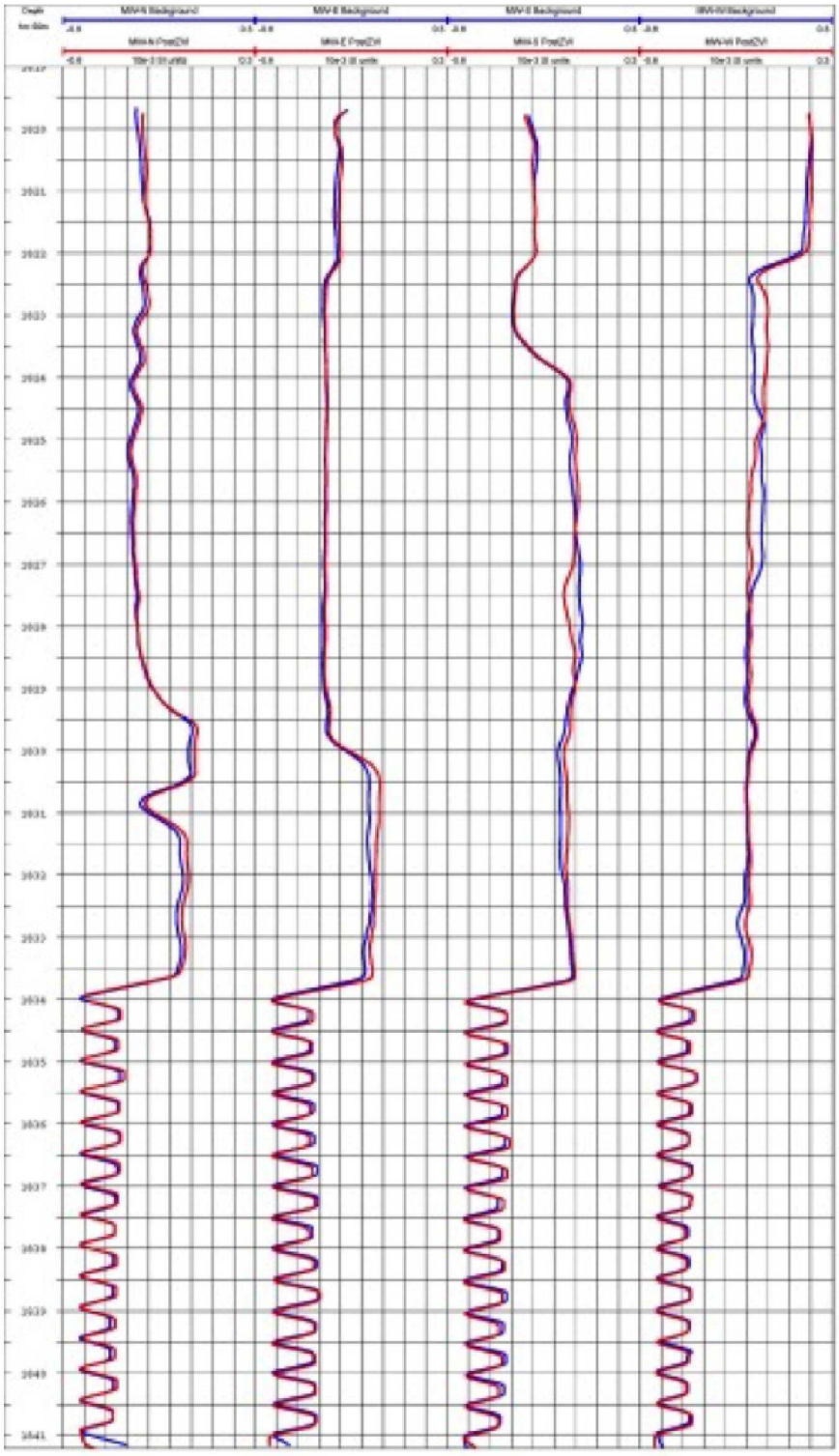

Figure 7.4. Composite magnetic susceptibility logs for MW-N, MW-E, MW-S, and MW-W showing the before ZVI injection (blue) and after ZVI (post) injection (red).

Figure 7.5. Logging operations at the Blue Canyon test pad during September, 2015 campaign.

Chapter 8

High Resolution Seismic Imaging

Introduction

While the coupling of crosswell seismic imaging and change detection techniques employed for imaging fractures is not in itself a major advancement, the novelty of the pilot study is concentrated around the use of a Non-Destructive Testing (NDT) tool. This tool allows for rapid data acquisition at unprecedented levels. For instance, we will show in the studies described below that we are able to achieve nominally three-inch to six-inch vertical resolution between the boreholes using more than 50,000 wave arrival picks to construct differenced tomograms. While this resolution is expected in laboratory settings, we are unaware of studies where this level of resolution has been achieved for in-situ tests to date. Each tomographic image (i.e. 25,000 waveforms) requires approximately 6.5 hours of field acquisition, 40 hours of analysis, and 40 hours of computation on a desktop style computer.

Testing Methodology

Crosswell Sonic Logging (CSL), as it is used in civil engineering applications (i.e. NDT), describes a seismic velocity profiling technique. Angled Crosswell Tomography (CT) testing, as it is used here, describes implementing multiple runs of CSL testing with vertical source-receiver offsets (Olson and Wright, 1989) . In essence, angled CT and traditional crosswell seismic testing produces similar raypath geometries even though the details of the data acquisition are markedly different.

The angled CT testing relies on a pair of piezoelectric hydrophones and a depth wheel to measure compressional wave velocity in the ultrasonic frequency band. The hydrophones, which have a center frequency of 42 kHz, are interchangeable as source and receiver. The depth wheel controls the resolution of the test and in this instance ensures that a signal is recorded between the two hydrophones every 0.56 inches along the entire length of the tested uncased boreholes. As mentioned above, the difference between angled CT and CSL is that for angled CT acoustic data are collected by performing angled testing at different offsets in each of the borehole combinations whereas CSL testing incorporates source and receiver positions at the same depth or horizontal plane. In the case study presented here,

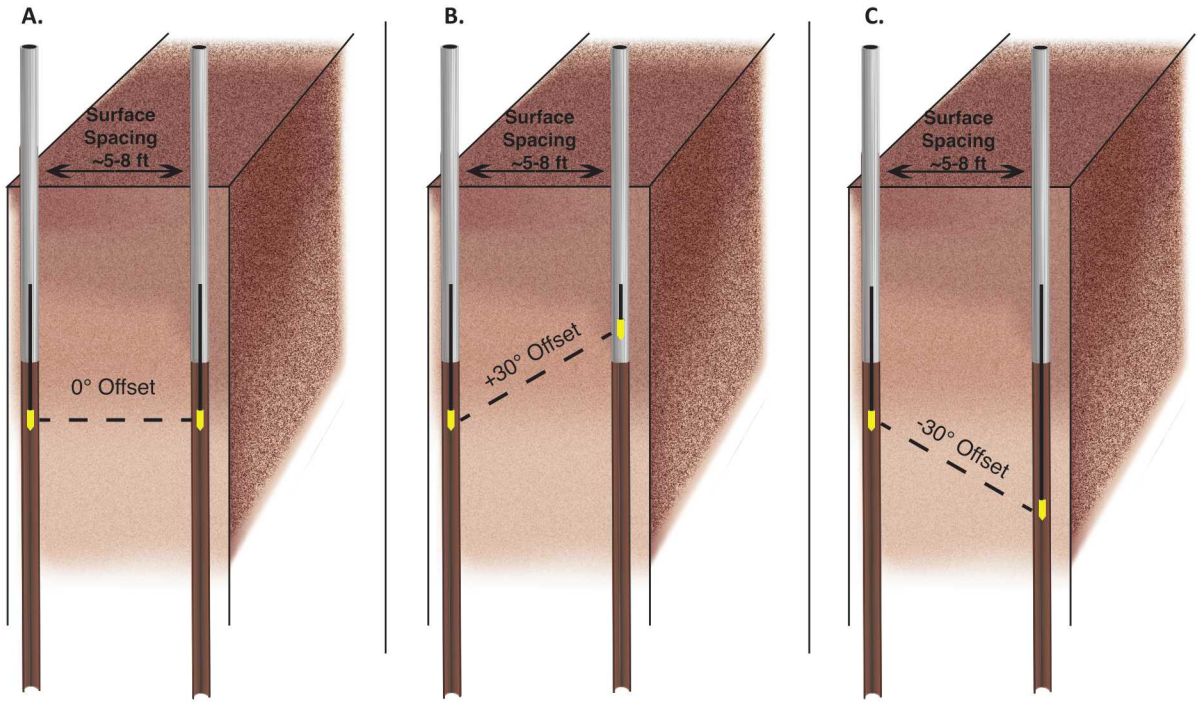

Figure 8.1. The angled CT testing was performed using Olson Instruments Crosswell Sonic Logging (CSL) system in four uncased drilled holes nominally 4 feet off center in the cardinal directions (see Figure 4.1). Testing was performed in all 6 available tube pairs. Nine logs (source-receiver offsets of 0°, +/-15°, +/-30°, +/-45°, and +/-60°) were acquired between each tube pair for a total of 54 logs. This figure illustrates the nature of the testing by showing three example hydrophone configurations for the testing. In practice, each of these configurations are conducted separately. For example, the tube pair would be logged with the configuration shown in A., the hydrophones would be offset by +30°, the tube pair would be logged with the configuration shown in B., the hydrophones would be offset by -30°, the tube pair would be logged with the configuration shown in C., etc. This would follow until all of the aforementioned angles had been acquired.

the angled CT testing around the stimulation borehole was performed at 9 different vertical source-receiver offsets for each tube pair (0°, 15°, -15°, 30°, -30°, 45°, -45°, 60°, and -60°). Figure 8.1 illustrates the nature of the CT testing between two tube pairs (see Figure 4.1). This testing was then

These data are acquired with a sampling rate of 500,000 points per second (2 s per point). Each log (i.e. between one tube pair and acquiring one angle) takes approximately 2 minutes to acquire. The total testing time for each one of these tests is only about 6.5 hours. It then takes approximately 1 week to pick the data and 2 days to perform the inversions. Each tomogram is constructed using approximately 25,000 picks over the 8x8x40 foot (2.44x2.44x12.2 m) volume. The targeted resolution, as determined by checkerboard tests, is on the order of 3-6 inches (76 mm-152 mm) in the vertical direction.

Resolution

We show in Figure 8.2 the tomographic resolution tests calculated for our acquisition geometry (see panel to the left). The input consists of a checkerboard with blocks that are 6 inches (152 mm) high and 24 inches (61.0 cm) wide. The relative velocity perturbations are 5% from background. Black lines are source and receiver positions in the recovered checkerboard test. There is no noise added to these tests, but we note that little change is seen until the picking errors exceed 10 microseconds in this case. This test reveals excellent pattern return except within about a foot of the top and bottom and to the left and right of the outermost source and receiver lines. Amplitude return is excellent in the center and drops toward the edges. We note here that checkerboard tests are indirect and idealized measurements and that further sensitivity testing needs to be performed on these datasets before the resolution can be definitively determined. This is, however, nontrivial given the large number of observations used to construct these tomographic images.

Test Timing

Complete angled CT datasets were acquired and analyzed a total of three times to characterize the stimulations for this test:

- Test 1: Imaged pre-explosion conditions
- Test 2: After first explosive fracturing
- Test 3: After second explosive fracturing

This testing design is required to isolate the changes induced by each of the fracturing events. Alternatively, one could have undertaken only Test 1 and Test 3 to get the total change from both stimulations.

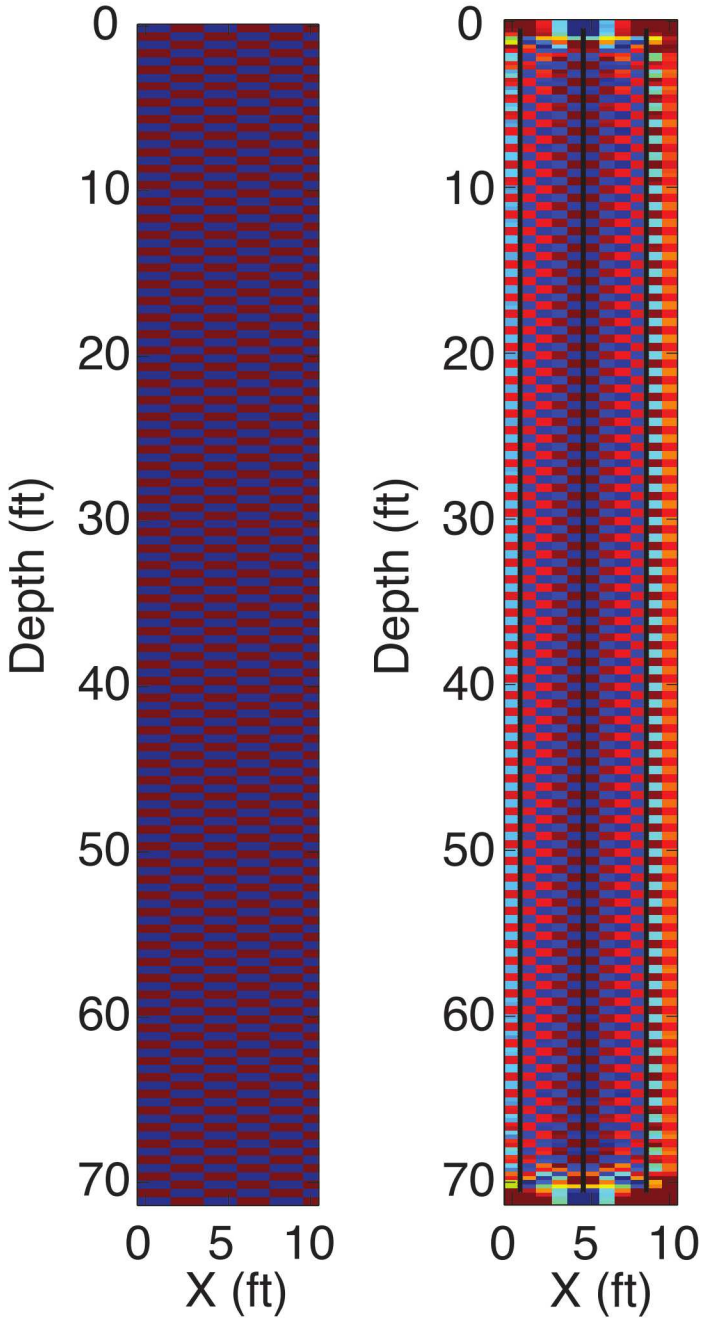

Figure 8.2. Computed resolution tests for the acquisition geometry described above.

Inversion Overview

The changes observed between tests can be visualized in a number of ways (i.e. changes in spectral content, coda duration, gathers, etc.). We have chosen here to provide the tomographic images from each of the tests computed with a Vidale-Hole finite-difference 3-D eikonal solver (Vidale, 1990; Hole and Zelt, 1995). Using this technique, there are two obvious choices in how to define the raypath geometry: 1) let the inversion of the data solve for the ray path geometry or 2) use the ray path geometry defined by the previous (in time) test. Initial testing during the seedling portion of this project evaluated which of these were most likely to highlight the changes induced by the stimulation events. This testing found that both techniques produced comparable results. It is hypothesized at this time, that this similarity is due to the very close offsets between the tube pairs. For the results shown below, we chose to iteratively solve for the raypaths for each test independently.

Observed Changes

The time-lapse tomographic images, representing the changes in P-wave velocity attributable to each of the energetic stimulations, provide a useful way of visualizing changes in subsurface structure and/or saturation. Here we have chosen to show two viewpoints of these changes (see Figures 8.3 and 8.4) along with the changes in the 4km/s isosurfaces (see Figures 8.5 and 8.6). We should note that in the cases of the 3D volumes, changes seen in P-wave velocity are attributable to structures running perpendicular to the view. For instance, this means that when observing the images from West to East, that changes are caused by fractures with a strike nominally North-South and visa versa. Also, note that in both viewpoints there is a complex starting velocity model with velocities greater than 5.5 km/s and lower than 3.5 km/s. The sharp boundary between these two end members likely represents a pre-existing steeply dipping fault. These types of structures have been observed else where at Blue Canyon Dome and are evident in some of the core sections taken from this site. However, there is no obvious evidence of this contact in the core from this stimulation borehole.

For the viewpoint South to North (see Figure 8.3), we observe the development of nominally three features from top to bottom. First, there is a horizontal feature (presumably a horizontal fracture) between 9-10m below ground surface. This strong P-wave velocity reduction is coincident with the known interface between the weathered and un-weathered rhyolite. The next feature is a general velocity reduction from the eastern edge to the western edge from approximately 10-14m below ground surface. Finally, the third feature is a near vertical feature that begins forming between A and B, and further intensifies between B and C. This feature is believed to be a nearly vertical fracture with a strike nominally East to West, although there is some indication that it is slightly Southwest to Northeast.

For the viewpoint East to West (see Figure 8.4), we also observe the development of the same aforementioned features. Between 9 and 10 meters, we can see the development of

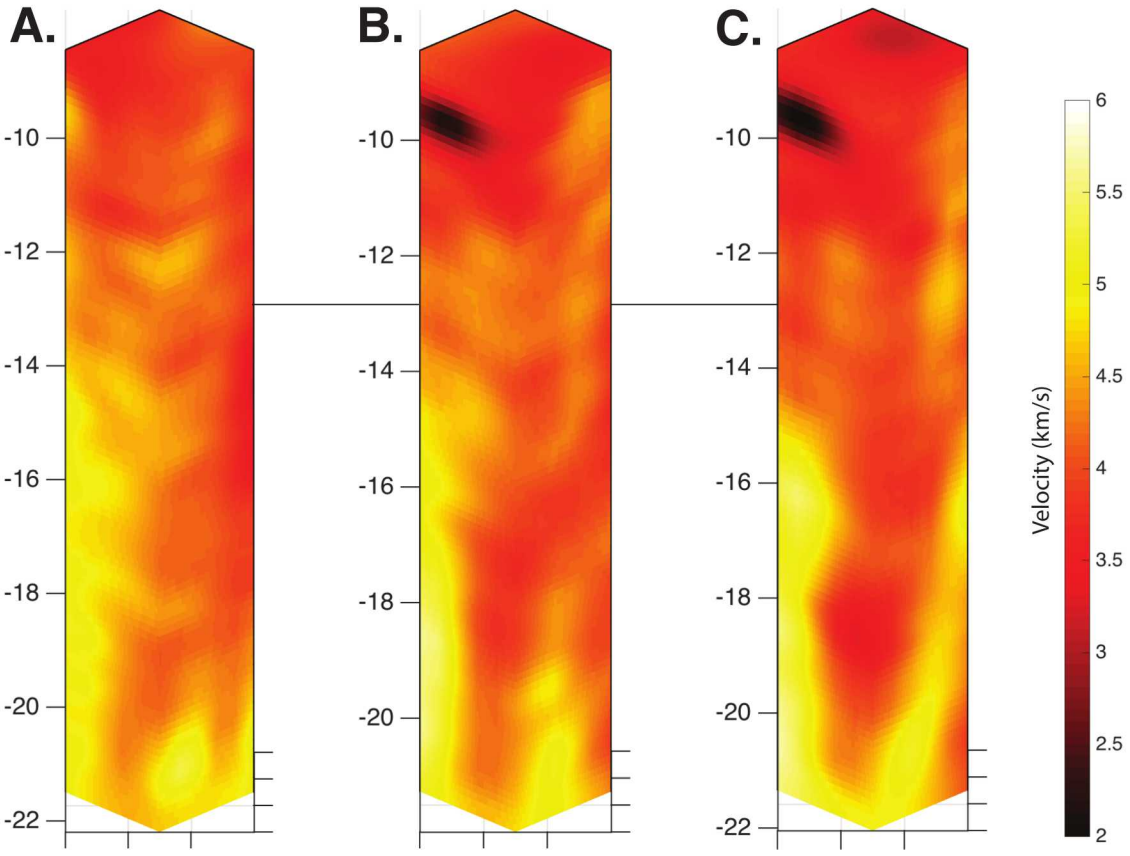

Figure 8.3. Tomographic image volumes displaying seismic velocity of the rock volume below ∼9m (35 feet). This view is looking South to North. The pre-shot conditions are shown in volume (A), post-stimulation #1 conditions in volume (B), and post-stimulation #2 conditions in volume (C). Comparison of the images shows a reduction in velocity at depths coincident with and above the stimulation depth (∼58-65', ∼17.5-20m). Also, a horizontal feature (seen as an elliptically shaped reduction in velocity) just above ∼10m (∼33') appears after the first stimulation and intensifies during the second stimulation. We note that the depth of this horizontal feature is coincident with the boundary between the highly fractured and the more competent rhyolite.

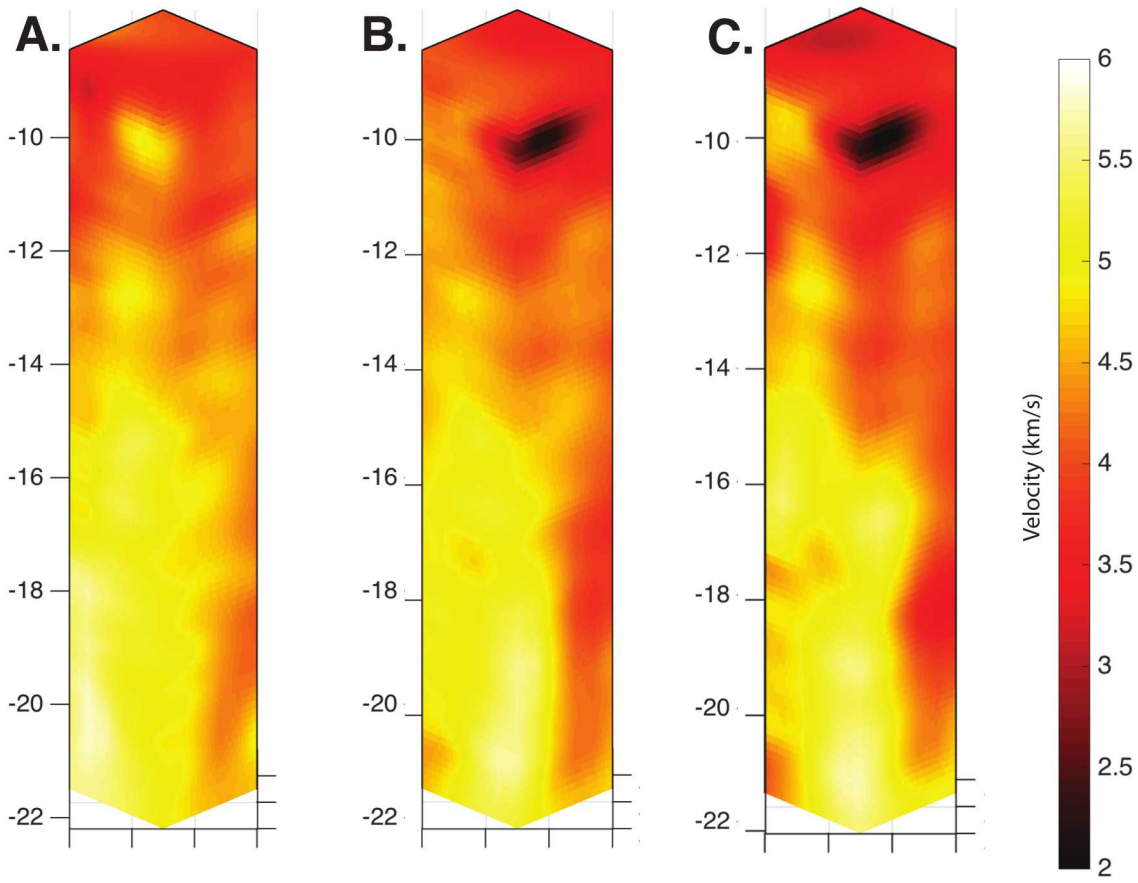

Figure 8.4. Tomographic image volumes displaying seismic velocity of the rock volume below ∼9m (35 feet). This view is looking East to West. The pre-shot conditions are shown in volume (A), post-stimulation #1 conditions in volume (B), and post-stimulation #2 conditions in volume (C). Comparison of the images shows a reduction in velocity at depths above the stimulation depth (∼58-65', ∼17.5-20m). Also, a horizontal feature (seen as an elliptically shaped reduction in velocity) just above ∼10m (∼33') appears after the first stimulation and intensifies during the second stimulation. We note that the depth of this horizontal feature is coincident with the boundary between the highly fractured and the more competent rhyolite.

the horizontal feature mentioned above. Here we see that the decrease in P-wave velocity between approximately 10 and 14 meters below ground surface is of the same approximate magnitude, which indicates that this feature is not entirely planar. Finally, we can see the same nearly vertical feature form between A-B and then intensify between B-C. This view further supports a slightly Southwest to Northeast strike.

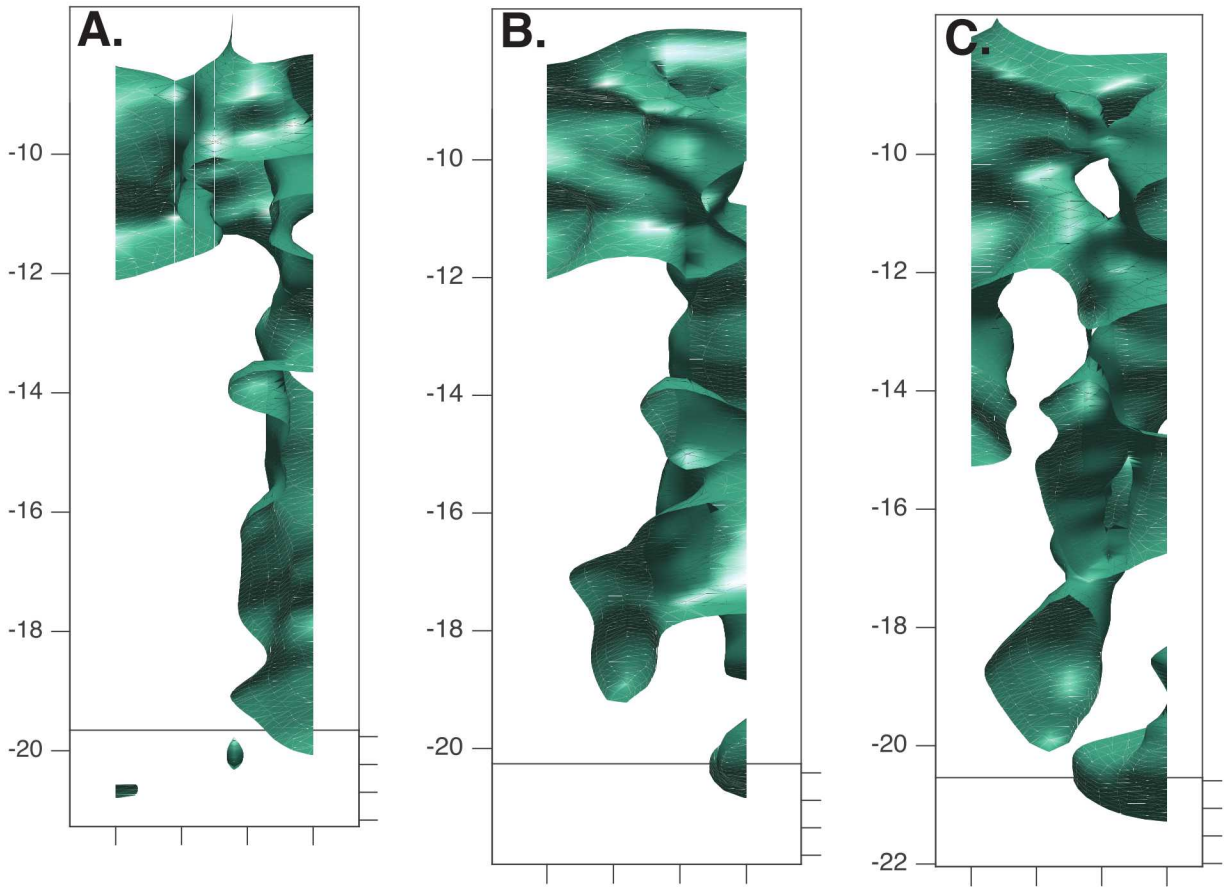

Figure 8.5. Isosurface highlighting the 4.0 km/s seismic velocity contour below ∼9m (35 feet). This view is looking South to North. The pre-shot conditions are shown in volume (A), post-stimulation #1 conditions in volume (B), and post-stimulation #2 conditions in volume (C). Comparison of the images suggests that a more volumetric fracture network developed above ∼12m, while a more planar feature (i.e. bi-wing fracture) developed below ∼12m.

Finally, we present here the two viewpoints with the 4km/s isosurfaces mapped for each stage (A-C; See Figures 8.5 and 8.6). This isosurfaces was chosen because it represents a 10% reduction from the mean velocity of the pre-stimulation conditions. While the details of these images should not be interpreted literally (i.e the boundaries of the fracture), they are illustrative in highlighting the areas where large changes occur. For instance, the development of the near vertical fracture is extremely evident in the South to North viewpoint (see Figure 8.5). Other changes mentioned above in the P-wave velocity models above are less obvious in this representation.

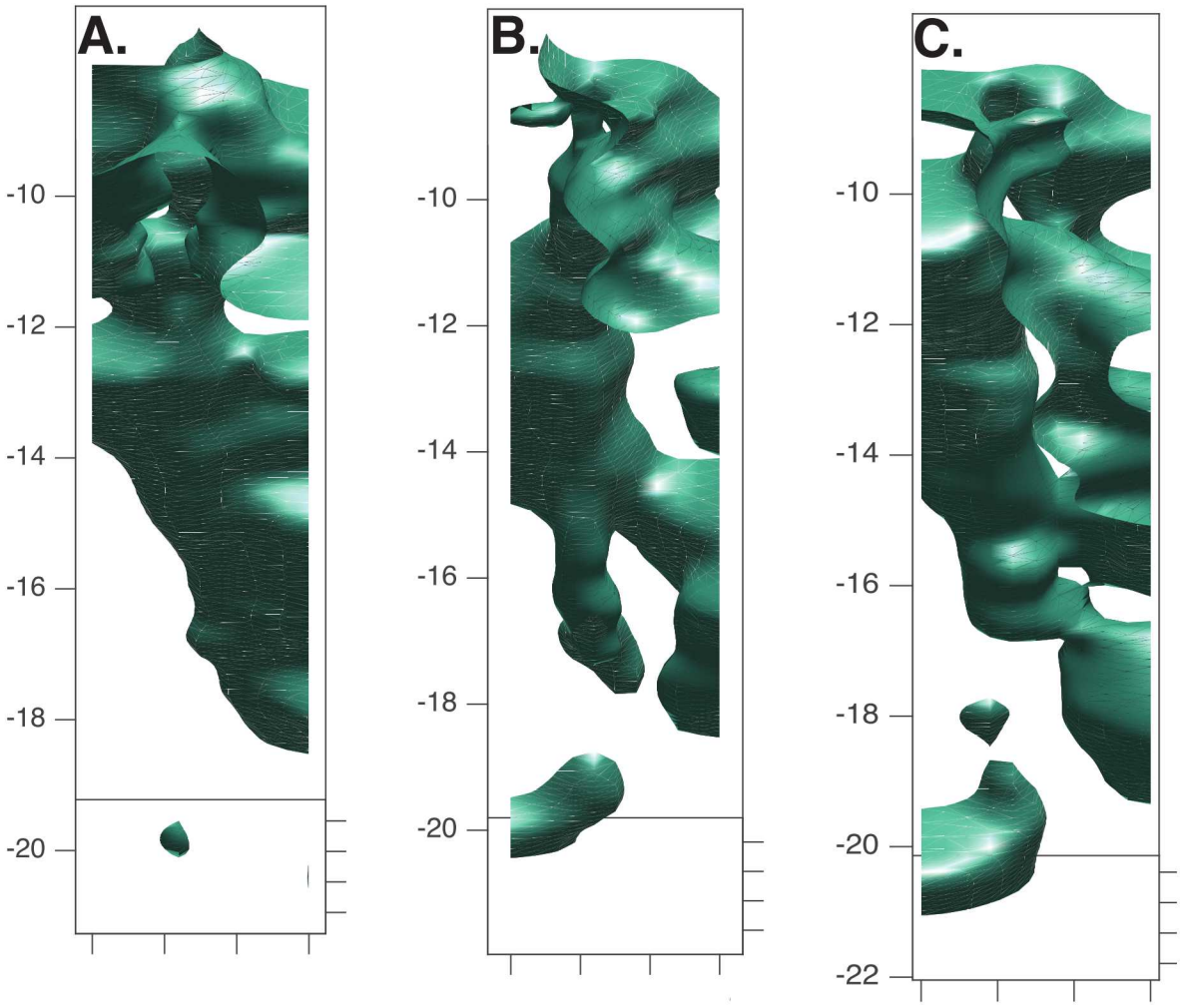

Figure 8.6. Isosurface highlighting the 4.0 km/s seismic velocity contour below ∼9m (35 feet). This view is looking East to West. The pre-shot conditions are shown in volume (A), post-stimulation #1 conditions in volume (B), and post-stimulation #2 conditions in volume (C). Comparison of the images suggests more minor (in comparison with Figure 8.5) changes occurred in this view. The changes shown here highlight the complex nature of these fracture systems and point to a potentially tortuous system. While it isn't as clear, the volumetric fracture network that developed above ∼12m can be identified with careful inspection.

Future Work

Future work pertaining to the angled tomography testing should occur four fronts to reach the goal of accurate real-time seismic tomographic imaging. First, the implementation of an accurate auto picker would reduce the time between the test and the development of the inverted images. Given that the actual acquisition time for this data is already fairly optimal, this is the next step in getting to actionable feedback. Ideally any auto picker rigorously developed for these purposes would be able to accurately pick in the presence of noise and would be useful for a variety of frequencies, source and receiver types, geologies, and offsets. The second front should be centered on inverting seismic data on a field computer, which of course requires that an auto picker has reliably identified the first arrivals. Given the current limitations of field computers (processors, RAM, etc.), the first demonstration of this capability should use similar approaches (i.e. field analysis of data, shipment of data to super computer, offsite-inversion, and finally retrieval of image in field) as the real-time ERT capability, which has proven successful in remote situations (i.e. this study). During the course of these efforts, the imaging technology should not be limited to traditional traveltime tomography, but should also consider anisotropic traveltime tomography and Full Waveform Inversion (FWI). The third set of efforts should be in equipment redesign. The Olson Engineering, Inc. system used here is an excellent candidate for short offset surveys (i.e. less than $\sim$3 meters or 10 feet). The system, however, is not capable of generating the frequencies or the amplitude required for seismic waves to traverse further source-receiver separations. While the ML-CASSM system, which was also used in this survey, is better suited for longer offsets, the system does not use a logging or encoded depth wheel technology. The logging style acquisition allows for much higher spatial sampling, while the ML-CASSM system allows for much higher temporal sampling. Each of these improvements has their place in change detection imaging of fracture networks. The fourth set of efforts should focus on the advancement of data visualization. In the case of enhanced reservoirs, the geometries and stark property contrast of the induced fractures is challenging to visualize in a way that actionable feedback can be determined from their interpretation. More R&D should be undertaken to determine what visualization is most useful for these systems.

Chapter 9

Multi-Level Continuous Active Source Seismic Monitoring

Introduction

Multi-Level Continuous Active Source Seismic Monitoring (ML-CASSM) is a recently developed technique which utilizes semi-permanent arrays of seismic sources and receivers, high speed switching, and automated data acquisition to acquire seismic surveys with both a high temporal resolution, currently on the order of 1 minute, and a high repeatability. In a typical crosswell ML-CASSM configuration, a sparse array of piezoelectric sources is used to generate seismic signals recorded by a hydrophone array; both remain stationary through the duration of the experiment yielding small crosswell datasets amenable to tomography, typically between every one and five minutes depending on stacking requirements. The high temporal sampling is due to the fact that no sources or receivers are moved during acquisition, hence the only limits on acquisition speed are record length, source switching speeds, and disk write requirements.

The same aspects which contribute to high temporal sampling, stationary S/R arrays, also contribute to high levels of repeatability since errors associated with source or receiver positioning are entirely eliminated. In cases where signal to noise levels are low, this high repeatability can be used in concert with massive vertical sampling to allow significant improvements in signal quality with stack coherence maintained beyond $1x10^5$ in downhole environments (Silver et al., 2007). Since the Cramer-Rao bound implies that differential traveltime accuracy is often bounded by S/N levels, high stack times can be used to allow detection of small signals using sub-sample accurate cross-correlation traveltime analysis (e.g. Silver et al. (2007); Niu et al. (2008)). To date, CASSM has been effectively used for detection of stress changes related to barometric cycles (Silver et al., 2007), $scCO_2$ movement (Daley et al., 2007), presumed earthquake precursors (Niu et al., 2008), and induced fractures in the context of near-surface hydraulic fracturing (Ajo-Franklin, 2012).

One notable limitation of ML-CASSM is that the datasets, while temporally dense, are often spatially sparse, often limited by the higher relative cost of seismic source fabrication in contrast with seismic receivers. While this limitation can be mitigated by effective regularization approaches (e.g. Ajo-Franklin et al. (2007)) or network geometry optimization

(e.g. Ajo-Franklin (2009)), the resulting spatial resolutions are somewhat lower than spatially dense campaign acquisition efforts using the same class of sources and receivers. A second challenge is the difficulty inherent in manual processing and parameter selection for the large data volumes generated by ML-CASSM acquisition; while manual picking is feasible for surveys with 2-3 time vintages, a survey with 2000 temporal epochs requires novel and largely automated approaches for processing and inversion.

At Blue Canyon Dome, the deployment of ML-CASSM was motivated by the short timescales under which flow and pressure alteration in fractures occur at the meter scale, typically on the order of minutes to hours. While the timescales of propellant or explosive fracturing (<100 ms) are outside of the reach of almost all active geophysical methods, flow experiments in fractures are experimentally accessible using techniques such as CASSM. In particular, we hoped to use CASSM to explore the seismic response of fractures as a function of stress perturbations induced by fluid injection, either water (e.g. a pump test) or tracer materials (e.g. ZVI). Access to this response could be potentially used to evaluate stress-dependent changes in permeability during injection and/or production when analyzed with the appropriate model. CASSM has already demonstrated this potential in prior deployments (e.g. Silver et al. (2007)) but never for discrete fractured systems over such short timescales.

In this section we will describe the completed work related to our ML-CASSM deployment at Blue Canyon Dome including system development, field deployment, field challenges, source repeatability, and preliminary analysis of the second pump test. The results, while not complete, indicate that the ML-CASSM system deployed is flexible, highly repeatable, and appears to measure variations in seismic response during pressure perturbations.

System Development

The ML-CASSM system fielded for the Blue Canyon Dome Pilot was built-for-purpose and, in terms of source and receiver count, the largest system constructed to date. The system included a 22 piezo-ceramic sources which were assembled into multiple borehole arrays. The sources were small 4" long radially-poled piezoceramic crystals which were air-backed and sealed with CNC-machined brass end-caps as can be seen in Figure 9.1 panels B and C. Given the relatively shallow depth of the pilot, the source design did not include pressure compensation and each source was deployed on a standard RG-58 coaxial cable, terminated in 5 KV coaxial connectors. The exterior of each source was also coated in a stiff protective epoxy layer to prevent crystal damage during deployment. For deployment at Blue Canyon Dome, the sources were grouped into two 10 level source arrays with single sources tied to the receiver arrays to allow single well data acquisition.

A second component of the system development effort was construction of a portable rack-based control and amplifier system designed for deployment in the Blue Canyon Dome field facility. The system consisted of two ruggedized 16U racks equipped with a control computer, D/A breakout subsystem, monitoring oscilloscope, high-voltage switching system,

Figure 9.1. Blue Canyon Dome ML-CASSM construction : Panel (A) shows the rack- mount control system during construction while panels (B) and (C) show the piezo-ceramic sources during assembly.

a DC power supply, and a high-voltage amplifier. The systems were tested in shallow wells at LBNL before being shipped to the Blue Canyon field site.

In addition to fabrication of the Blue Canyon Dome hardware, the project required an upgrade to the ML-CASSM control software developed during prior projects. The software, coded largely in MATLAB, handles source signal generation, D/A control, scheduling of the HV switch system, and triggering of the seismograph. As part of the Blue Canyon Dome effort, the control software was upgraded to handle 32 sources (formerly 16) and more flexible source encoding schemes.

Field Deployment at Blue Canyon Dome

The resulting ML-CASSM system was deployed at Blue Canyon Dome for the April 2016 fracturing pilot. At the time of deployment, the system was the largest ML-CASSM array assembled to date with 22 piezo-ceramic sources and 72 receivers positioned in the 4 wells surrounding the central fracturing well. Campaign crosswell data was recorded using the system before and after each fracture treatment and the system ran continuously during pump tests, ZVI injections, and during evening periods to explore both system repeatability

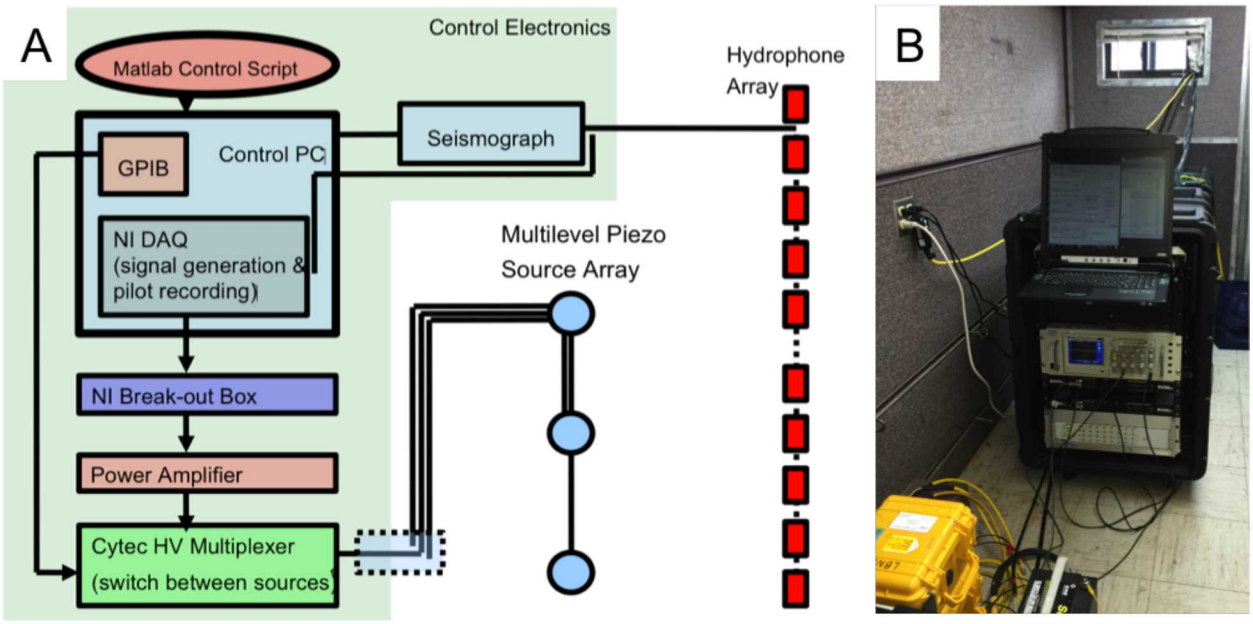

Figure 9.2. Panel A depicts the components of the ML-CASSM system while panel B shows the control electronics as deployed at Blue Canyon Dome

as well as natural barometric/tidal impacts on fracture response. Over the 1.5 weeks the system was active at the site, 55,000 gathers were recorded providing 2000 timelapse epochs with a peak temporal resolution of 1 minute. The system was removed from the wells during fracture emplacement to avoid potential damage to the piezoceramic sources and hydrophone arrays from the shock wave.

System Deployment And Geometry

Control electronics for the CASSM system were deployed in a instrument trailer supplied by Sandia. Figure 9.2 panel B shows the control rack and recording hardware as installed as well as a flow-chart depicting the system components in Figure 9.2 panel A. Control electronics included a 4U rackmount PC which ran the control software, triggered the seismographs, controlled the HV switch, and provided the analog source waveform. The source waveform was amplified by a custom 5 KV amplifier based on an IGBT array. Switching between sources was accomplished using a high-voltage coaxial switching fabric controlled by a serial interface (Cytec). All seismic datasets were recorded on three 24 channel Geode seismographs (Geometrics) triggered by the CASSM control computer.

As mentioned previously, the seismic sources were bundled into two 10 source arrays. A single source was included on each hydrophone array to provide information on tube wave propagation and potentially single well scattering data. Since each source was deployed

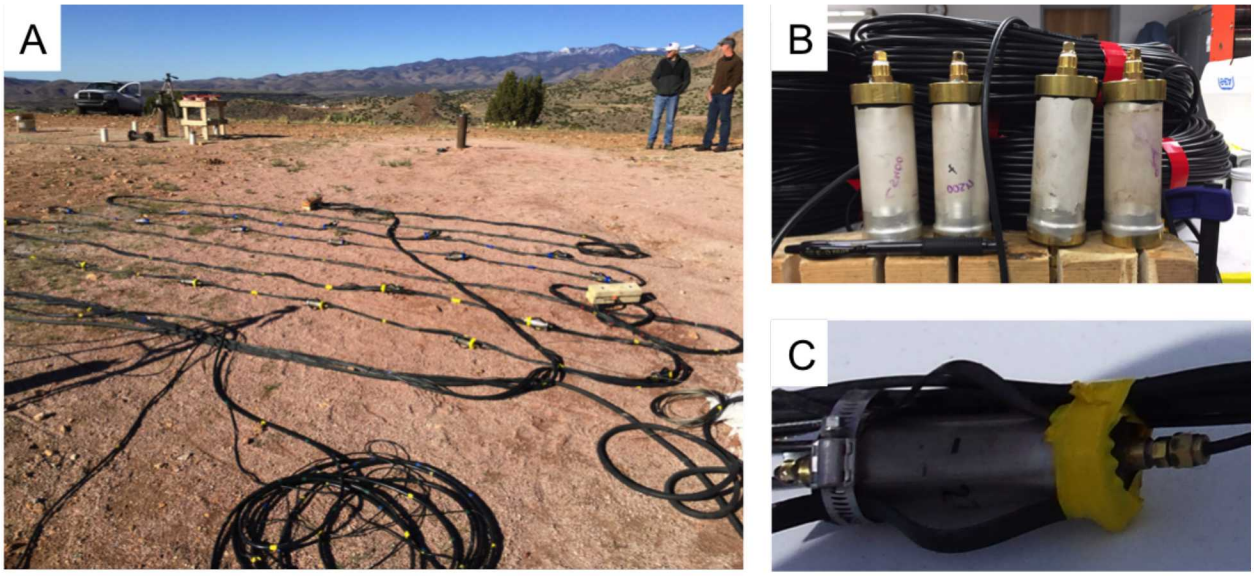

Figure 9.3. ML-CASSM source arrays in the field : Panel (A) depicts two 10-level source arrays unspooled while panels (B) and (C) show unfinished and deployment-ready sources respectively.

on an independent RG-58 cable, the entire assembly was strapped together to maintain a vertical source spacing of 1 meter spanning wireline depths between 12.9 and 21.9 m; both arrays, unspooled on the surface, can be seen in panel A of Figure 9.3. Each source was also fit with plastic centralizers before deployment to ensure repeatable lateral positioning in the borehole (Figure 9.3 panel C), a useful component considering the short offset of the monitoring wells and the effect of small location errors on traveltime repeatability.

After source assembly, the source and hydrophone arrays were deployed in the four monitoring wells surrounding the center fracturing well. For the majority of the experiment, source arrays were deployed in the south (3) and west (4) wells with hydrophone arrays in the north (1) and east (2) wells. This geometry provides four crosswell planes during each temporal acquisition including two diagonal planes which cross the fracture zone (North/South and East/West). The hydrophone arrays were 24 and 48 channel systems with 1/2 m vertical spacing; they were deployed in the north and east wells respectively. As can be seen in Figure 9.4 panel A, the source and receiver arrays also span the target zone vertically and provide reasonable angular coverage except at the very bottom of the array where the lack of a rat-hole resulted in only horizontal ray-paths. During execution of the CASSM surveys, the arrays were held motionless using a set of wooden clamps. The source/receiver system as deployed can be seen in Figure 9.4 panel B.

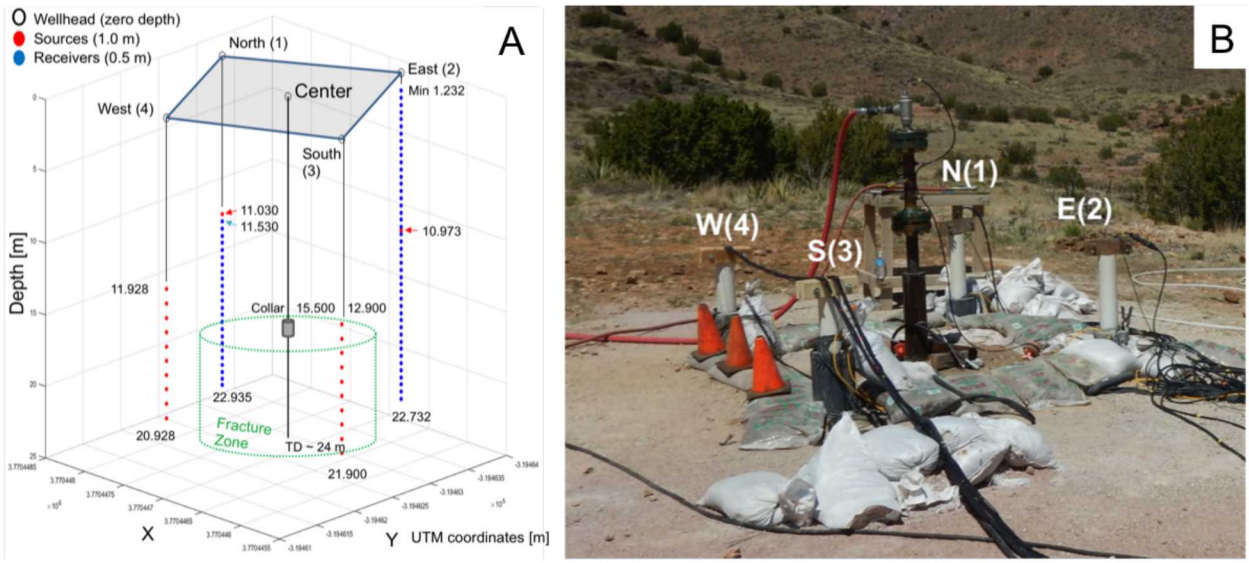

Figure 9.4. Schematic geometry (panel A) and surface photograph of the ML-CASSM system as deployed at Blue Canyon Dome.

Challenges in field acquisition

While the ML-CASSM system was successfully deployed, a variety of issues resulted in non-optimal data quality. One of the most persistent problems was the high surface wind speed at the site which coupled into both tube waves in the boreholes as well as traveling cable modes on the hydrophone arrays. Wind speed was variable (0-40 mph) and the wind-induced borehole modes were considerably higher amplitude than stacked data from the piezo-electric sources. Attempts were made to minimize coupling to tube waves through use of attenuating foam packed into the top meter of the well. While this modification decreased wind effects and cable modes, significant residual noise was still present. Fortunately, the noise was effectively suppressed through application of a large time-domain pad (1 s), slow taper, and a high-pass filter with corners at 400 and 500 Hz. Figure 9.5 shows an example of this wind suppression step. Secondary challenges during deployment included power brown-outs, mitigated using dual UPS systems, and the need to re-deploy the arrays between fracturing steps.

Preliminary Results from Blue Canyon Dome Field Test

To date, only preliminary processing has been performed on the extensive dataset acquired at the Blue Canyon Dome site. The bulk of the 55,000 gathers acquired during the experiment were, after processing, of sufficient quality for subsequent analysis. Initial pro-

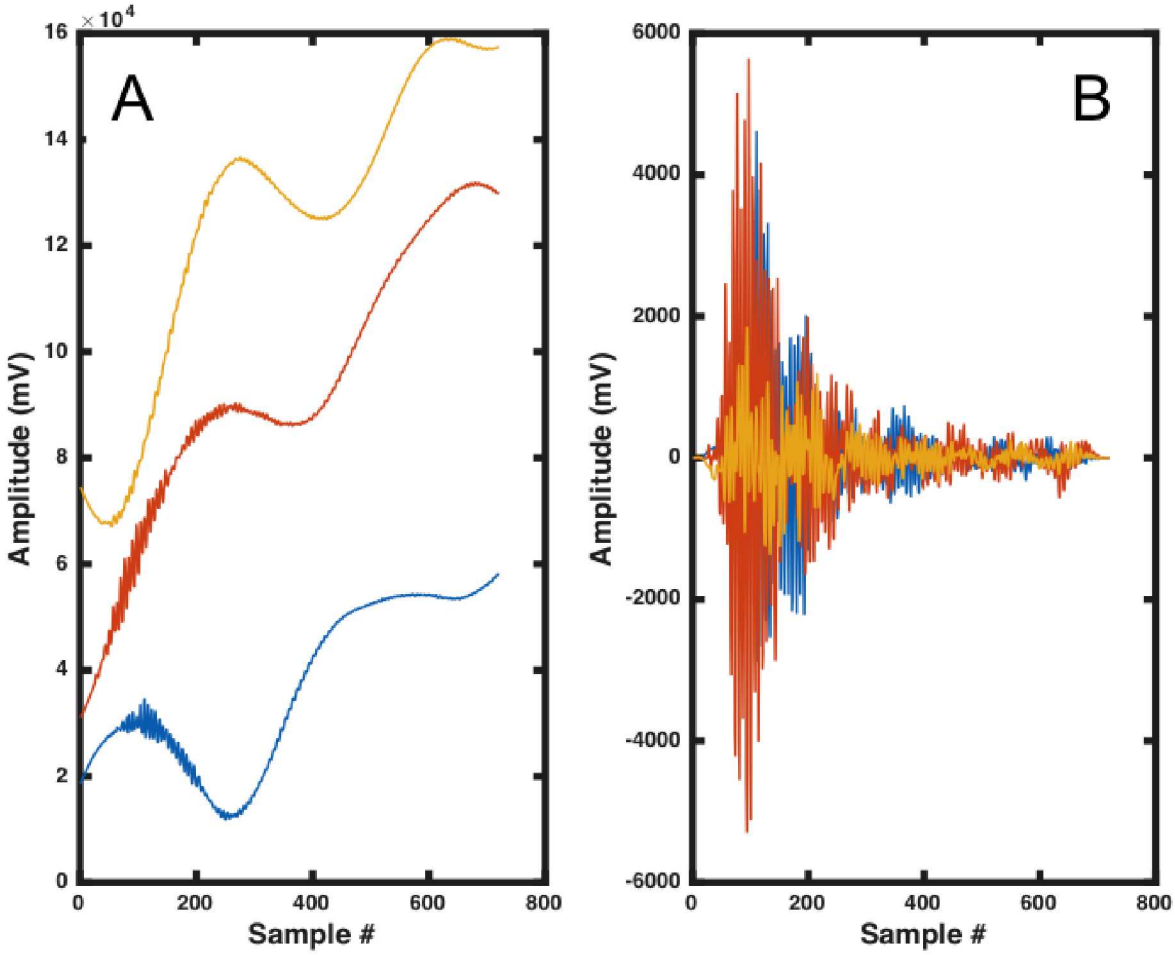

Figure 9.5. Example of high-amplitude wind-induced borehole noise : panel (A) shows three raw CASSM traces contaminated by wind noise while panel (B) shows the result after careful application of pad, taper, and bandpass filter.

cessing steps included : (1) data conversion and date assignment for the sequential SEG-2 field records, (2) assignment of CASSM source numbers to field gathers using information from auxilliary data channels, (3) temporal sorting of all gathers into timelapse "epochs" including a full source suite, (4) addition of wireline geometry for all traces, (5) conversion of wireline geometry into true geometry using deviation logs, (6) application of wind suppression filter and bandpass, and (7) sorting the full dataset into temporal gathers for traveltime analysis.

The characteristics of the baseline CASSM datasets were relatively uniform with an example gathers shown in Figure 9.6. The upper levels on the 48 level hydrophone array, positioned in the overburden, had very low S/N suggesting some degree of partial saturation or low Q weathered material. P-waves arrivals, while pickable, were relatively low in amplitude; strong S-wave arrivals and even tentatively identified converted modes (P-to-S) were also visible. Figure 9.6 panel A shows a raw CASSM gather with color highlighting showing the response of the 24 and 48 channel array sections in the north and east wells respectively. Panel B, Figure 9.6 shows an example gather with preliminary picks for direct P, direct S, and P-S converted arrivals. Note the high amplitude coda which could either be caused by strong S scattering or coherent reflections which were spatially aliased at the 1/2 m receiver spacing.

Source Characteristics and Repeatability

The piezo-ceramic sources used in the ML-CASSM survey exhibited good bandwidth and repeatability during the experiment. The 4" sources utilized have several resonant modes and typically exhibit peak frequencies in the 4-5 kHz range. Due to the high initial Q and short offsets of the Blue Canyon Dome test site, frequency peaks up to 9 kHz were observed in the pre-fracture surveys (see Figure 9.7C) with reasonable signals down to 800 Hz on the lower end of the spectrum. Significant changes in signal spectrum were observed before and after the fracturing events; Figure 9.7 panel A shows a single source/receiver pair before and after the first fracture event. As can be seen, raw amplitudes were considerably lower after fracturing, suggesting significant changes in Q, with several higher frequency source peaks absent in the repeat survey.n the repeat survey. While large changes in spectral characteristics are visible, the changes in P-wave first arrival times were smaller in magnitude (Figure 9.7b).

During periods which did not span significant subsurface alterations (e.g. fracture induction, water injections etc), the CASSM sources exhibited excellent repeatability. Figure 9.8 provides several examples of source fidelity over a $\sim$25 minute period. Figure 9.8A depicts 18 epochs of data for the same source/receiver pair without gain equalization; as can be seen, the source waveform, including later arrivals, are highly repeatable. Phase stability in the source was good with a quantitative NRMS in the P-wave window of better than 5%. Comparisons revealed that NRMS limits were due to largely to incomplete removal of wind noise, visible as small background amplitude trends. Panels B and C of Figure 9.8 show all 18 epochs superimposed. Panel C shows a detailed view repeatability in the P-wave window.

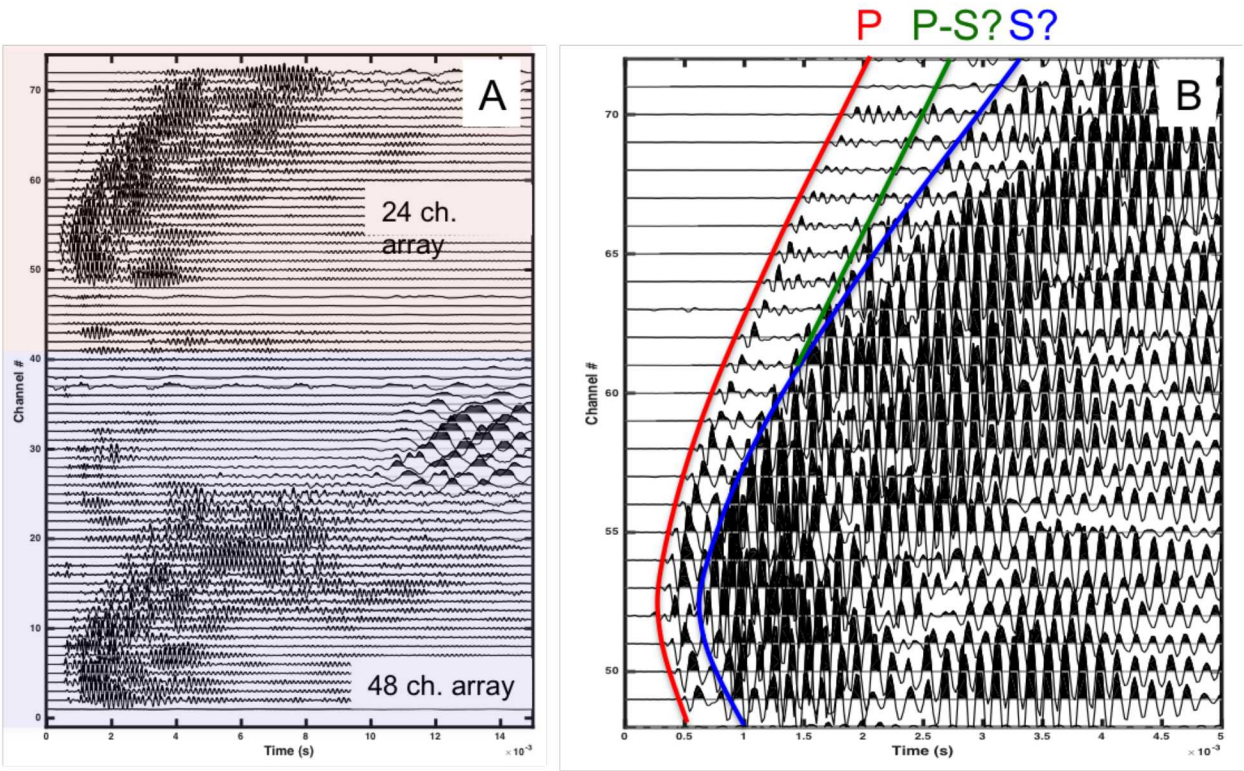

Figure 9.6. Raw CASSM data including a full field record (panel A) and a single segmented gather (panel B) showing tentative picks of direct wave mode (P,S, P-to-S).

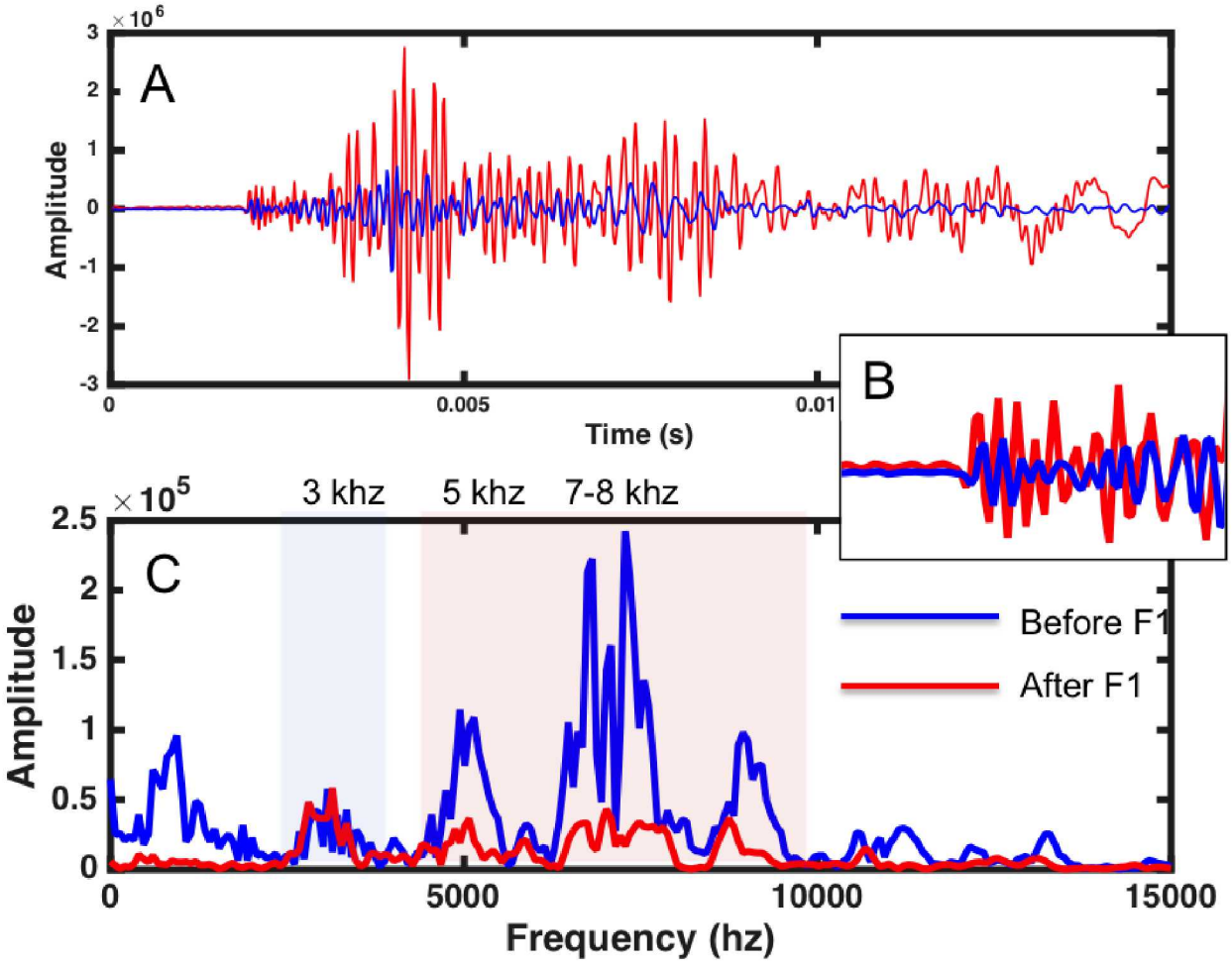

Figure 9.7. Example of changes in a single crosswell trace before and after fracturing: panel (A) shows time domain traces while inset (B) shows the first arrival window. Panel (C) shows the difference in source spectrum.

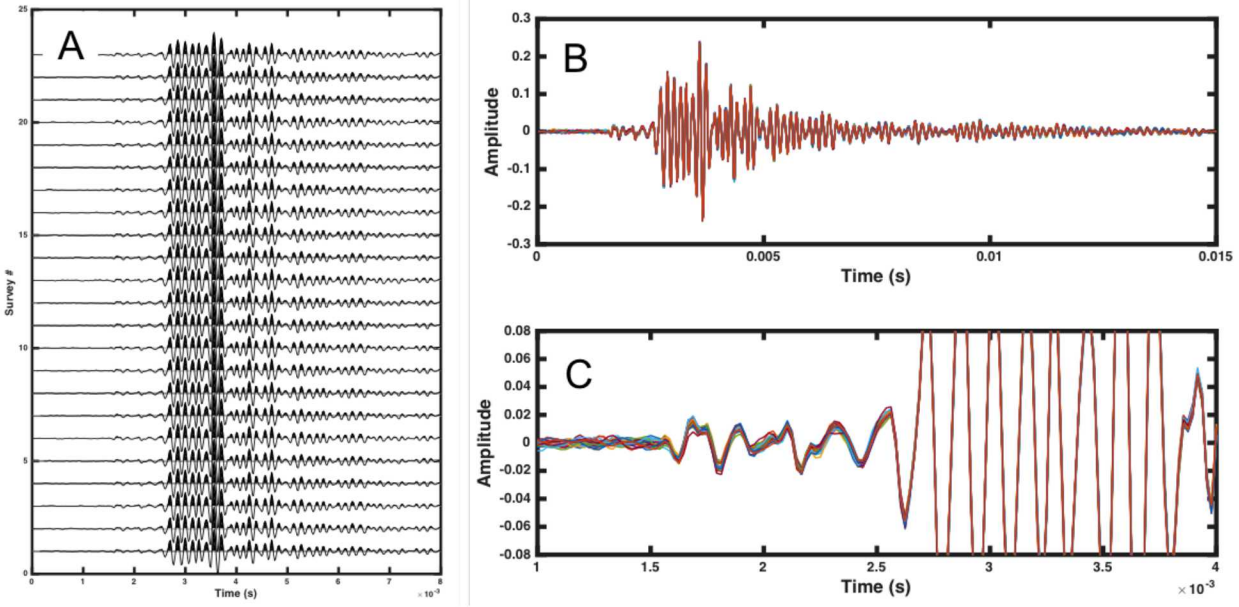

Figure 9.8. CASSM source repeatability : Panel (A) shows a wiggle comparison of 25 minutes of CASSM acquisition for the same source/receiver pair while panels (B) and (C) show the same traces superimposed to accenuate differences. Panel (C) is a zoom of the P-wave first arrival.

Second Injection Test : Stress Observations?

While the full ML-CASSM dataset acquired at Blue Canyon is only in the initial phases of processing, early analysis indicates that the seismic measurements during the sequence of water and ZVI injections yielded significant responses. Initial exploratory data analysis has focused on the water injection test performed after the second fracture emplacement on the afternoon of 4/18/2016. In this portion of the experiment, after an initial high volume push, water was injected at a constant rate of ∼1.3 gallons/minute until a pressure of ∼43 psi was reached, followed by measurement of pressure decay. If flow in this scenario is dominated by fracture transmission, a seismic signature should be visible as effective stress on the fracture plane is decreased. Given the relatively shallow depths monitored (12.9-22.9 m), the effective stress on the fracture plane should be reduced from ∼70 psi to ∼20 psi over the course of the injection, with a corresponding reduction in effective fracture stiffness as well as an increase in fracture impedance. After the initial processing described previously, a crosswell data subset corresponding to the E/W well pair (2/4) was selected for preliminary analysis. The data during the pumptest was divided into 174 timelapse epochs with a temporal resolution of ∼1 minute for each 10x48 (S/R) tomographic dataset. This data subset corresponds to the entire pumptest with the addition of 15 minutes of pre-injection data and 30 minutes after pressure had decayed to near 0 psi.

Qualitative examination found significant changes in waveform over the course of the fluid injection, including the appearance of pressure-dependent variations in the coda, small variations in P-wave first arrival, and reductions in apparent Q. Figure 9.9 shows typical responses for oblique high angle rays as a function of time. Panels (A) and (B) show a single trace as a function of time during the pump test at two gain levels to better appreciate signal response. As can be seen, a sudden change in coda is visible temporally correlated with the initiation of the pump test (time history shown in Figure 9.9). A later arrival, with variable arrival time, appears to be correlated with pressure magnitude and is visible in panel (A) at times near 3 ms; this arrival could be a coherent reflection or scattered event sensitive to fracture aperture. Amplitude of the coda appears sensitive to pressure as well with changes in apparent amplitude visible in panel (B).

While changes in coda response and scattered arrivals show the greatest apparent sensitivity, the direct P-wave arrival also appears to have measurable variations during injection. The challenge of such analysis is lack of prior knowledge of fracture orientation with respect to ray path; this complicates any preliminary interpretation until finalized fracture images are derived from other components of the dataset. Figure 9.10 panel (A) shows an example temporal gather for a S/R pair near zero offset in the upper section of the 4/2 well pair. As can be seen, the P-wave first arrival is delayed by increased pressure during the pump test. The delay time is not, however, proportional to applied stress and appears to be a binary opening/closing response.

A more detailed visualization of the coda variations discussed previously yields several secondary observations. While the later arrivals do appear to show a stress-dependent response during injection, they do not show the same response path during pressure decay

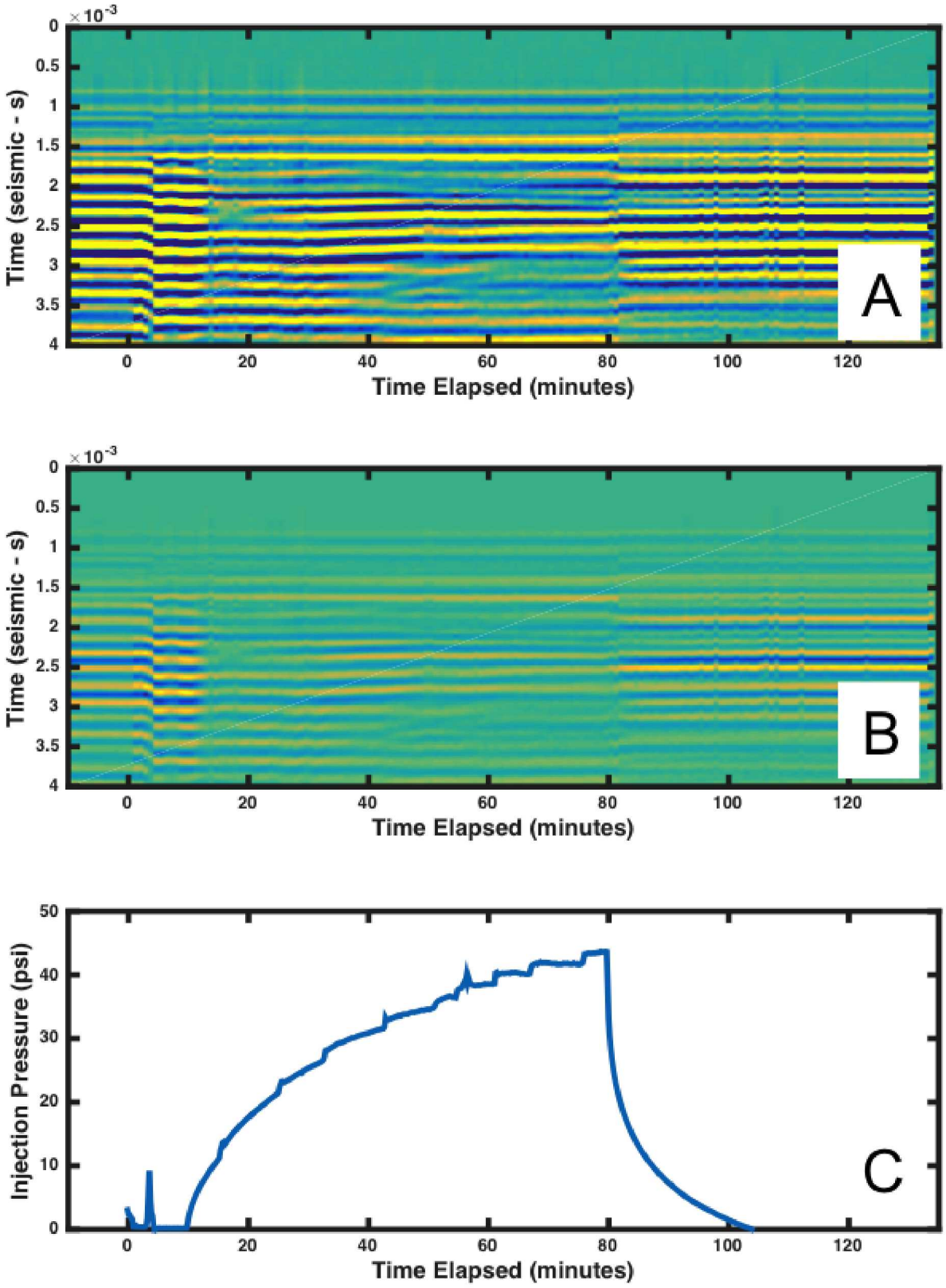

Figure 9.9. Representative CASSM response during second pump test : Panels (A) and (B) correspond to the evolution of the same oblique source/receiver pair over time

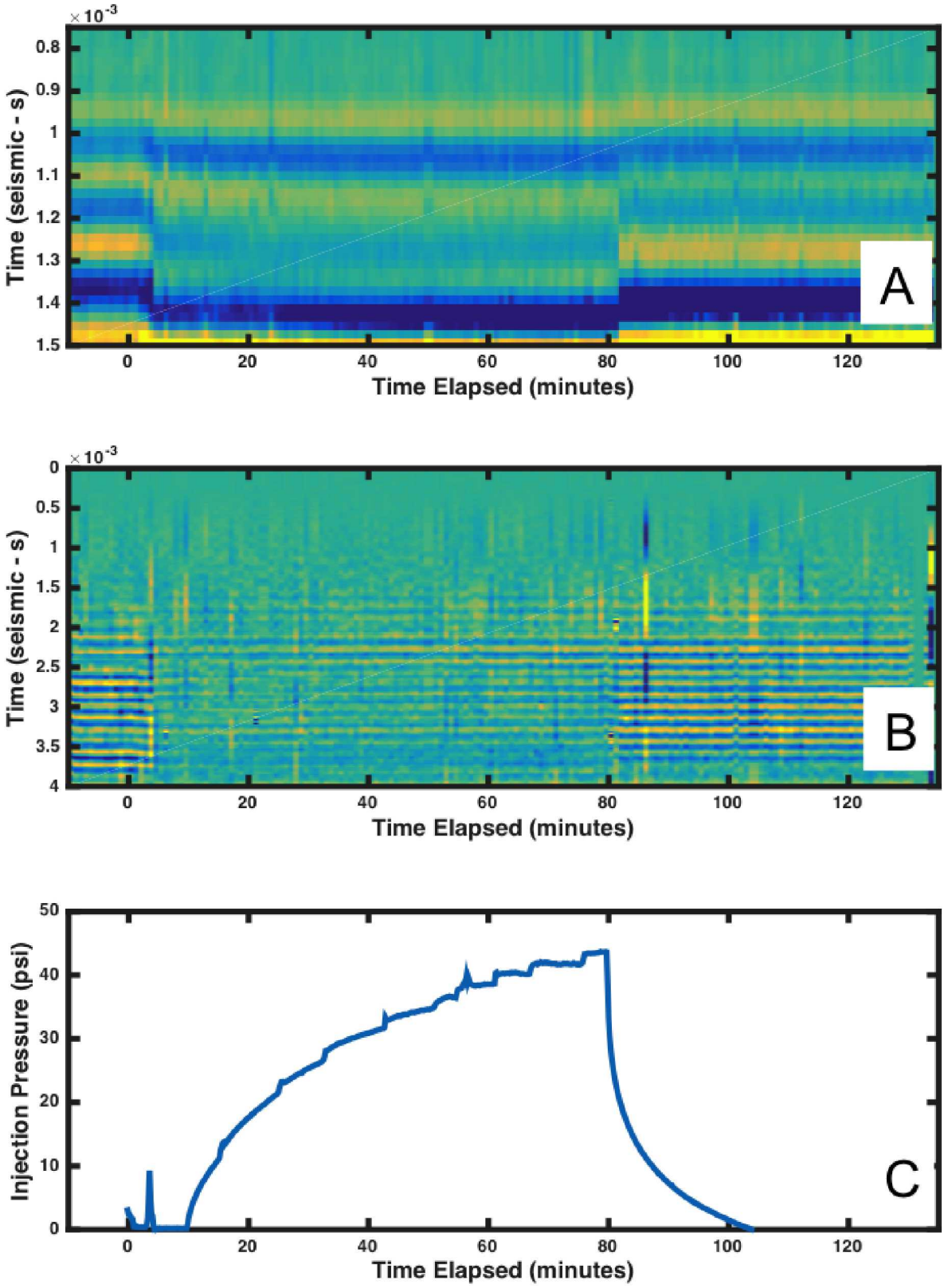

Figure 9.10. An example of first arrival effects during injection (A) as well as Q response (B) during the injection history shown in panel (C).

(9.11). Likewise, as can be seen in both Figures 9.9 and 9.11, the coda sequence does not return to the starting state after conclusion of the injection, suggesting a secondary alteration beyond elastic changes in fracture aperture.

ML-CASSM Effort : Conclusions and Next Steps

While the ML-CASSM analysis is still in preliminary stages, several observations can be made. The ML-CASSM system constructed for the experiment, the largest to date with 22 sources, proved quite flexible and was quickly deployed at the site with minimal operational challenges. During the 1.5 weeks in the field, a vast dataset consisting of over 55,000 gathers and 2000 vintages of crosswell data were acquired. Like prior ML-CASSM experiments, the source arrays exhibited excellent repeatability (<5% NRMS) and wide bandwidth (800 Hz to 9 kHz) with the main challenge remaining signal contamination from wind noise. A response from fracturing was observed although tomographic analysis is still pending. Likewise, a seismic response was visible during the 2nd pump test conducted, suggesting that our goal of developing models for stress-dependent permeability of fractured systems is within reach.

However, much work remains to be done to fully understand the observations made at the Blue Canyon Dome fracture pilot. Large sections of the dataset remain unexamined, including the first pump test and both ZVI injections. The responses during the second pump test were complex, particularly waveform changes deep within the coda, and will require significantly more analysis to quantify the discrete arrivals detected. The lack of symmetric pressure responses suggest that non-elastic perturbations occurred to the fractures during pressure perturbation. More generally, we have yet to apply the advances in automatic picking described elsewhere in this report to the full ML-CASSM dataset; such tools are essential to fully processing datasets with fine temporal sampling and the development of effective real-time geophysical monitoring systems.

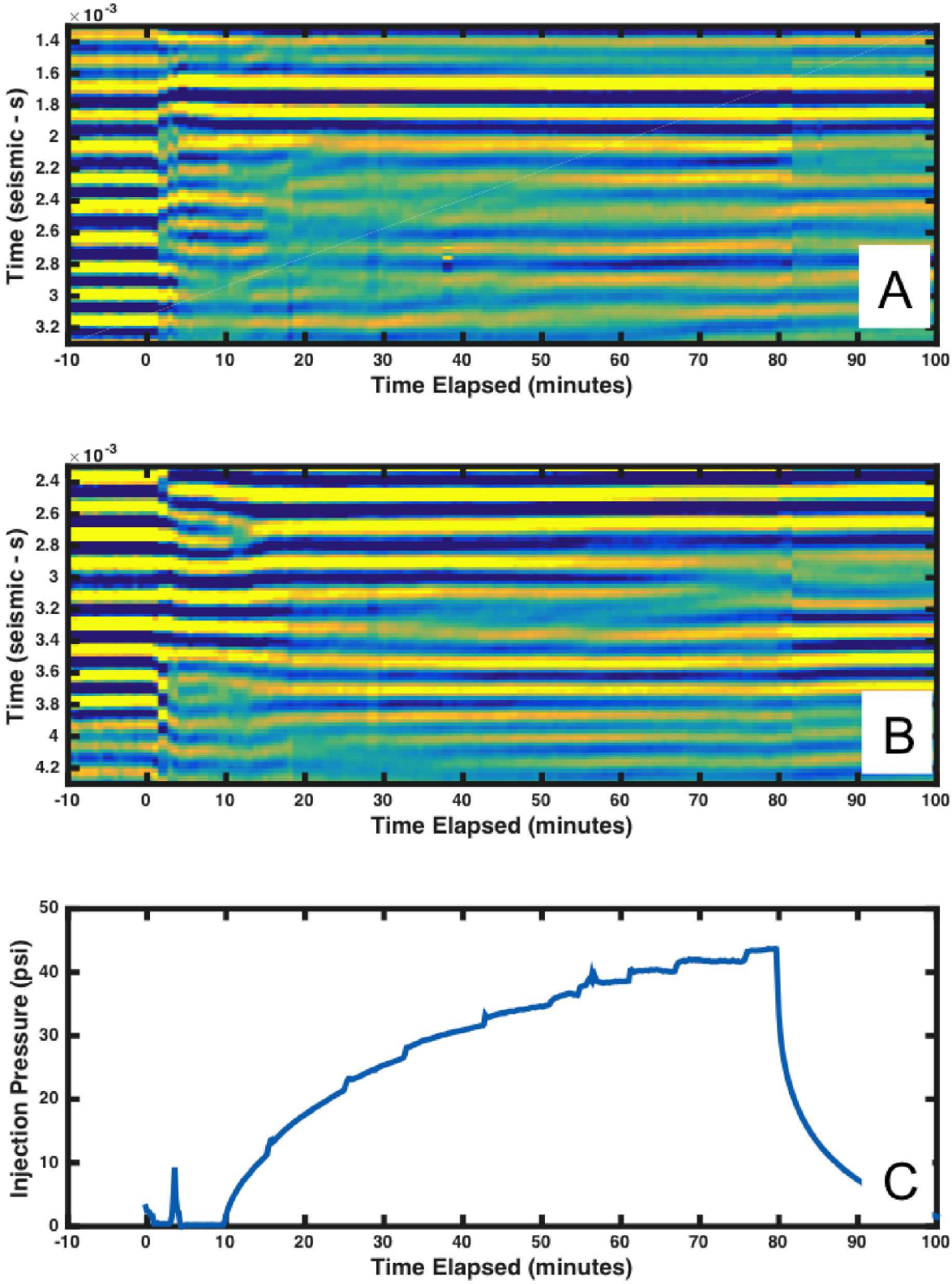

Figure 9.11. A detailed view of the temporal response for two 45° S/R pairs at the top (A) and bottom (B) of the 4/2 well pair in comparison to injection pressure.

Chapter 10

Distributed Acoustic Sensing

Distributed sensing using fiber optic cables is an advancing technology that shows potential for improving the efficiency and spatial resolution of geophysical studies (Molenaar et al., 2012; Daley et al., 2013; Parker et al., 2014). To address the New Subsurface Signals (NSS) SubTER pillar, we aimed to test the use of Distributed Acoustic Sensing (DAS) for fracture monitoring and characterization. In particular, ambient seismic noise was recorded in the hope of passively detecting velocity changes resulting from fracture emplacement through the use of seismic interferometry. Heretofore, ambient seismic noise recorded on fiber optic cables has not been used in borehole installations for the purpose of fracture imaging. The novel fiber installation at Blue Canyon Dome provides a unique dataset for examining the ambient noise wavefield as recorded by DAS within boreholes and exploring its potential use for fracture imaging studies.

Methods

It has been well established that group and phase velocities can be found using the cross correlation of ambient seismic noise records from two seismic stations to recover the impulse response, or empirical Greens Function, for surface waves traveling between those stations (Campillo and Paul, 2003; Shapiro and Campillo, 2004; Lin et al., 2008). Velocity changes of the subsurface have been shown to result in time-shifts in scattered coda waves within cross correlations of ambient seismic noise (Sens-Schönfelder and Wegler, 2006; Hadziioannou et al., 2009). The emplacement of fractures at Blue Canyon Dome is expected to reduce the bulk seismic velocity, with surface waves traveling perpendicular to fractures experiencing the strongest velocity reduction. Therefore, comparison of the scattered arrivals within cross-correlations of ambient seismic noise recorded on the fiber optic cables before and after fracture emplacement should show a relative velocity decrease. Furthermore, variations between channel pairs may be useful in fracture characterization.

A continuous length of fiber optic cable was installed in the monitoring boreholes to test the viability of DAS for detecting seismic velocity changes resulting from fracture emplacement. The permanent fiber installation allowed for collection of both passive and active seismic data throughout the study (Figure A.1 in Appendix A). Passive seismic interferometry using ambient noise required the most development and is the focus of this chapter.

Twelve to thirteen hours of ambient noise were recorded before and after both explosive stimulations providing distinct time periods for comparison. These recordings took place over night (approximately 6:30 PM to 7:30 AM) during which time site activities were a minimum. Acoustic data were recorded at a sampling rate of 10 kHz. Ambient noise sources were expected to be environmental and anthropogenic noise. The contracted company, Silixa, de-noised the raw DAS data and converted the format to HDF5. The de-noising procedure resulted in channels located approximately every 1 meter along the continuous length of fiber optic cable. We used distance measurements, provided by Silixa, to determine the channel depths and locations corresponding to each borehole and created 30-second long miniseed files for each channel located below ground surface.

The Python package MSNoise was used to create 1-minute cross correlations for the first 3 hours of each night recording time period. Moving 60- and 120-minute stacks were created for each time period (preshot1, postshot1, preshot2, postshot2). The MSNoise source codes required heavy alteration to work with such small timescales not normally encountered in seismic interferometry studies. The MSNoise procedure was then adjusted to calculate velocity changes (δv/v) in the moving stacks for each discrete time period relative to the complete preshot1 3-hour stack. Lastly, the δv/v values from all moving stacks were averaged for each time period and channel pair. To reduce computation time the channels were downsampled by a factor of 3 and only channels within the competent rhyolite formation, below 35 ft depth, were analyzed.

Preliminary Results

The average relative velocity change was calculated for each analyzed channel pair and night recording period. For all channel pairs the preshot1 moving stacks resulted in δv/v values near zero (-2 % $<\delta$v/v $>$2 %), which was to be expected. The ambient noise recordings following the first explosive stimulation (postshot1) showed a relative velocity decrease for 93 % of all analyzed channel pairs with an average δv/v of -7 %. Eigthy-four percent of channel pairs showed a large velocity decrease ($<$-2 %). Fourteen percent of all analyzed channel pairs had no significant velocity change (-2 % $<\delta$v/v $>$2 %) and 2 % of channel pairs showed a large velocity increase ($>$2 %) (Figure 10.1). Following the second explosive stimulation (postshot2) a larger percentage of channel pairs showed a relative velocity increase compared to the postshot1 results. Sixteen percent of channel pairs showed a large velocity increase ($>$2 %). Fifty-eight percent of channel pairs showed a large velocity decrease ($<$-2 %). Twenty-six percent of all analyzed channel pairs had no significant velocity change relative to preshot1 conditions (-2 % $<\delta$v/v $>$2 %) (Figure 10.1). There are multiple potential explanations for the greater proportion of channel pairs showing a relative velocity increase during the preshot2 and postshot2 time periods. First, water injections and pressure tests are likely to have an effect on the seismic velocity. Second, a greater scattering medium is likely to decrease the signal-to-noise ratio and alter travel paths between channels. Therefore the wavefield may be too altered between preshot1 and postshot2 for coherent and meaningful comparison of scattered phases. Lastly, some fracture healing may have occurred.

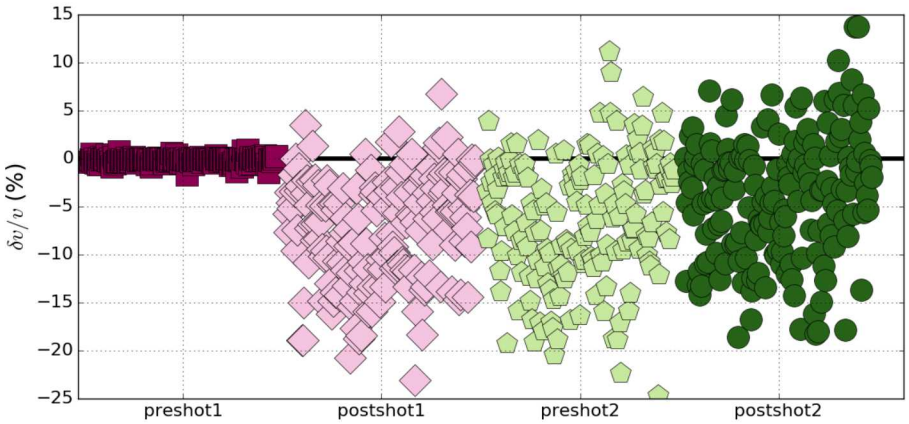

Figure 10.1. Average percent velocity changes (δv/v) from 120-minute moving stacks relative to the complete preshot1 3-hour stack for each channel pair and time period.

The percent relative velocity change following the two explosive shots (δv/v %) was compared to the percent P-wave velocity change obtained from cross-well tomography (Figure 10.2). The absolute magnitude of velocity was not directly compared since the two results are from different seismic waves and techniques, however, the sign and relative magnitude was found to be in good agreement. Channel pairs with the largest decrease in δv/v occur across zones of the largest decrease in P-wave velocity in the 3D tomography. Channel pairs that occur closer to positive velocity change zones in the tomography had a smaller decrease or even an increase in δv/v. Larger scale trends in both sets of results suggest the presence of a near-vertical fracture oriented north-east to south-west. The DAS results show that channel pairs below 16 m depth and between the West and South boreholes show the strongest reduction in velocity. We interpret this to be a direct indication of the fracture location, supported by the cross-well tomography.

Some initial steps were taken to characterize the ambient noise wavefield as recorded by the DAS technique. Figure 10.3 shows the power of different frequencies within the raw ambient seismic noise for each analyzed channel. The channels are sorted based on their borehole (rows) and depth (colors). The four columns in Figure 10.3 represent the different time periods analyzed. For all boreholes there is a broadband decrease in power following the first shot. This is to be expected with the addition of scattering fractures. Frequencies above 1000 Hz shows a very flat power response that has no significant depth relationship. Conversely, frequencies below 1000 Hz show stronger power for shallower channels and this trend appears more prominently following the first shot. The West and South boreholes show this trend the strongest. These observations suggest a possible link to the presence of fractures. Overall, the trend of higher power for lower frequencies at shallower channels is not currently understood and further spectral analysis is needed.

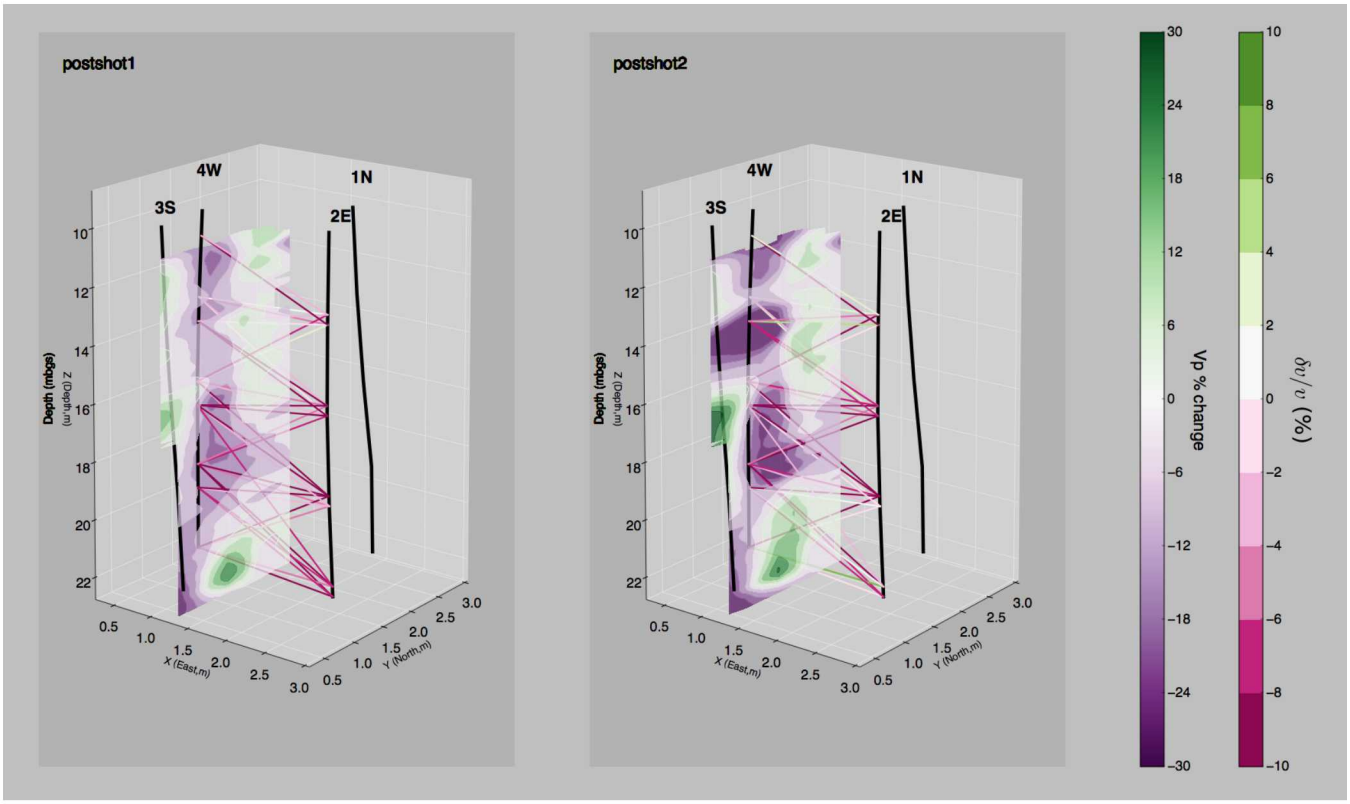

Figure 10.2. Percent relative velocity change for channel pairs between the West and East boreholes is compared to a North-West slice through the percent relative P-wave velocity change from cross-well tomography results. Note that the δv/v lines serve to connect the two channels for each channel pair and do not represent the absolute travel path since the ambient noise technique uses the scattered arrivals and no formal ray-tracing was done.

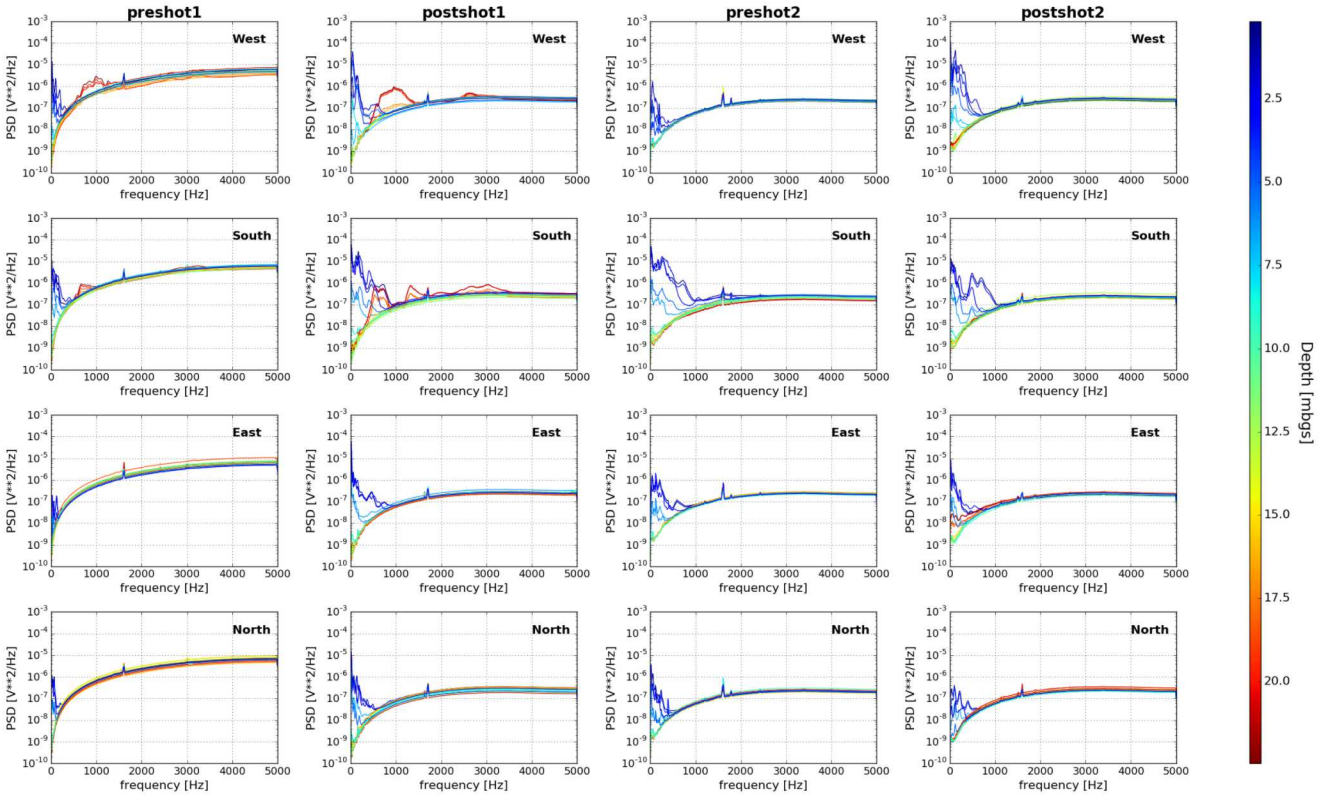

Figure 10.3. Power spectral density (PSD) for the raw ambient noise recorded using the DAS technique. PSD subplots are organized by borehole and night recording time period. The channels are then colored based on the their depths to identify possible trends.

Future Work

These preliminary results suggest the passive technique of seismic interferometry using ambient seismic noise recorded on fiber optic cables is a promising new option for detecting fracture generation and fracture imaging. However, the stability of the ambient seismic noise wavefield needs further investigation. Due to time constraints and computing limitations, current results were obtained using only 3 hours of ambient noise data from each of the 4 night recordings. Higher quality measurements are expected when longer time periods are stacked. We plan to cross-correlate the remaining 9 hours of ambient noise data from each time period to create larger stacks. We will investigate the relationship between signal-to-noise ratio and length of time stacked so as to inform future studies. In addition, further spectral analysis needs to be done along with beamforming to characterize the ambient noise sources during each time period. Furthermore, the moving stacks from preshot2 and postshot2 will be compare to the postshot1 full stack (instead of preshot1) to attempt to improve the δv/v results.

Water injections and active source seismic campaigns were also recorded on the fiber optic cables, but those data have not yet been analyzed. Molenaar et al. (2012) showed that changes in acoustic-energy levels across high frequency DAS measurements correlated with injection rates during hydraulic fracturing. This response was only seen in channels closest to the perforation locations and was absent elsewhere. A similar relationship may exist in the fiber data recorded during water and pressure injections at Blue Canyon Dome. Therefore, we plan to analyze the DAS data recorded during injections to explore relationships with injection rates and potentially identify fracture locations through variations in channel responses. Comparison of active source seismic arrivals between the fiber and hydrophone arrays is also needed to further assess the DAS recording quality.

Chapter 11

Real-Time Electrical Resistivity Tomography

Overview

Current flow within electrically resistive fractured rocks systems is dominated by fracture flow when the fractures are fluid filled. Because the electrically conductive features of the system are the fractures themselves, the fractures, or flow within the fractures may be imaged using electrical geophysical methods. These methods use temporary or permanently installed electrodes to inject current into the subsurface, and to measure the resulting potentials induced by the current injection. There are no moving parts required downhole, and no instrumentation required in the borehole, making the systems robust for long term monitoring in fractured rock systems. At the Blue Canyon Site, electrodes were permanently grouted within the borehole annulus, leaving the borehole accessible for seismic monitoring and ground penetrating radar instrumentation. In this section we review system installation, baseline 3D imaging before fracture stimulation, and real-time 4D post-stimulation imaging of fluid flow within the stimulated fracture zone. The imaging results illuminate the stimulated fracture dimensions by imaging the fluid within the fracture, and demonstrate the feasibility of real-time imaging as a feedback mechanism enabling control of subsurface processes during fracture stimulation and subsequent operations.

System Installation

Stainless steel electrodes were installed at 0.5 m intervals on the outside of the PVC casing in each of the four instrumented monitoring wells surrounding the stimulated well. Each electrode was attach to a wire that extended through the annulus to the surface and the ERT survey instrumentation. The electrodes were then grouted in place using a high-strength grout specially formulated to improve imaging resolution by reducing vertical current flow within the annulus, as described in the next section. Figure 11.1 A shows and casing string instrumented with electrodes being lowered into the borehole prior to grouting. Figure 11.1 B shows a close-up view of a single electrode and wire termination. Sixteen electrodes were installed on each well, for a total of 64 electrodes covering a vertical imaging zone of

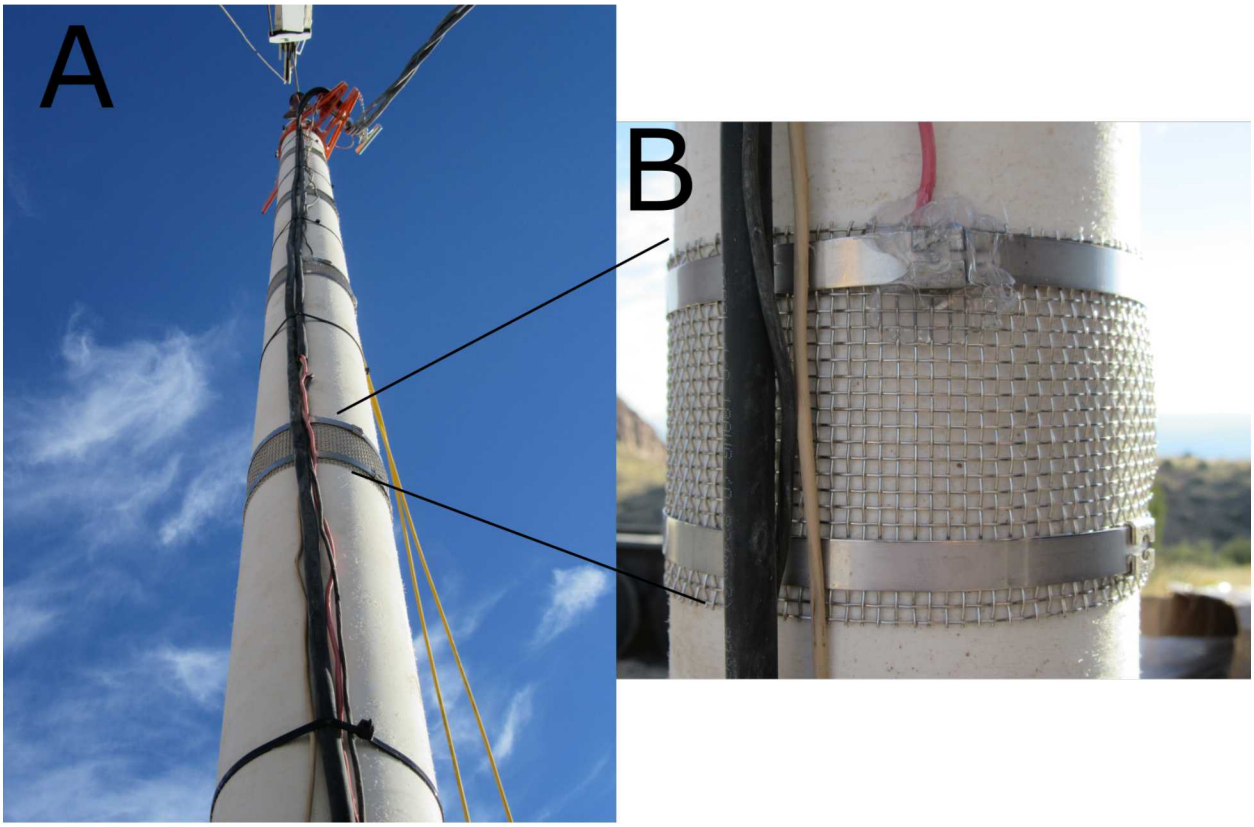

Figure 11.1. A) Photograph of PVC casing string instrumented with electrodes and distributed acoustic sensing fiber optic cables being lowered into a monitoring borehole. B) close up photograph of electrode and conductor termination for an electrode installed in the annular space.

approximately 8 meters surrounding the stimulated well.

Annular Grout Development

Laboratory scale measurements of cores collected from the monitoring boreholes had bulk electrical conductivities as low as 5e-5 S/m. Typical grouting materials (e.g. Portland cement and fine sand) have conductivities ranging from 0.03 to 0.05 S/m, several orders of magnitude larger than the host rock. Noting that the grouting materials encase the electrodes within the annulus, the high conductivity of the grout relative to the host rock would cause current channeling within the annulus, thereby reducing the capability to sense host rock conductivity away from the borehole, resulting in a loss of imaging resolution. To reduce current channeling within the borehole, efforts were undertaken to formulate a low conductivity grout material. A comprehensive literature provided guidance, and suggested

that materials used in high-strength, low permeability cement mixtures also provided low porosity and low electrical conductivity. Based on this information several cement samples were prepared and monitored for conductivity during the 28 day curing period. At the end of this period, the grout with the lowest conductivity was chosen to be used at the field. The grout consisted of a mixture of approximately 15 percent Type A Portland Cement and 85 percent nickel fly ash, yielding a conductivity of approximately 0.001 S/m. Although the conductivity of the engineered grout was over one order of magnitude less than that of standard grouting materials, it was still several orders of magnitude larger than the rhyolite host rock, resulting is significant current channeling, as revealed by simulations of current flow discussed in the next section. Under these conditions, imaging resolution was maintained to the extent possible using advanced modeling techniques within the inversion algorithm. In particular, the boreholes and grout annulus were modeled in true dimension, including borehole deviations, 2) the grout conductivity within the annulus was provided to the inversion algorithm, and 3) the electrodes were modeled in true dimension, rather than as point sources (Johnson et al., 2015). As shown in the pretest model, neglecting the effects of the borehole grout and the finite electrode dimensions would have decreased the accuracy of the forward modeling and reduced imaging resolution.

Pre-Test Modeling

Extensive pre-test ERT modeling was conducted to assess expected imaging performance and optimizing data collection schedules specific to field conditions. Using the parallel E4D code (Johnson et al. (2010); https://e4d.pnnl.gov), all aspects of the system were modeled in true dimension to assess the effects of grout conductivity, borehole deviation, electrode dimension, and borehole fluid conductivity within the stimulation well. Figure 11.2 shows a simulation of the subsurface 3D potential distribution generated from a cross well current injection given field conditions specific to the sight. The potential field is represented by 3D iso-surfaces according to the given color scale. Noting that current flows perpendicular to the potential iso-surfaces, the impact of current flow through the relatively conductive grout is immediately evident by the vertical stretching of the potential distribution along each borehole. Failure to account for this phenomena within the imaging algorithm would likely produce significant imaging artifacts and reduce the overall utility of the baseline and time-lapse ERT imaging. By modeling the annular grout in true dimension, and specifying the grout conductivity, the imaging algorithm was informed of this feature, and able to focus solely on estimating the conductivity of the host rock (as opposed to ignoring or estimating the grout conductivity).

Pre-test imaging and post-stimulation time-lapse imaging of tracer flow was conducted with a string of vertical electrodes deployed in the stimulation borehole. During pre-test imaging, the stimulation hole was filled with hydrant water. During time-lapse imaging, the stimulation hole was filled with zero-valent iron tracer, which had a conductivity approximately two orders of magnitude larger than the hydrant water. In order to investigate the influence of the changing borehole fluid conductivity between the baseline and time-lapse

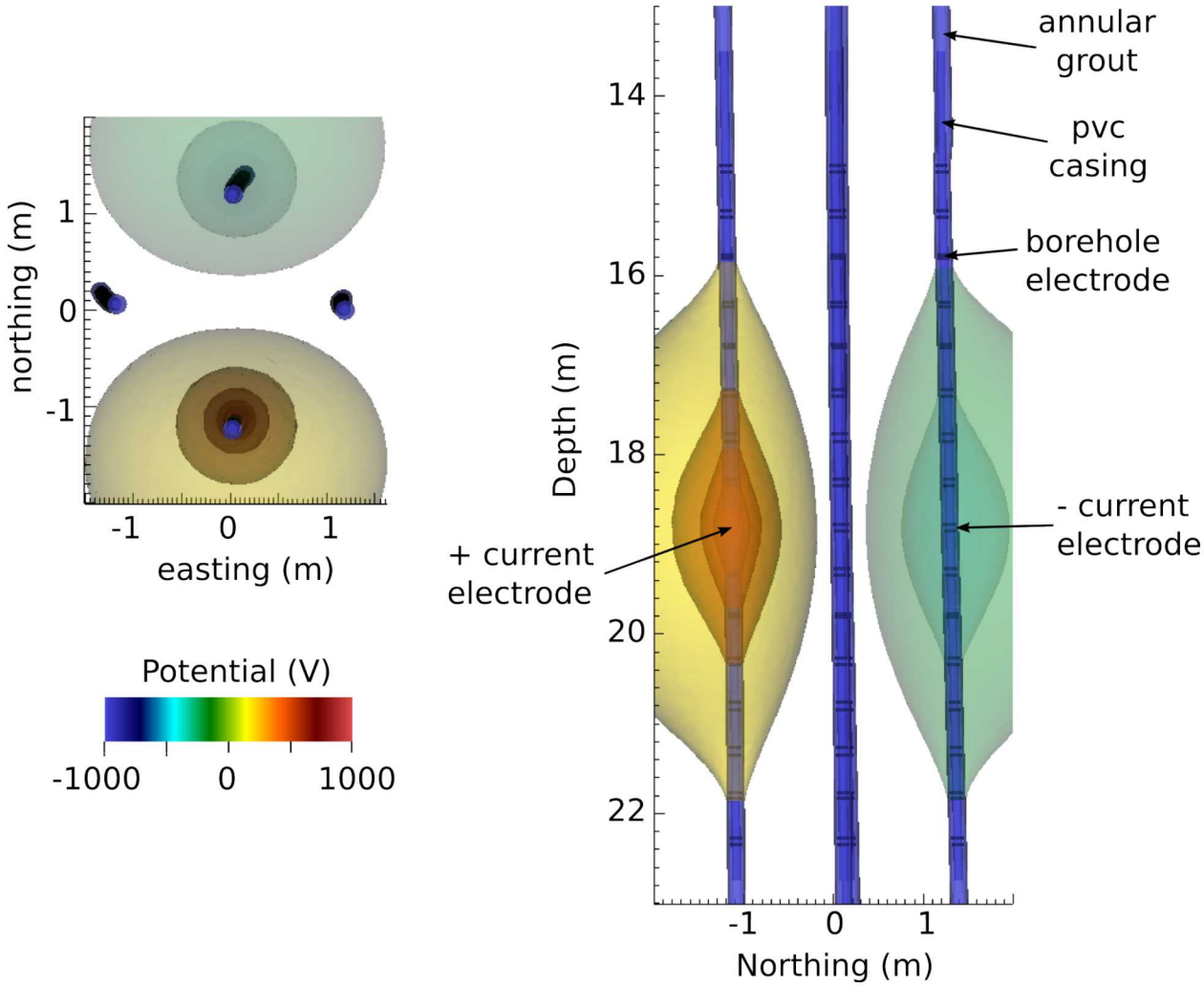

Figure 11.2. (left) Plan view and (right) cross-section view of a simulated potential distribution demonstrating the influence of the electrically conductive grout relative to the host rock. This effect is accounted for in the forward modeling portion of the inversion algorithm

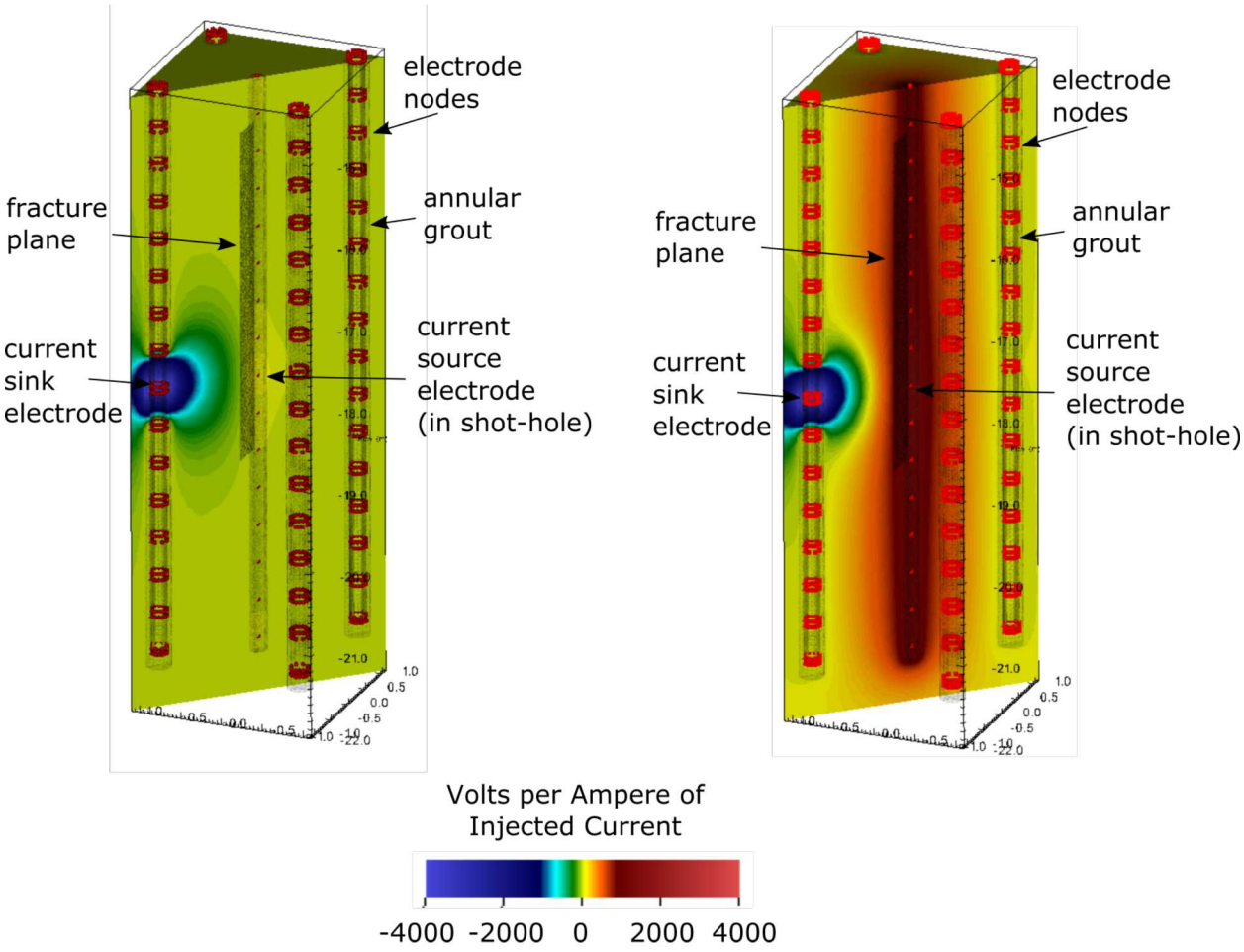

Figure 11.3. Simulated potential distribution with hydrant water (left) and zero-valent iron (right) tracer occupying the stimulated borehole. The effects of borehole conductivity were explicitly accounted for during the forward modeling portion of the inversion algorithm.

tests, we simulated voltage distributions for each scenario. An example simulation is shown in Figure 11.3. Here the current sink electrode is within the annulus of a monitoring well and the current source electrode is within the fluid filled stimulation hole. The simulation shows that when the stimulation hole is filled with tracer, the entire borehole essentially acts as a long linear electrode. Failure to account for this phenomena in the inversion algorithm would significantly denigrate imaging results. As with the annular grout, we inform the inversion of this condition by modeling the borehole in true dimension and specify the electrical conductivity of the borehole fluid during the inversion computations. These options are made possible using the unstructured mesh capabilities, high performance computing, and advanced constraint options available in the E4D imaging software.

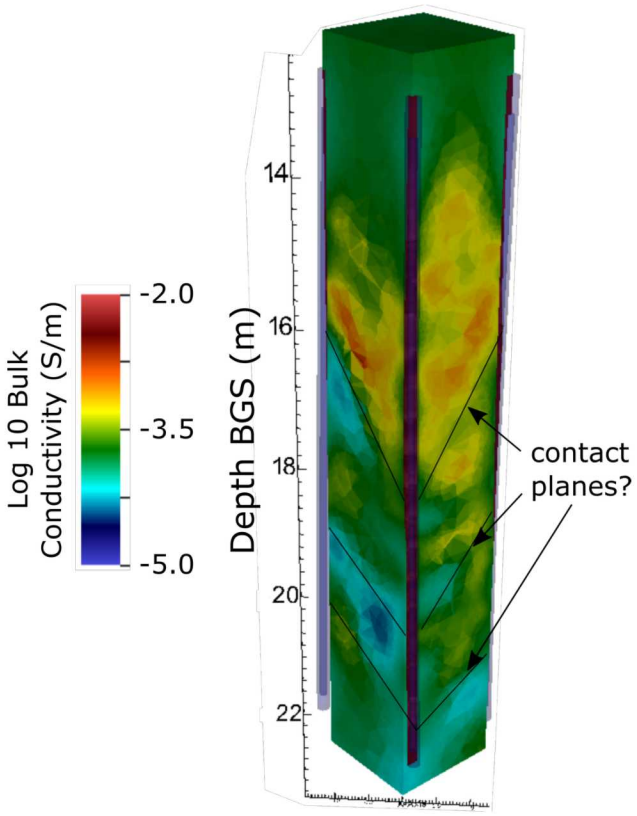

Figure 11.4. South to north facing view of 3D pre-stimulation baseline ERT image.

Baseline Pre-Stimulation Imaging

A comprehensive baseline ERT data set was collected prior to stimulation operations. The resulting image is shown in Figure 11.4. Conductivity values vary over three orders of magnitude from approximately 0.02 S/m in the upper section of the imaging zone, to 0.00005 S/m at the bottom of the imaging zone. The images reveals steeply dipping structures striking generally west to east, with a dominant and persistent contact range from 16-18 meters below ground surface. This feature is also evident in the ground penetrating radar and high resolution seismic images.

In addition to providing insight into the geologic structure of the target zone, the baseline ERT image is a critical component of the time lapse ERT processing flow. It serves as both the starting model and the reference model by which all time-lapse images are constrained. If the time-lapse ERT data do not demand a change in the bulk conductivity distribution from baseline in a particular region of the image, then the time-lapse inversion is constrained to assume the baseline value, indicating no change in that region.

Post-Stimulation Real-Time Imaging of Tracer Transport

A primary goal of the SubTER initiative is to develop and demonstrate methods of imaging the distribution of stimulated fractures, and of imaging fluid flow within stimulated fractures. The capability to determine dominant flow paths within a stimulated fracture system is critical for assessing the efficacy of stimulation and verifying environmental projection. Furthermore, the capability to image fracture flow in real-time places time lapse imaging within the sphere of possible technologies that could provide the feedback mechanism necessary to enable real-time flow control within fractured rock systems. Time-lapse ERT imaging operates by imaging spatial and temporal contrasts in electrical conductivity with respect to some baseline condition. The baseline conductivity is removed from the time-lapse images, revealing only what has changed with time. Conductivity contrasts can be induced in stimulated fracture zones simply by introducing fluid into the fracture. The fracture conductivity contrast can also be enhanced using saline tracers. At the Blue Canyon Dome site we demonstrated real-time 3D time lapse ERT imaging (e.g. 4D imaging) of tracer transport through the fracture zone generated after the first stimulation. Rather than using a saline tracer, we used an engineered mixture of zero-valent iron (ZVI) nano-particles immersed in a reducing solute. The intent of the zero valent iron was to induce a contrast in the capacitive properties of the fracture zone, in addition to a contrast in electrical conductivity. In theory, changes in capacitive properties can be imaged in a manner similar changes in conductivity, using the same electrode array and instrumentation. This method is referred to as Complex Resistivity Tomography (CRT) or Spectral Induced Polarization Tomography (SIP). The reductant solution was intended to keep the ZVI particles from oxidizing during injection, thereby preserving the electrical properties of the injectate. The ZVI tracer was injected at a rate of 1.9 liters/minute (.5 gallons/min), for approximately 330 minutes. During injection, time-lapse ERT surveys were collected on an optimized measurement cycle of approximately 13 minutes per survey. Once each survey was complete, the data were processed for data quality using the on-site data collection laptop, then transferred by wireless internet to an off-site supercomputer for tomographic processing. Inversion results were then transferred back to the on-site computer for visualization. The total time for post collection processing, data transmission, and inversion was approximately 2.5 minutes; 2 minutes for inversion and 30 seconds for data quality pre-processing and transmission. The entire process was automated from data collection through inversion to presentation on the field laptop. Visualization of the time lapse imaging results are shown in Figures 11.5 and 11.6. Each figure shows isosurfaces of the change in conductivity induced induced by the ZVI tracer migration into the fracture zone at the indicated elapsed time. The isosurfaces are at log 10 conductivity values of 0.10 0.15 S/m.

Figure 11.5 and 11.6 show views of the time-lase ERT sequence facing south to north and east to west respectively. Close inspection of each view show the fracture suggest a single dominant fracture extending generally in a north south direction. Figure 11.5 is oriented facing parallel to the dominant fracture and 11.6 is facing approximately normal to the fracture. This is consistent with post-stimulation acoustic televiewer logging results,

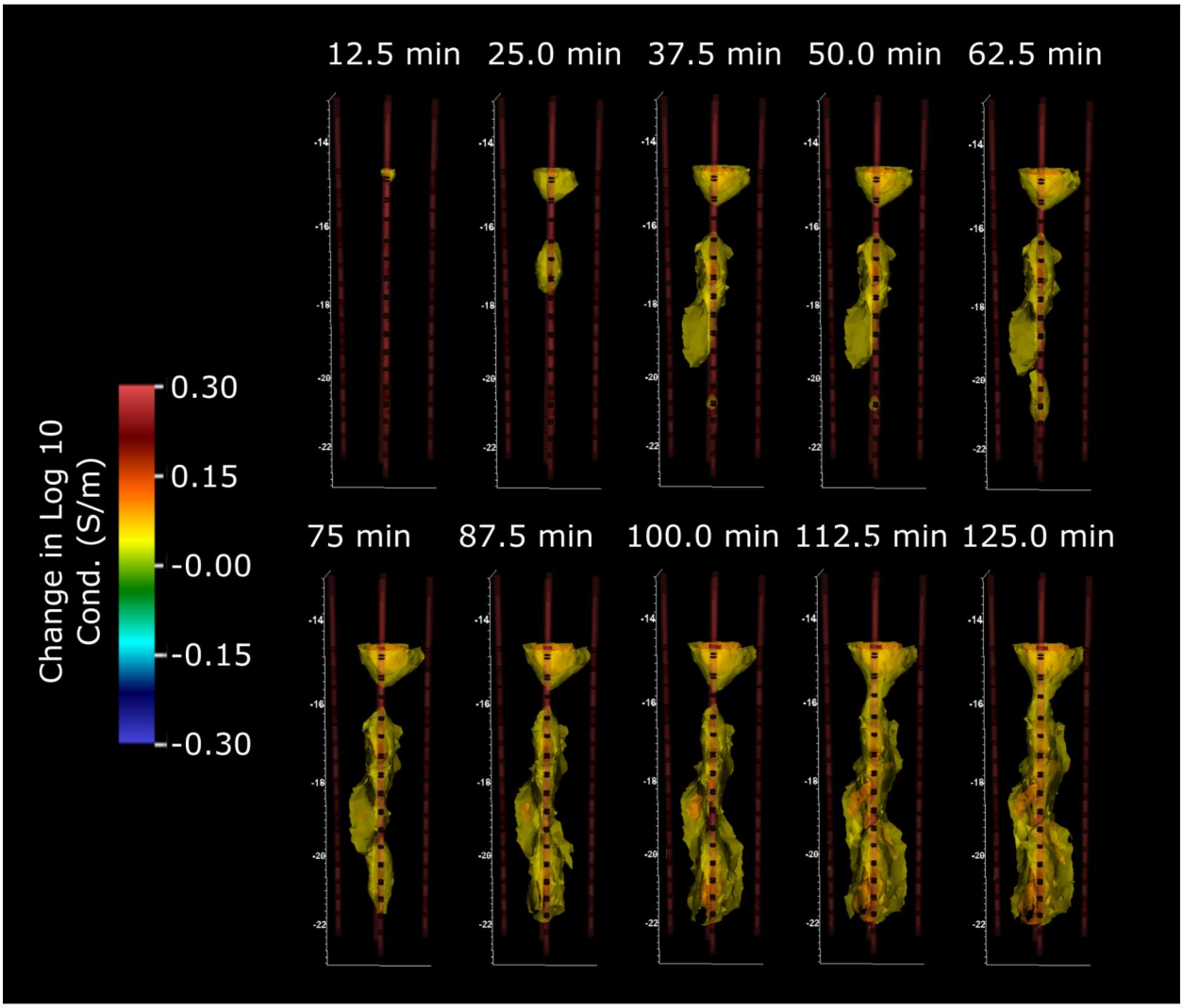

Figure 11.5. South to north facing view of real-time ERT images collected during zero valent iron tracer injection into the fracture stimulation zone.

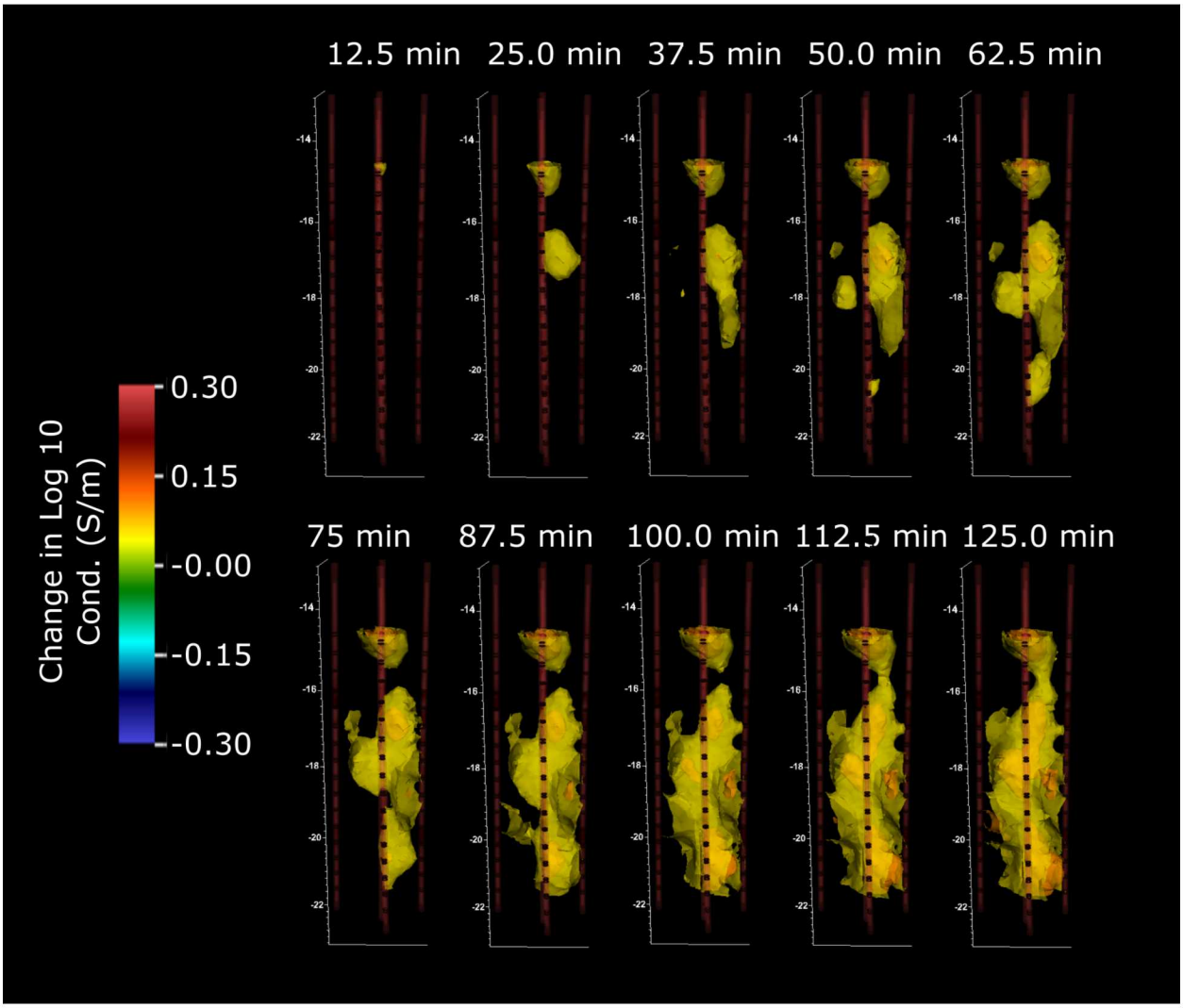

Figure 11.6. West to east facing view of real-time ERT images collected during zero valent iron tracer injection into the fracture stimulation zone.

which show a dominant vertical fracture. Although the time-lapse imaging occurred for approximately 330 minutes, the images do not change after 125 minutes, suggesting that the the ZVI tracers has filled the fractures within the imaging zone after about 125 minutes. This corresponds to a fracture volume of 235 liters (62 gallons) within the ERT imaging zone. Inspection of the imaging sequence also provides details concerning dominant flow paths within the fracture zone. For instance, tracer moving quickly in the upper portions of the fracture zone (about 15m depth). This location corresponds to the bottom of the borehole seal used to contain the stimulation pressure, which was shown by televiewer logs to be have two localized perpendicular vertical fractures rather than a single dominant zone.

In summary, the time lapse imaging ERT was able to characterize in real time and in 3D the dominant flow paths within the stimulated fracture zone, thereby illuminating the location of the dominant fractures. In combination with the known tracer injection rate, the time lapse ERT images was able to determine the fracture volume within the imaging zone.

Chapter 12

Ground Penetrating Radar

Crosshole ground penetrating radar (GPR) velocity data were collecting before and after each stimulation event. Although GPR is currently not applicable in deep subsurface environments, we collected cross hole GPR as an opportunity to provide structural information for verification of seismic and ERT imaging results, and to evaluate the utility of GPR for difference imaging of stimulated fracture zones. Pre- and post-stimulation analysis of radar travel times revealed differences caused by the stimulation event were below noise thresholds, eliminating the possibility of using GPR for difference imaging.

The baseline GPR image is shown in Figure12.1 in comparison to the baseline ERT image. Both images show a similar dipping structure, with a negative correlation between bulk conductivity and GPR velocity. The GPR inversion shown in Figure12.1 is a demonstration of the parallel ERT/travel-time joint inversion code developed as part of this project. The GPR travel-time data were inverted using the fresnel volume travel time tomography capabilities implemented in E4D as described in section 14.

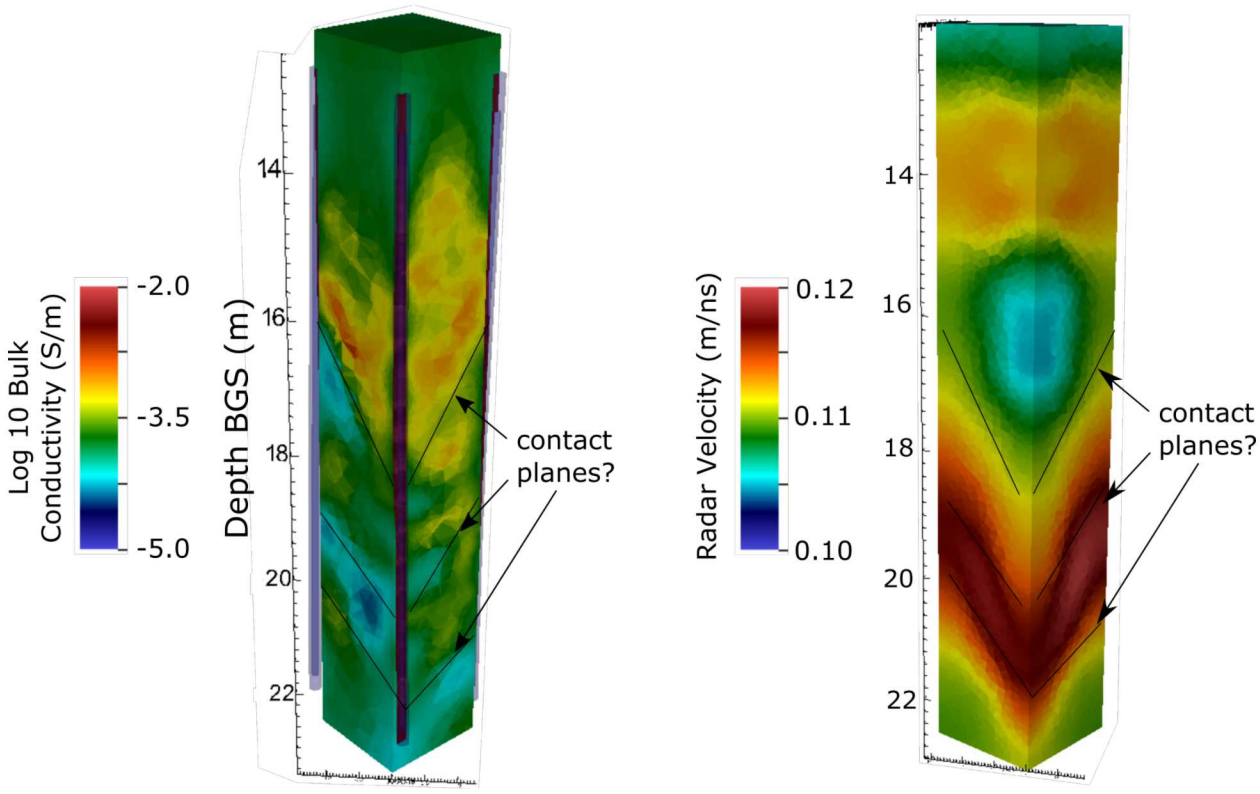

Figure 12.1. South to north facing view of baseline ERT (left) and GPR (right) images.

Chapter 13

Nano-Zero Valent Iron

The SubTER sensing pillar identified novel tracers as potential research candidates for providing information concerning stimulated fraction zones and fluid flow, particularly when coupled with geophysical imaging. Using pre- and post-fracture difference imaging, the presence of water in the stimulated fracture zone may provide an adequate contrast in geophysical properties for both seismic and ERT imaging. However, it is well known that those contrasts can be enhanced for improved imaging resolution using tracers. We demonstrated the use of a such a tracer for ERT imaging during the Blue Canyon Test. The object of the tracer was to provide a contrast in both electrical conductivity and also provide a polarization response that could be detected using Induced Polarization imaging. ZVI is known to provide such a contrast, and being relatively benign in the environment, was chosen as the tracer for the Blue Canyon experiments. Laboratory efforts were undertaken to formulate a ZVI solution that would both provide adequate contrast in conductivity and polarization, while staying in suspension long enough to migrate through the borehole and into the fracture zone during injection. Those studies revealed the necessity to suspend the ZVI in a reductant in order to prevent oxidation and degradation in electrical properties. The final design solution consisted of approximately 1.8 percent by weight ZVI suspended in a dithionite reductant solution. The solution had a conductivity of 0.7 S/m and a peak polarization response of 10 mrad at 5 Hz. The solution was stored in concentrated form for shipment, and diluted on sight prior to injection into the fracture zone as shown in Figure 13.1. As discussed previously, the ZVI solution provided an effective contrast agent for ERT imaging. However, the polarization data were contaminated by noise, likely from well-known inductive coupling in the ERT cables leading from the instrument trailer to the wellfield, and down the wellbores. There is currently no solution for this problem in collecting deep subsurface polarization data . However, coupling tracers with ERT and seismic imaging is an area of active research and may enable diagnosis of fractured rock characteristics that is currently not possible.

Figure 13.1. Zero-valent iron and diothionite reductant solution (right) applied to the mixing tank (right) prior to injection into the stimulated fracture zone.

Chapter 14

Joint Inversion Development

Electrical and particularly seismic geophysical methods have an established pedigree for interrogating the state of fractured rock systems, both in the literature and in the previous chapters of this report. These methods stand to play an integral role in providing the feedback mechanism necessary to control subsurface operations such as stimulation and resource recovery. Seismic and electrical sensing methods are complimentary of each other, in that seismic methods are predominantly sensitive to the mechanical properties of the subsurface, while electrical methods are also sensitive to geochemical properties. Interpreted together, these methods have the potential to provide high information-content four-dimensional monitoring of the subsurface. Furthermore, providing that information in near real-time is within reach, which was a primary goal of the SubTER initiative. We have demonstrated in this project the capability to collect both crosshole seismic and ERT data in near real-time, and to invert ERT data in near real-time. In the next chapter, we show progress toward addressing the primary obstacle inhibiting the real-time crosshole seismic imaging, namely the capability to autonomously pick arrival times with accuracy. With these advancements in mind, we proposed in this project to augment E4D (https://e4d.pnnl.gov) with the capability to model and invert cross-hole travel time in parallel, with the ultimate of objective of real-time joint inversion of crosshole seismic and ERT data. Building upon the modular framework and parallel inversion tools already incorporated into E4D, we developed a state-of-the art 3D Fast Forward Marching (FMM) algorithm on an unstructured tetrahedral mesh to model seismic travel times. The forward model uses the local Eikonal equation forward solver proposed by Fu et al. (2013) within the original FMM algorithm originally proposed by Sethian (1996). This facilitates the capability to efficiently and accurately model borehole effects or known boundaries in true dimension, thereby improving modeling accuracy and imaging resolution. Figure 14.1 shows a joint forward simulation of the electrical potential field and travel time field at the Blue Canyon Dome site. The upper image shows the electrical potential resulting from an active cross-well current source/sink pair, with electrodes, boreholes, and borehole annulus modeled in true dimension. The lower image shows the simulated seismic travel-time distribution given a source within a borehole at the indicated position. In this case the water filled borehole and cement annulus are modeled in true dimension. The effects of the boreholes and annular grout are evident in the images. Neglecting to model such effects in the imaging processes generally results in the inability to accurately fit data and a loss of resolution. The capability to model efficiently model such effects, and to do so with parallel computing resources, is critical for enabling inversions to be conducted in near real time (Figure 14.1).

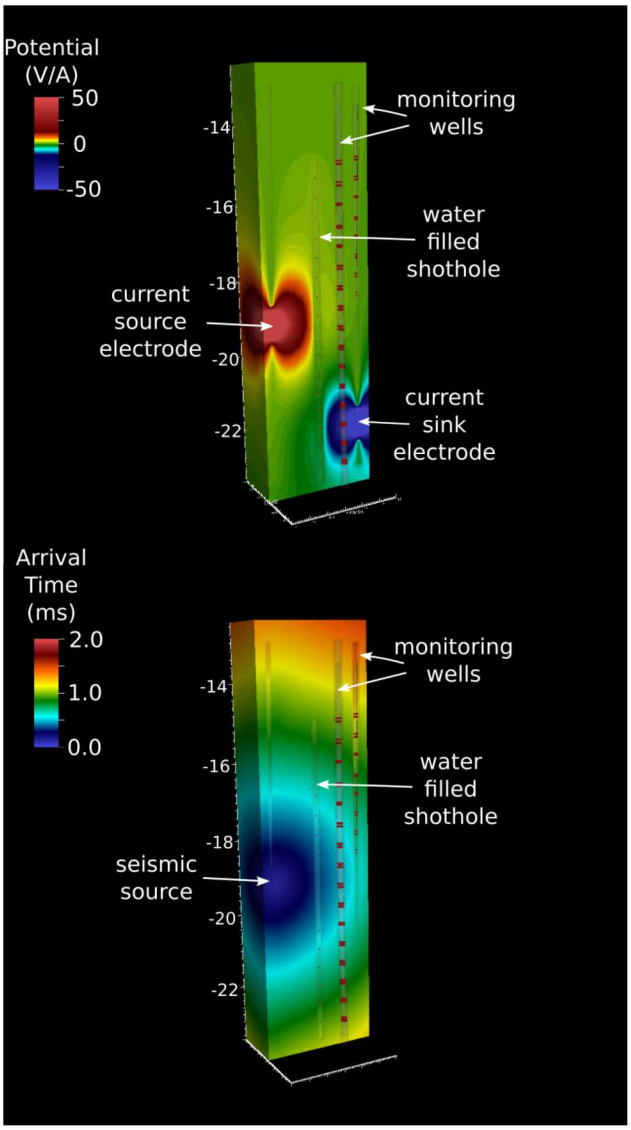

Figure 14.1. Joint forward simulation of subsurface potential (top) and wave travel time (bot) on a common computational mesh.

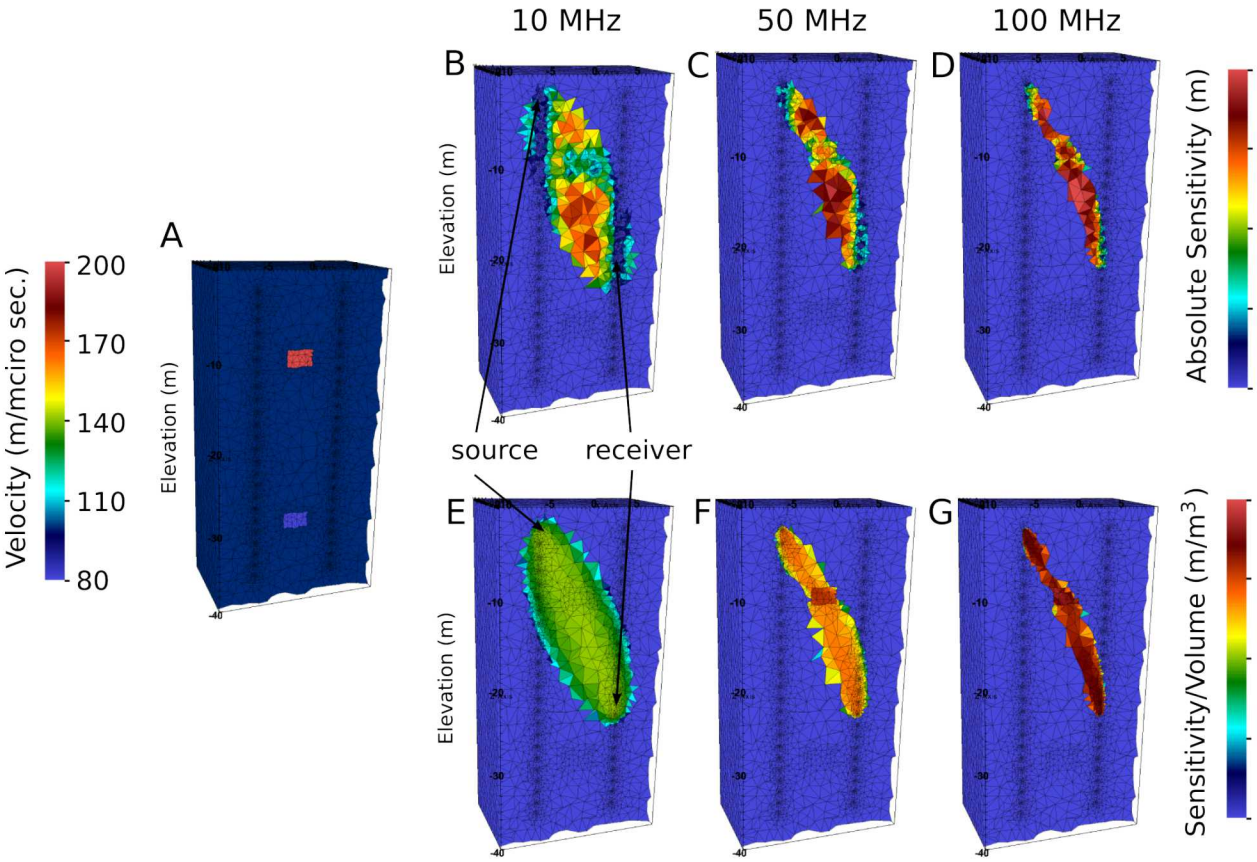

Figure 14.2. A) Radar velocity cross section on unstructured tetrahedral mesh. B-D) Absolute fresnel volume sensitivities at 10, 50 and 100 MHz. E-F) Fresnel volume sensitivities per unit volume at 10, 50 and 100 MHz.

For the traveltime inversion, we implemented a variant of the Fresnel volume sensitivities proposed by Watanabe et al. (1999). In contrast to ray-based tomography, Fresnel volume sensitivities account for the finite frequency dependent sensitivity of the travel time to the subsurface velocity distribution, and are a more accurate representation of wave propagation physics (Jordi et al., 2016; Johnson et al., 2012). Because the code is scalable, the slight increase in computation time associated with the Fresnel volume approach in comparison to the ray-based approached can be rectified by using additional compute cores. Figure 14.2 shows examples of Fresnel volume sensitivities computed using the newly developed FMM code. Figure 14.2 A shows a synthetic radar velocity distribution, which consists of two anomalous blocks embedded within an homogeneous background. Figure 14.2 B, C, D, show the Fresnel volume sensitivities for each element of the computational mesh for dominant wave propagation frequencies of 10 MHz, 50 MHz, and 100 MHz, respectively. Figure 14.2 E, F, and G show the corresponding sensitivity per unit volume. The narrowing of the Fresnel volume with increasing frequency is indicative of the ray approximation that becomes appropriate at the infinite frequency limit.

The FMM module for E4D was developed so that E4D and can execute independently in ERT mode, independently in FMM mode, or jointly in both ERT and FMM. In the latter case, the available computational cores are divided between E4D and FMM processor groups as specified by user input. Each processor group runs dependently (i.e. without communication with the other group) during forward and sensitivity computations. It is only during the inversion that the two processor groups communicate by passing to each other the current electrical conductivity and/or velocity models. These models are then used by each processor group to augment the model constraint matrix for each inversion with a 3D version of the cross-gradient minimization constraints proposed by Gallardo and Meju (2007). Cross-gradient minimization constraints are structural constraints that encourage the parameter fields (electrical conductivity and wave velocity in this case) to assume a similar spatial structure, which, assuming the parameter fields are correlated, improves overall resolution of each. These constraints can be particularly useful in time-lapse inversions, where the change in the parameter distributions from some baseline condition are assumed to have correlated spatial structure. For example, a decrease in velocity and increase in electrical conductivity is expected to occur a the location of a stimulated fracture. By jointly inverting seismic and ERT data, were are not only improving resolution of the location of the fracture zone, but also providing a more complete picture of the physical and geochemical changes associated with the stimulation. Furthermore, the parallel capabilities of the code provide the foundation for joint, real-time, time-lapse inversion of seismic and ERT data moving forward. Although the joint inversion code was completed and demonstrated during the period of performance (see Figure 12.1), time limitations inhibited demonstration of the code on the full 3D time-lapse seismic/ERT data collected during tracer injection. We anticipate completion of the joint inversion to be one of the culminating efforts of Blue Canyon Dome test and a major step toward real-time joint inversion in the future.

Chapter 15

Automatic Multiple Phase Arrival Time Estimates

Arrival times in seismic and ultrasonic acquisitions form the basis of later velocity structure analyses of rocks and other solid materials Aki and Richards (2002). As part of a detailed study of rock damage, large quantities of velocity data are acquired at a range of frequencies, with the highest frequencies targeting smaller spatial distances. However, with short distances, the later phase arrivals overlap on the codas of earlier phase arrivals (Kurz et al., 2005; Rinehart et al., 2016). Furthermore, with higher frequencies, elastic waves attenuate faster, which may cause low signal-to-noise ratios (SNRs). Nonetheless, for traditional velocity structure analysis (e.g. tomographic image analysis), accurate arrival time estimates are required. Unfortunately, manual arrival time estimation is slow, labor intensive and costly (Kanasewich, 1981; Sabbione and Velis, 2010; Shearer, 1994). Many types of automated arrival time estimators have been developed, but most require careful parameter tuning, or are not able to make any estimate of later phase arrival times (i.e., the S-wave arrival time) (Anant and Dowla, 1997; Rinehart et al., 2016; Sabbione and Velis, 2010).

Introduction

In this project, we use the method developed in Rinehart et al. (2016) to estimate first arrival times (P-wave arrival times) and, when possible, second arrival times (S-wave arrival times) from high frequency seismic data (nominally 60 kHz) collected between two wells in order to characterize explosion-induced fracturing from a central well. Rinehart et al.s method was developed to estimate phase arrival times from single component acoustic emissions data for 1 cm to 10 cm sample lengths at 25 MHz sampling frequencies with 0.5 to 2 MHz signal frequencies. They used a non-normalized rectilinity metric of the continuous wavelet transform scale covariance of the signal to identify the first arrival and a second arrival. In the current study, we are interested in lower frequencies (10s to 100s kHz) and larger spatial lengths (1s of m). Nonetheless, the short lag times, variable material, and relatively low SNRs of the tests have made automatic picking difficult; the signals are more similar to acoustic emissions than more traditional seismic signals (i.e. lower center frequency). Here we will provide a brief summary of the automatic picking case study conducted during the course of this project.

The development of a robust automatic picker is vital to the success of high frequency seismic characterization of damage zones. The tens of thousands of traces are collected make manually processing this quantity of data is cost prohibitive. By applying a new algorithm, we are opening new avenues for high density seismic data collection to understand rock damage.

Research Summary

As a summary, we present here the velocity estimates from the automatically estimated arrivals (Figure 15.1) and the percent error in P-wave velocity estimates relative to the manual first arrival estimates (Figure 15.1, center column). The majority of velocity estimates for Experiment 1 at all offset angles fall within 10% error (Figure 15.1 center column, light gray vertical lines). The quantity of outliers is greater for the higher offset angles (+45° and -45°) than for the 0° offset (Figure 15.1, center column). The greatest variability in error is seen at above 1802 m elevation in the +45° offset data. For all offsets, the number of outliers increases with experiment number (e.g. with damage). The number of misestimates decreases with depth for the P-wave arrival times.

The P-wave arrival times (Figure 15.1, left column) show a range of behaviors. For the 0° offset, the majority of the velocity estimates are internally consistent with increasing velocities with depth, and with decreasing velocities with increasing damage (from Experiment 1 to 2 to 3). There are some misidentified arrivals, even for the training data set (0°, Experiment 1; Figure 15.1a, black solid). With increasing damage, the number of misestimated velocities increase and the variability of the velocities from point to point increase, even though the arrival times remain close to the manual arrival time estimates. Between Experiment 1 (black) and 2 (gray solid), there is a distinct lowering of P-wave velocity. In Experiment 3, there is a large, low velocity zone around 1805 m elevation. This zone is consistent in both the manual and the automatic estimates. Misestimated velocities, or those with greater than 10% difference from the manual estimates, stand out as single points deviating by more than 0.5 km/s from the estimates immediately above and below them.

The P-wave velocities for the -45° offset (Figure 15.1d) show similar trends to the 0° offset estimates. There is a general increase in velocity with depth and a slight decrease in velocities between experiments. Recall that the source is above the receiver in this case, so the elastic waves are propagating generally from lower velocity into higher velocity materials. The number of misestimates is higher than for the 0° offset and increases with through the experiment sequence. Once again, the misestimates stand out as single points with a larger than 0.5 km/s difference in velocity from the neighboring points above and below it.

The P-wave velocities for the +45° offset (Figure 15.1g) shows considerable scatter in the uppermost 6 m of the survey and then little to no scatter below that. There is still a general trend of increasing velocity with increasing depth in the boreholes, and a clear decrease in velocity from Experiment 1 to Experiment 2. The majority of the measurements for

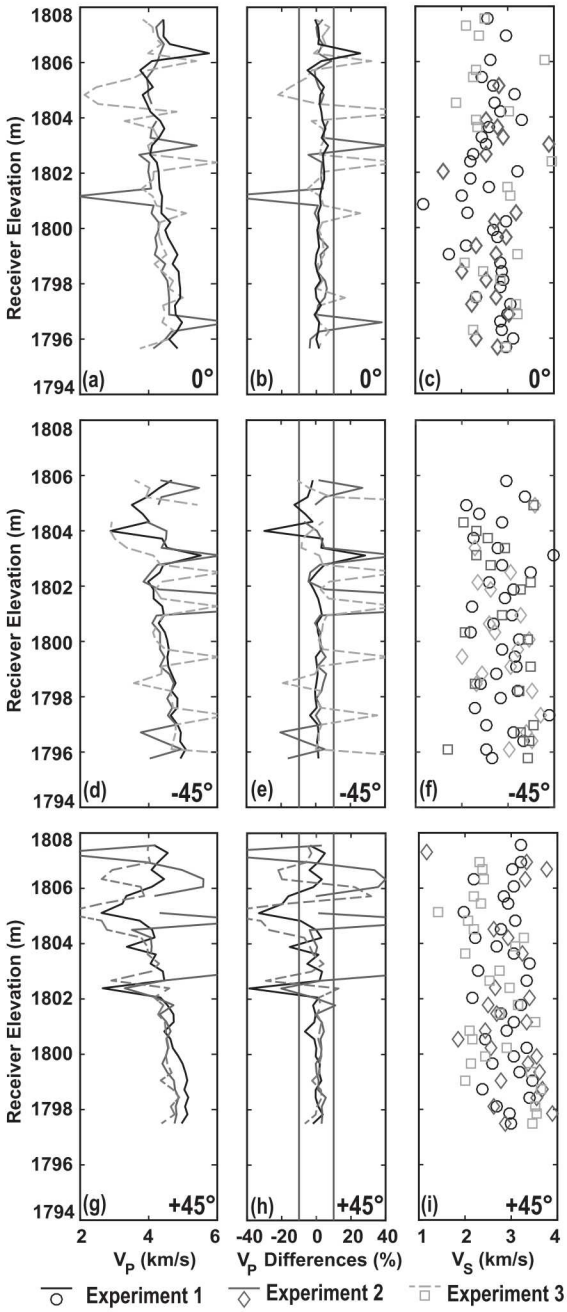

Figure 15.1. Summary of velocities (km/s) and errors (%) against elevation (m) for 0° data (a-c), -45° data (d-f), and +45° data (g-i) for Experiment 1 (solid black line, circle), Experiment 2 (solid grey line, diamond), and Experiment 3 (dashed grey line, square). Left column shows automatically estimated P-wave velocities (km/s), center column shows percent difference of automatically P-wave velocity estimate from manual P-wave velocity estimate (%; vertical gray lines at 10%), and right column shows automatically estimated S-wave velocities (km/s).

Experiment 1, even in the top 4 m, are within 10% of the manual estimates (Figure 15.1h). With increasing damage, the number of misestimates increases dramatically (Figure 15.1g) in the top 6 m of the borehole. Once again, these are, with one exception, more than 0.5 km/s different than the estimates above and below them.

The S-wave times are more problematic (Figure 15.1, right column). There appears to be a reasonable and roughly increasing-with-depth trend of data at 2800 m/s for the 0° offsets and Experiment 1. The later experiments at 0° offsets show an increased scatter. All three experiments, however, show a large amount of scatter between 1800 m and 1802 m elevation. A slight slowing shift is observed from Experiments 1 to 2 to 3, though this trend is partially obfuscated by the increase in uncertainty.

Both higher angle (-45° and +45°, Figure 15.1 f and i) S-wave velocity datasets show much more scatter than the 0° data. The data forms a 1.5 km/s-thick cloud centered around 3 km/s with a vague initial increasing-with-depth trend. The scatter increases from Experiment 1 to 2 to 3. Generally, the scatter increases with damage and is significantly less for the Experiment 1 +45° offset data than for the Experiment 1 -45° offset data. The later experiments have wildly scattered velocities.

We note here that these estimates for all three experiments at a given offset angle, between 100 and 120 traces per offset angle, required approximately eight seconds on a Windows 7 laptop with 8 GB of RAM and an Intel Core i7 processor using MATLAB version 2016a.

Discussion

The goal of this study was to understand how the arrival time estimating metrics in Rinehart et al. (2016) operated for this application; the estimates in the current study do not benefit from later quality assurance. The first arrival estimates are robust, even without the geometric and physical (i.e., velocity and travel time) constraints used in Rinehart et al. (2016) as an additional quality check. A simple post-analysis quality check of the first arrival phase velocities based on local percent changes in travel time or velocity could exclude misidentified first arrival estimates from later inversions. In other words, misidentifications could be identified by looking for velocity changes of greater than 10% than either neighboring estimate.

The increase in the number of misidentified arrival times with damage and with offset angle suggests that the metrics and method used for P-wave arrival times can be sensitive to high SNR, possibly enhanced by energy loss due to increased scattering in fractures. More of the traces showed lower SNR with increasing rock damage, and first arrival time misestimates often occur. The role of scattering is supported by the increasing of the number of misidentified arrivals through the experimental sequence. Additionally, more energy is expected to be lost when the receiver is above the sourcereflections will have more energy than the transmitted wave when the velocity is decreasing in the direction of propagation (Aki and Richards, 2002). This is observed in the upper 6 m of the +45° offset dataset.

In short, the fundamental metrics used in Rinehart et al. (2016) are effective in identifying first arrivals in cross borehole ultrasonics through damaged rock at a range of offset angles, and provide constraints in S-wave arrival times at low offset angles in undamaged rock. First arrival misestimates show large deviations from their neighboring arrival time estimates. This will allow culling of the poor time estimates before inverting the data. S-wave arrival times are obfuscated by multiple prior phase arrivals that are similar in amplitude and scale correlation structure to the S-wave. For both P- and S-wave arrivals, estimate quality decreases with distance, number of time-equivalent paths in the rock (i.e., multipathing and scattering), and with energy loss to scattering and reflections. With the incorporation of simple geometrical and physical quality checking after the initial arrival time identifications, this method should allow a rapid and reliable estimate of first arrival times, and it should allow the initial S-wave arrival times to be constrained.

Chapter 16

Self Consistent Modeling

Recent research has indicated that it is possible to relate changes in stress within a reservoir to changes in seismic attributes (Sayers and den Boer, 2012). In addition, Sayers and den Boer (2012) demonstrated an approach for relating these stress changes to evolution in the conductivity of embedded fractures and the associated upscaled permeability of the rock mass. In addition, Morris et al. (2013, 2015) demonstrated that it is possible to develop physics-based models for fractures that provide stress-dependent estimates of hydraulic conductivity and corresponding seismic/acoustic attributes. Such models combine details of spatial distribution of aperture with corresponding physical models of asperity and host-rock deformation to obtain an internally consistent representation of the evolution of contact and aperture within a stressed fracture. The result is a direct calculation of how remotely observable geophysical attributes vary with stress along with the hydraulic conductivity.

Let us assume that we have N fractures within a volume V with prescribed hydraulic transmissivities g, areas A, normal vectors n, and normal/shear compliances (B_N, B_T) for each of the fractures. Our goal is to model the effective compliance tensor S_{ijkl} (where $\epsilon_{ij} = S_{ijkl}\sigma_{kl}$, Schoenberg and Sayers (1995)) and permeability tensor ($\mathbf{k}$) for the volume V.

Following Schoenberg and Sayers (1995) and Sayers and den Boer (2012) we separate the compliance/permeability of the fracture rock mass into that due to the matrix (S^0_{ijkl}, $\mathbf{k}^0$) and the "excess" compliance/permeability due to the presence of the fractures (ΔS_{ijkl}, $\Delta\mathbf{k}$):

$$S_{ijkl} = S^0_{ijkl} + \Delta S_{ijkl} \tag{16.1}$$

$$\mathbf{k} = \mathbf{k}^0 + \Delta\mathbf{k} \tag{16.2}$$

A scalar estimate of the permeability of the fractured rock can then be obtained by taking the magnitude of the permeability tensor:

$$k = |\mathbf{k}| \tag{16.3}$$

Similarly, we can obtain a representative compressibility either by taking a magnitude or relevant component of the compliance tensor

$$S = |\mathbf{S}| \tag{16.4}$$

Note that for a tight matrix rock (such as a shale or granite) with dense fracturing, we expect the matrix compressibility and permeability to be small compared with those due to the presence of fractures.

Here we follow the approach outlined by Zhang et al. (2009) and Sayers and den Boer (2012) to obtained upscaled permeabilities and compressibilities. Our goal is to obtain an effective permeability, k, for a medium containing some number of fractures of specified area, orientation and conductivity. Following Kachanov (1980) , the permeability of a fractured reservoir may be estimated by first calculating a second-rank tensor, γ_{ij}, using:

$$\gamma_{ij} = \frac{1}{V} \sum_{r=1}^{N} g^{(r)} n_i^{(r)} n_j^{(r)} A^{(r)}, \tag{16.5}$$

where $g^{(r)}$ is the hydraulic transmissivity of fracture r in volume V. Note that r acts as an "index" into the list of N fractures. Note also that we can obtain the hydraulic transmissivity of fracture r from its aperture $h^{(r)}$ using the cubic law:

$$g^{(r)} = \frac{\left(b^{(r)}\right)^3}{12} \tag{16.6}$$

An estimate of the upscaled permeability due to the N fractures is given by

$$\Delta \mathbf{k} = C \left[tr\left(\boldsymbol{\gamma}\right) \mathbf{I} - \boldsymbol{\gamma} \right] \tag{16.7}$$

Here C is a coefficient between zero and unity reflecting the degree of fracture interconnectivity. We will assume C to be 0.747 based upon published numerical studies (Zhang et al., 2009; Sayers and den Boer, 2012).

It can be shown (Sayers and Kachanov, 1991, 1995) that the upscaled excess compliance due to the N fractures is:

$$\Delta S_{ijkl} = \frac{1}{4} \left(\delta_{ik} \alpha_{jl} + \delta_{il} \alpha_{jk} + \delta_{jk} \alpha_{il} + \delta_{jl} \alpha_{ik} \right) + \beta_{ijkl} \tag{16.8}$$

where α_{ij} is a second-rank fracture tensor and β_{ijkl} is a fourth-rank fracture tensor defined by

$$\alpha_{ij} = \frac{1}{V} \sum_{r=1}^{N} B_T^{(r)} n_i^{(r)} n_j^{(r)} A^{(r)} \tag{16.9}$$

$$\beta_{ijkl} = \frac{1}{V} \sum_{r=1}^{N} \left(B_N^{(r)} - B_T^{(r)} \right) n_i^{(r)} n_j^{(r)} n_k^{(r)} n_l^{(r)} A^{(r)} \tag{16.10}$$

As stated previously, $B_N^{(r)}$ and $B_T^{(r)}$ are the normal and shear compliances of the r^{th} fracture in the set of the N fractures in the volume V. Similarly, $n_i^{(r)}$ denotes the i^{th} component of the normal to the r^{th} fracture and $A^{(r)}$ is its area. We will now describe an approach to obtaining a consistent set of fracture dimensions and compliances for fractures under stress at depth.

In the absence of detailed, site-specific data, we need to utilize a model that relates fracture compliances and hydraulic properties (e.g., hydraulic aperture) to fracture lengths and stress state. (Morris et al., 2016) proposed a model that compares favorably against laboratory and field data as well as against detailed numerical simulation. The starting point for this approach was a previous observation due to Jocker et al. (2010) who developed a model for fracture mechanical behavior by introducing the concept of a thin layer with a thickness, h, representing the average fracture aperture, and stress-dependent elastic properties which capture the observed nonlinearity. Using their approach, the aperture of a fracture under stress is

$$h = \frac{h_0 C_{n,0}}{(C_{n,0} + \sigma_0)} \tag{16.11}$$

where h_0 is the stress-free aperture of the fracture, σ_n is the current normal stress on the fracture, and $C_{n,0}$ is a constant "intrinsic" stiffness of the layer (i.e., the normal stiffness which the layer/fracture possesses regardless of the presence of the applied normal stress). At a given stress level, the fracture specific stiffness (inverse of fracture normal compliance) can be obtained by Morris et al. (2016)

$$\kappa_n = \frac{h_0}{(h_0 - U_n)^2} C_{n,0} = \frac{(C_{n,0} + \sigma_n)^2}{h_0 C_{n,0}} \tag{16.12}$$

and normal compliance:

$$B_N = \frac{1}{\kappa_n} \tag{16.13}$$

Jocker et al. (2010) demonstrated that this model was consistent with a wide range of laboratory experiments. Morris et al. (2016) further demonstrated that this model was consistent with field observation of fracture compliance over a range of fracture lengths (see Figure 16.1).

Morris et al. (2016) found that a good fit to the observed scaling of compliance was obtained by taking:

$$C_{n,0} = 3.59 L^{-0.244}, \tag{16.14}$$

$$h_0 = 0.00505 L^{0.832} \tag{16.15}$$

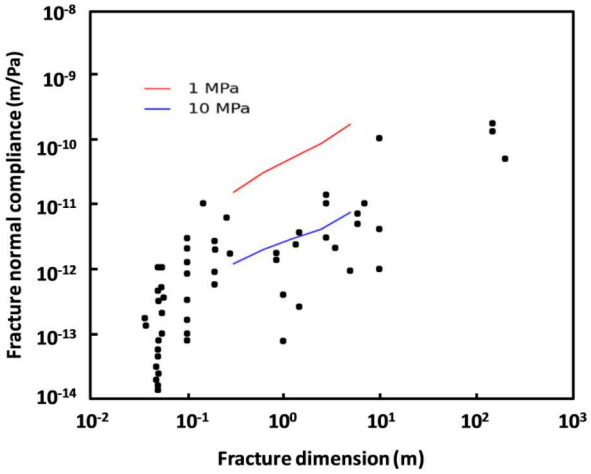

Figure 16.1. Comparison between Morris et al. (2016) (colored lines, in red at 1 MPa effective stress and blue at 10 MPa effective stress) and the results reviewed by Hobday and Worthington (2012) (black circles).

where L is the fracture length in cm, h_0 is in mm, and $C_{n,0}$ is in MPa. Using these fits for intrinsic stiffness and stress-free aperture, we can obtain estimates of the normal compliances and apertures of fractures of any length under stress. This approach does not provide an estimate for shear compliance, however, following Sayers and den Boer (2011) we can take this to be:

$$B_T = 2B_N \tag{16.16}$$

Given any distribution of dimensions for a set of fractures (length and height) we can use this model to generate an individual aperture h and normal/shear compliances (B_N, B_T) for each implicit fracture. From these we can derive hydraulic transmissivities g, via the cubic law and derive the upscaled compliances and permeability.

We have derived approaches for relating geophysical attributes (upscaled moduli) and permeability to a self-consistent representation for the individual fractures in the system. After successful completion of the aforementioned field test and the initial data reduction, we will apply a workflow similar to that developed by Sayers and den Boer (2012) to our seismic tomographic data. In doing so, we will attempt to obtain in situ estimates of the induced stress and permeability change due to both energetic stimulations and ZVI injections. As shown in Figure 16.2, the approach is to invert various forward models for geophysical and hydraulic properties to obtain predictions of the evolution of permeability.

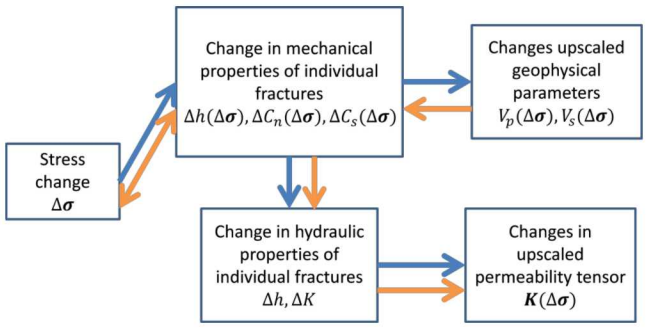

Figure 16.2. Forward models (blue arrows) have been developed to relate stress change in a formation to deformation on fractures. The mechanical deformation of the fractures, in turn can be related to changes in the fracture normal and shear compliances. In a rock mass containing a number of fractures, these changes can be upscaled to obtain anisotropic field-scale seismic velocities. Similarly, upscaled field-scale permeability tensors can also be calculated. These same models can be inverted to provide a workflow that inverts observed changes in geophysical attributes into stress changes and/or permeability changes. As part of this workflow, it is possible to either invert for stress change (if it is unknown) or use any quantified information regarding stress change to improve the accuracy of the inversion for permeability change.

Chapter 17

Future Work

In the text contained in this report, we have summarized the major tasks in this SubTER project. We have touched on a number of the current challenges surrounding real-time geophysical imaging of fractures and illustrated that new techniques, both for acquisition and processing, show promise in overcoming image resolution, economic burden, data processing constraints, etc. We have also highlighted the potential power in joint inversion of geophysical data for these types of imaging challenges. Finally, we have provided a dataset for researchers to test their ideas for the years to come.

We note here that a great deal of work remains in this field to fulfill the dream of designing a system capable of imaging fractures in real-time at the resolutions required to make meaningful reservoir development decisions. As can be easily seen from this report, there are three major topics which will need to be rigorously addressed before the system is realized: 1) processing of realtime crosswell seismic data, 2) development of fiber based (i.e. behind casing) measurements, and 3) a deeper understanding of joint inversion techniques and their associated tradeoffs. Independently, improvement in each of these areas will advance our imaging capabilities and/or reduce the economic burden of geophysical imaging in deep wellbore environments. Collectively, these improvements will revolutionize the way reservoirs are managed, which will allow for optimal production.

The challenges surrounding the realtime processing of crosswell seismic data, or any dense seismic dataset for that matter, originate in two places: 1) the shear volume of seismic data that is acquired and therefore requires processing and 2) precision imaging frequently requires waveform evaluation by a trained analyst. These obstacles could potentially be overcome in a few ways, three of which will be briefly discussed here. First, and simplest, if the target volume and change detection requirements (i.e. how much and how often the system should be imaged) were strictly defined, the seismic measurements could be optimized such that few extraneous measurements were taken. In the most efficient sense, this would require a deep understanding of fracture generation and evolution in a reservoir. In a more realistic environment, significant improvements could be realized by constraining these measurements using a basic understanding. The second way that this challenge could be addressed is to develop real time processing (e.g. massively parallel algorithms) that can estimate first arrivals and the pick error distributions, which would eliminate the need for analyst interpretation. While we recognize that substantial gains have been realized in this field, we feel that the research gap exists in defining the required pick accuracy for which

meaningful feedback is still possible (e.g. Do you need the 70% solution or the 90% solution?). Furthermore, it is unclear at this time how pick-errors, which may be represented by probability density functions in this case, are propagated through the model to help interpreters understand the spatial validity. The final way that this challenge could be addressed is to develop in-field processing techniques that do not rely on waveform interpretation (i.e. coda wave interferometry). This improvement would allow all of the data to be processed in the field. Then depending on the technique the waveform measurement could be transferred to computational resources offsite or potentially inverted onsite.

The development and deployment of behind casing fiber based measurements speaks to the economic burden of geophysical tools occupying the wellbore. At this time, we note that these measurement techniques (e.g. those systems without point sensors), are still undergoing basic research and development. Furthermore, it is not yet clear how the information gained from the measurements will be incorporated into pre-existing geomechanical models or will be used in traditional geophysical imaging. For example, one specific challenge for tomographic imaging with fiber data surrounds the compensation for gauge length and/or development of unique ray tracing for fiber deployments. This informational gap will need to be addressed before fiber based measurements are routinely utilized for reservoir management.

Finally, for realtime imaging and feedback to be realized, significant research of joint inversion techniques will be required. For the example, during this project we have chosen to implement structural controls on the joint inversion. This method allows for the two measurements sets (e.g. ERT and seismic) to be inverted in parallel, which is much faster than constraining all of the data to joint physics. However, there are situations where this structural control may struggle to resolve fractures (i.e. fractures that are not fluid filled either from isolation or relaxation). The computational efficiency of this technique vs its potential pitfalls must be evaluated against solving the fully-coupled inverse problem, which will likely be prohibitive for realtime feedback.

In conclusion, this SubTER project utilized state-of-the-art seismic and electrical geophysical imaging technologies that characterized 1) the 3D extent and distribution of fractures stimulated from the explosive source, 2) 3D fluid transport within the stimulated fracture network through use of a contrasting tracer, and 3) fracture attributes through advanced data analysis. Furthermore, we have shown that significant effort was placed upon developing real-time acquisition and processing, which is paramount for providing realtime feedback in reservoir management. The primary products from this study include a comprehensive set of 4D crosshole seismic and electrical dataset that can be used for testing algorithms and inversion techniques for years to come. Finally, during the course of this project we were able to develop methods of estimating fracture attributes from seismic data, assimilating disparate and transient data sets to improve fracture network imaging resolution, and advance capabilities for near real-time inversion of cross-hole tomographic data. These are relevant to all situations where fracture emplacement is used for reservoir stimulation (e.g. Enhanced Geothermal Systems (EGS) and tight shale gases).

References

Agarwal, R. (1980). A new method to account for producing time effects when drawdown type curves are used to analyze pressure buildup and other test data. *Proceedings of SPE Annual Technical Conference and Exhibition*.

Ajo-Franklin, J. (2012). Continuous active source seismic monitoring (cassm) : Applications in monitoring co2 sequestration and hydraulic fracture evolution [2 case studies]. University Lecture.

Ajo-Franklin, J., Daley, T., Butler-Veytia, B., Peterson, J., Wu, Y., Kelly, B., Hubbard, S., et al. (2011). Multi-level continuous active source seismic monitoring (ml-cassm): Mapping shallow hydrofracture evolution at a tce contaminated site. In *2011 SEG Annual Meeting*. Society of Exploration Geophysicists.

Ajo-Franklin, J. B. (2009). Optimal experiment design for time-lapse traveltime tomography. *Geophysics*, 74(4):Q27–Q40.

Ajo-Franklin, J. B., Minsley, B. J., and Daley, T. M. (2007). Applying compactness constraints to differential traveltime tomography. *Geophysics*, 72(4):R67–R75.

Aki, K., Fehler, M., Aamodt, R., Albright, J., Potter, R., Pearson, C., and Tester, J. (1982). Interpretation of seismic data from hydraulic fracturing experiments at the fenton hill, new mexico, hot dry rock geothermal site. *Journal of Geophysical Research: Solid Earth*, 87(B2):936–944.

Aki, K. and Richards, P. G. (2002). *Quantitative seismology*, volume 2.

Anant, K. S. and Dowla, F. U. (1997). Wavelet transform methods for phase identification in three-component seismograms. *Bulletin of the Seismological Society of America*, 87(6):1598–1612.

Bergmann, P., Ivandic, M., Norden, B., Rücker, C., Kiessling, D., Lüth, S., Schmidt-Hattenberger, C., and Juhlin, C. (2013). Combination of seismic reflection and constrained resistivity inversion with an application to 4d imaging of the co 2 storage site, ketzin, germany. *Geophysics*, 79(2):B37–B50.

Campillo, M. and Paul, A. (2003). Long-range correlations in the diffuse seismic coda. *Science*, 299(5606):547–549.

Chamberlin, R. M., McIntosh, W. C., and Eggleston, T. L. (2004). 40ar/39ar geochronology and eruptive history of the eastern sector of the oligocene socorro caldera, central rio grande rift, new mexico. *New Mexico Bureau of Mines and Mineral Resources Bulletin*, 160:251–279.

Daley, T. M., Freifeld, B. M., Ajo-Franklin, J., Dou, S., Pevzner, R., Shulakova, V., Kashikar, S., Miller, D. E., Goetz, J., Henninges, J., et al. (2013). Field testing of fiber-optic distributed acoustic sensing (das) for subsurface seismic monitoring. *The Leading Edge*, 32(6):699–706.

Daley, T. M., Solbau, R. D., Ajo-Franklin, J. B., and Benson, S. M. (2007). Continuous active-source seismic monitoring of co 2 injection in a brine aquifer. *Geophysics*, 72(5):A57–A61.

Freeze, R. A. and Cherry, J. A. (1979). Groundwater, 604 pp.

Fu, Z., Kirby, R. M., and Whitaker, R. T. (2013). A fast iterative method for solving the eikonal equation on tetrahedral domains. *SIAM J. Sci. Comput. SIAM Journal on Scientific Computing*, 35(5).

Gallardo, L. A. and Meju, M. A. (2007). Joint two-dimensional cross-gradient imaging of magnetotelluric and seismic traveltime data for structural and lithological classification. *Geophysical Journal International*, 169(3):12611272.

Gringarten, A. and Witherspoon, P. (1972). A method of analyzing pump test data from fractured aquifers. *Percolation through fissured rock, Deutsche Gesellschaft fur Red and Grundbau, Stuttgart*, pages T3B1–T3B8.

Hadziioannou, C., Larose, E., Coutant, O., Roux, P., and Campillo, M. (2009). Stability of monitoring weak changes in multiply scattering media with ambient noise correlation: Laboratory experiments. *The Journal of the Acoustical Society of America*, 125(6):3688–3695.

Hobday, C. and Worthington, M. (2012). Field measurements of normal and shear fracture compliance. *Geophysical Prospecting*, 60(3):488–499.

Hole, J. and Zelt, B. (1995). 3-d finite-difference reflection traveltimes. *Geophysical Journal International*, 121(2):427–434.

Jocker, J., Prioul, R., et al. (2010). Analysis of fracture mechanical behavior under normal stress. In *44th US Rock Mechanics Symposium and 5th US-Canada Rock Mechanics Symposium*. American Rock Mechanics Association.

Johnson, T., Versteeg, R., Thomle, J., Hammond, G., Chen, X., and Zachara, J. (2015). Four-dimensional electrical conductivity monitoring of stage-driven river water intrusion: Accounting for water table effects using a transient mesh boundary and conditional inversion constraints. *Water Resources Research*, 51(8):6177–6196.

Johnson, T. and Wellman, D. (2015). Accurate modelling and inversion of electrical resistivity data in the presence of metallic infrastructure with known location and dimension. *Geophys. J. Int. Geophysical Journal International*, 202(2):10961108.

Johnson, T. C., Slater, L. D., Ntarlagiannis, D., Day-Lewis, F. D., and Elwaseif, M. (2012). Monitoring groundwater-surface water interaction using time-series and time-frequency analysis of transient three-dimensional electrical resistivity changes. *Water Resources Research*, 48(7).

Johnson, T. C., Versteeg, R. J., Ward, A., Day-Lewis, F. D., and Revil, A. (2010). Improved hydrogeophysical characterization and monitoring through parallel modeling and inversion of time-domain resistivity andinduced-polarization data. *Geophysics*, 75(4).

Jordi, C., Schmelzbach, C., and Greenhalgh, S. (2016). Frequency-dependent traveltime tomography using fat rays: application to near-surface seismic imaging. *Journal of Applied Geophysics*, 131:202213.

Kachanov, M. (1980). Continuum model of medium with cracks. *Journal of the engineering mechanics division*, 106(5):1039–1051.

Kanasewich, E. R. (1981). *Time sequence analysis in geophysics*. University of Alberta.

Kurz, J. H., Grosse, C. U., and Reinhardt, H.-W. (2005). Strategies for reliable automatic onset time picking of acoustic emissions and of ultrasound signals in concrete. *Ultrasonics*, 43(7):538–546.

Lin, F.-C., Moschetti, M. P., and Ritzwoller, M. H. (2008). Surface wave tomography of the western united states from ambient seismic noise: Rayleigh and love wave phase velocity maps. *Geophysical Journal International*, 173(1):281–298.

Majer, E. L., Peterson, J. E., Daley, T., Kaelin, B., Myer, L., Queen, J., D'Onfro, P., and Rizer, W. (1997). Fracture detection using crosswell and single well surveys. *Geophysics*, 62(2):495–504.

Molenaar, M. M., Hill, D., Webster, P., Fidan, E., Birch, B., et al. (2012). First downhole application of distributed acoustic sensing for hydraulic-fracturing monitoring and diagnostics. *SPE Drilling & Completion*, 27(01):32–38.

Morris, J. et al. (2015). Numerical investigation of the relationship between fracture shear compliance and conductivity anisotropy. In *49th US Rock Mechanics/Geomechanics Symposium*. American Rock Mechanics Association.

Morris, J., Jocker, J., Prioul, R., et al. (2013). Exploring alternative characterizations of fracture stiffness and their respective scaling behaviors. In *47th US Rock Mechanics/Geomechanics Symposium*. American Rock Mechanics Association.

Morris, J. P., Jocker, J., and Prioul, R. (2016). Numerical investigation of alternative fracture stiffness measures and their respective scaling behaviours. *Geophysical Prospecting*.

Neal, J., Krohn, C., et al. (2012). Higher resolution subsurface imaging. *Journal of Petroleum Technology*, 64(03):44–53.

Niu, F., Silver, P. G., Daley, T. M., Cheng, X., and Majer, E. L. (2008). Preseismic velocity changes observed from active source monitoring at the parkfield safod drill site. *Nature*, 454(7201):204–208.

Olson, L. and Wright, C. (1989). Seismic, sonic, and vibration methods for quality assurance and forensic investigation of geotechnical, pavement and structural systems. *Non-Destructive Testing And Evaluation For Manufacturing And Construction.*, page 263.

Parker, T., Shatalin, S., and Farhadiroushan, M. (2014). Distributed acoustic sensing–a new tool for seismic applications. *first break*, 32(2):61–69.

Rinehart, A. J., McKenna, S. A., and Dewers, T. A. (2016). Using wavelet covariance models for simultaneous picking of overlapping p-and s-wave arrival times in noisy single-component data. *Seismological Research Letters*.

Robinson, J., Slater, L., Johnson, T., Shapiro, A., Tiedeman, C., Ntarlagiannis, D., Johnson, C., Day-Lewis, F., Lacombe, P., Imbrigiotta, T., et al. (2015). Imaging pathways in fractured rock using three-dimensional electrical resistivity tomography. *Groundwater*.

Sabbione, J. I. and Velis, D. (2010). Automatic first-breaks picking: New strategies and algorithms. *Geophysics*, 75(4):V67–V76.

Sayers, C. and Kachanov, M. (1991). A simple technique for finding effective elastic constants of cracked solids for arbitrary crack orientation statistics. *International Journal of Solids and Structures*, 27(6):671–680.

Sayers, C. and Kachanov, M. (1995). Microcrack-induced elastic wave anisotropy of brittle rocks. *Journal of Geophysical Research: Solid Earth*, 100(B3):4149–4156.

Sayers, C. M. and den Boer, L. D. (2011). Rock physics-based relations for density and s-velocity versus p-velocity in deepwater subsalt gulf of mexico shales. *The Leading Edge*, 30(12):1376–1381.

Sayers, C. M. and den Boer, L. D. (2012). Characterizing production-induced anisotropy of fractured reservoirs having multiple fracture sets. *Geophysical Prospecting*, 60(5):919–939.

Schmidt, R. A., Warpinski, N. R., Cooper, P. W., et al. (1980). In situ evaluation of several tailored-pulse well-shooting concepts. In *SPE Unconventional Gas Recovery Symposium*. Society of Petroleum Engineers.

Schoenberg, M. and Sayers, C. M. (1995). Seismic anisotropy of fractured rock. *Geophysics*, 60(1):204–211.

Sens-Schönfelder, C. and Wegler, U. (2006). Passive image interferometry and seasonal variations of seismic velocities at merapi volcano, indonesia. *Geophysical research letters*, 33(21).

Sethian, J. A. (1996). A fast marching level set method for monotonically advancing fronts. *Proceedings of the National Academy of Sciences*, 93(4):15911595.

Shapiro, N. M. and Campillo, M. (2004). Emergence of broadband rayleigh waves from correlations of the ambient seismic noise. *Geophysical Research Letters*, 31(7).

Shearer, P. M. (1994). Global seismic event detection using a matched filter on long-period seismograms. *JOURNAL OF GEOPHYSICAL RESEARCH-ALL SERIES-*, 99:13–713.

Silver, P. G., Daley, T. M., Niu, F., and Majer, E. L. (2007). Active source monitoring of cross-well seismic travel time for stress-induced changes. *Bulletin of the Seismological Society of America*, 97(1B):281–293.

Vidale, J. E. (1990). Finite-difference calculation of traveltimes in three dimensions. *Geophysics*, 55(5):521–526.

Watanabe, T., Matsuoka, T., and Ashida, Y. (1999). Seismic traveltime tomography using fresnel volume approach. *SEG Technical Program Expanded Abstracts 1999*.

Zhang, Y., Sayers, C. M., and Adachi, J. I. (2009). The use of effective medium theories for seismic wave propagation and fluid flow in fractured reservoirs under applied stress. *Geophysical Journal International*, 177(1):205–221.

Appendix A

Test	Start Date	End Date	Sampling Frequency (kHz)	File Duration (s)	Purpose
Angled CT	4/15/16 8:36:00	4/15/16 8:52:00	100	30	15 minute trial determining if there is any signal detected
Day Activities 4-16-16	4/16/16 7:53:00	4/16/16 17:50:00	10	30	Characterize daytime wavefield recorded on fiber
ML-CASSM 1	4/13/16 18:00:00	4/14/16 19:22:00	100	0.015	Night test with LBNL using their seismic impulse source.
ML-CASSM 3	4/16/16 18:00:00	4/18/16 7:27:00	100	0.015	Night test with LBNL using their seismic impulse source.
Night Recording 4-12-16	4/12/16 18:44:00	4/13/16 7:32:00	10	30	First night recording ambient noise, prior to first shot
Night Recording 4-14-16	4/14/16 18:07:00	4/15/16 7:24:00	10	30	Second night recording for ambient noise, after first shot
Night Recording 4-15-16	4/15/16 18:30:00	4/16/16 7:51:00	10	30	Third night recording for ambient noise, prior to second shot
Night Recording 4-18-16	4/18/16 19:14:00	4/19/16 7:25:00	10	30	Fourth night recording for ambient noise, after second shot
Post Shot 2 Pressure Test	4/18/16 15:57:00	4/18/16 19:12:00	10	30	Looking for indications of breakthough with the fiber
Pre-Water Injection1	4/14/16 9:40:00	4/14/16 9:57:00	100	30	Gathering data for a baseline
Pre-Water Injection1	4/14/16 9:58:00	4/14/16 12:52:00	10	30	Gathering data for a baseline
SHOT 1	4/13/16 15:13:00	4/13/16 15:16:00	100	30	Captures the explosive shot
SHOT 2	4/18/16 15:02:00	4/18/16 15:05:00	100	30	Captures the explosive shot
Water Injection1	4/14/16 12:55:00	4/14/16 17:57:00	100	30	Investigate fiber recordings from the treatment well
Water Injection2	4/18/16 9:28:00	4/18/16 12:34:00	100	30	Investigate fiber recordings from the treatment well
ZVI Injection 1	4/15/16 14:01:00	4/15/16 18:29:00	100	30	Investigate fiber recordings from the treatment well
ZVI Injection 2	4/19/16 13:11:00	4/19/16 15:14:00	100	30	Investigate fiber recordings from the treatment well

Figure A.1. Collection details of activities and time periods recorded on the borehole fiber optic cables.

DISTRIBUTION:

	MS		,
			,
1	MS	0899	Technical Library, 9536 (electronic copy)


Sandia National Laboratories